Effect of Pressure on the Rheological Properties of Three Polyethylenes

By
Hee Eon Park

Department of Chemical engineering
McGill university, Montreal

April 2001

A Thesis submitted to the Faculty of Graduate Studies in partial fulfillment of the requirements of the degree of Master of Engineering

0-612-70248-0

With My Wish

for Successful Accomplishing "I.L.Y. Project"

비는 싫지만 소나기는 좋고,
인간은 싫지만 너만은 좋다.

내가 새라면 너에게 하늘을 주고,
내가 꽃이라면 너에게 향기를 주겠지만
나는 인간이기에 너에게 사랑을 준다.

이혜인의 너에게 띄우는 글에서.

Abstract

The effect of pressure on the viscosity of polyethylenes was studied using a newly developed high-pressure, sliding-plate rheometer. The rheometer subjects the sample to a homogeneous pressure and temperature at levels up to 70 MPa and 225℃. Simple shear is generated in the sample, and the resulting shear stress is measured locally in the center of the sample by means of a shear stress transducer. Viscosity curves were generated at four pressures from 0.1 to 70 MPa, and it was found that the pressure data could be shifted onto the ambient pressure curves by means of a pressure shift factor. The viscosity increases exponentially with pressure. Long chain branching increases the pressure sensitivity, but the polydispersity has little effect.

The effect of pressure on the creep behavior of polyethylenes was also studied. It was observed that pressure decreases the creep compliance. Careful tuning the controller is required to obtain reliable data when operating the rheometer in the creep mode.

Résumé

L'objectif de ce travail est d'étudier les effets de la pression sur la viscosité des polyéthylènes à l'aide d'un nouveau rhéomètre à cisaillement plan haute pression. La gamme de pression et température accessibles s'étend jusqu'à 70 MPa et 225°C. L'échantillon est soumis à un cisaillement pur et la contrainte de cisaillement résultante est mesurée localement au centre de léchantillon à l'aide d'un transducteur de contrainte. Des courbes de viscosité ont été obtenues pour quatre valeurs de pression entre 0.1 et 70 MPa et on a mis en évidence l'existence d'un coefficient de décalage en pression permettant de former une courbe maîtresse à la pression ambiante. La variation de la viscosité avec la pression suit une loi exponentielle. La présence de ramifications longues dans l'échantillon augmente la sensibilité à la pression, alors que l'effet de la polydispersité est peu marqué.

On a également étudié l'effet de la pression sur le comportement en fluage des polyéthylènes. On a pu observer une diminution de la complaisance en fluage avec la pression. L'obtention de données fiables en fluage nécessite un soin particulier dans les réglages du contrôleur du rhéomètre.

Acknowledgements

It is the greatest honor to express appreciation for everything from my mentor Dr. John M. Dealy. When I started my research here, my goal was obtaining good (not necessarily beautiful) results, but now it is being like him.

Special thanks must go to Charles Dolan, whose excellent cares to any mechanical difficulties helped me get through the situations. I also appreciate the training done by Dr. Stewart McGlashan and instant technical answers given by Dr. Francois Koran and Dr. Frank Bubic.

One of the most fabulous experiences that I have is having had the opportunity to work as a part of such a great research team. Dr. Paula Wood-Adams always gave me precious suggestions, criticism, and encouragement. Dr. Daryoosh Beigzadeh awoke my interest in polymer synthesis. I am also grateful to the post-doctoral fellows, Dr. Stéphane Costeux and Dr. Benoît Blottiere, for their academic advice. I am very much indebted to Seungoh Kim for priceless suggestions and inspiration, and his help played a very important role in my successful life here. Yufeng Ye, who is my first office mate, gave me important ideas concerning creep tests and trained me on an SR5000. Whenever I worked at late night, Siripon Anatawaraskul was also working in our lab. It was pretty good time to discuss important problems with Chunxia He and Enrique Torres.

I am especially grateful to Dr. Juan Vera for the concerns for Differential Fee Waivers. I would like to thank Alan Gagnon and Lou Cusmich for their prompt assistance concerning electrical or mechanical situations. I also appreciate the cooperation done by every staff in the Inter Library Loan Office. It really helped me a lot to finish my studies on time.

I would also like to thank the graduate students and research associates in the

Department of Chemical Engineering. Young Mi Chung is my ten-year friend since when I was a freshman. Her passion for research and studies always excited and encouraged me, and her academic background and knowledge have been fabulous help for my studies. Young Gyun Cho, with whom I share wonderful memories, delivered important industrial experience and knowledge, and those helped me to find good ideas for my research. Hongsun Son's industrial experience fascinated me a lot. Byoung-Uk Cho provided me books which were helpful to take care of my health. Ae-Gyeong Cheong used to work in her lab until early in the morning, and it brought me much consolation when I kept the no "sleep" condition during writing my thesis. Dr. Young-Sang Yun helped me start studying at McGill. Dr. Richard Lai-Fook taught me how to use a dead weight tester, and it was essential for obtaining the confidence to the pressure transducer.

I would also like to thank professors at POSTECH, South Korea for the encouragement and advice. Dr. Young Gul Kim, Dr. Kyung Hee Lee, Dr. Sun Bok Lee, and Dr. Jong Moon Park always encouraged me to keep my studies and let me pick up valuable information. Dr. In-Sik Nam, who was my Bachelor thesis supervisor, not only consulted with me about my future but also has gave me a bill for my future haircut, and I keep the bill as a kind of a charm against evils. Dr. Jin Kon Kim, who is the research director in the Polymer Nano-Rheology Lab, gave me a lot of information regarding rheology studies.

I would also like to thank students at POSTECH who provided me with lots of scientific documents and books. Jeongman The-Man Son, who was a graduate student in the Polymer Nano-Rheology Lab, never complained about my endless requests concerning references. The wonderful retrospections with Woosung Adrian Jung and Sunyoung Bbox Park have been strong stimulation for my life. The great time shared with Minseok Song, Yongwoo Shin, and Jiyoung Na also has been big solace. Daihyun Park, who was my last room mate at POSTECH, mentally assisted me so much. Hyejin Kim, who always shows an active attitude to everything, promoted my diligence. Sangsook Cecily Kim and Hyunmi Timy Baek, who used to be L.C.C., also offered my needs many times.

Finally, I must thank my every ancestor and ancestress who made me exist and made me able to experience the beautiful life on earth. Undoubtedly my ultimate thanks must go to my family, especially my parents, brother, sister-in-law, and my first nephew Taejun.

Table of Contents

List of Figures

List of Tables

Chapter 1. Introduction

Since high pressures are involved in many plastics forming processes, the rheological behavior of polymer melts under such conditions is very important. For example, in high-speed injection molding the viscosity may increase by an order of magnitude as the pressure rises from one atm to 100 MPa, and reliable high-pressure data are thus required for the simulation and design of injection molds. It is clear that viscosity data obtained at atmospheric pressure can be quite misleading if applied to a high-pressure process. However, there have been few measurements of the effect of pressure on rheological properties.

Constant stress experiments are required to determine the creep compliance, which is an important viscoelastic property. Constant stress tests are also useful for slip studies. The slip velocity increases with shear stress above a critical value of around 0.1 MPa, depending on the nature of the polymer, but it is also of interest to study the pressure dependence of slip. However, due to the difficulty of making measurements under high pressure, very few creep and slip measurements at elevated pressures have been reported. A newly developed high-pressure sliding plate rheometer provides a reliable way to measure rheological properties and slip at high pressure.

1.1. Objectives

The primary objectives of the research were to determine the effect of pressure on viscosity of three polyethylenes having different molecular structure and the effect of molecular structure on the pressure sensitivity of the viscosity.

Secondary objectives were to investigate the effect of pressure on the creep compliance and creep recovery and to improve the reliability of the new high-pressure rheometer.

1.2. Viscosity

The viscosity of polymeric fluids is a very important physical property in polymer processing, as it is directly related to processability. The viscosity of a polymer is highly dependent on temperature, pressure, shear rate, molecular structure, and additives. Even though elevated pressures are involved in several important polymer processing operations, such as high speed extrusion and injection molding, the pressure dependence of the viscosity has not been well studied due to the difficulty of carrying out experiments at high pressure.

1.2.1. Shear Rate Dependency

For Newtonian fluids the viscosity is independent of shear rate, but most polymer melts are non-Newtonian, and the viscosity is a strong function of shear rate. The curve of viscosity versus shear rate shows three regions: Newtonian (constant viscosity), transition, and power law. The limiting value of the viscosity at low shear rate is called the zero-shear or Newtonian viscosity, which is given the symbol η_0. In the next region the viscosity begins to decrease with increasing shear rate, finally approaching a power-law region. Plots using linear scales do not show the three regions clearly (Fig. 1.1), so that viscosity shear rate data are usually plotted using logarithmic scales (Fig. 1.2).

A number of equations have been proposed to describe the dependence of viscosity on shear rate. One example is the power law model that often describes the viscosity at high shear rates:

$$\eta = \eta_0 |\lambda \dot{\gamma}|^{n-1} \tag{1.1}$$

where n is the power-law index, and λ is a characteristic time of the material. This time constant usually has the same temperature dependence as the viscosity and can thus be expressed as:

$$\lambda \equiv \eta_0 / \tau \tag{1.2}$$

where τ is a material dependent constant having units of stress. Since η_0 is a function of temperature and pressure, λ is also a function of temperature and pressure.

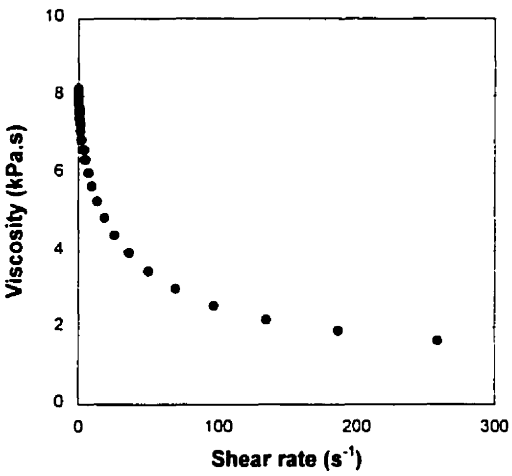

Figure 1.1. Typical viscosity versus shear rate curve for a shear thinning material with linear scales: Linear metallocene polyethylene at 170℃.

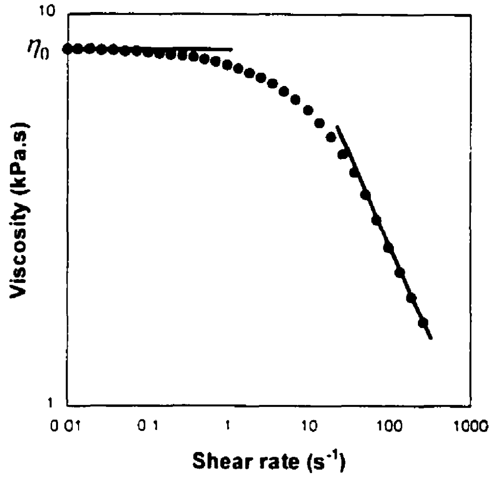

Figure 1.2. The viscosity curve for the same material using logarithmic scales.

To describe behavior over a broad range of shear rates, several generalized power law equations have been proposed. An example is the Cross model [1], which is shown in Equation 1.3:

$$\eta=\frac{\eta_0}{1+|\lambda\dot{\gamma}|^m} \tag{1.3}$$

At low shear rates, the viscosity approaches η_0, and at high shear rate, the viscosity shows power law behavior with $m = 1 - n$. The characteristic time, λ, is the inverse of the shear rate at which the viscosity is half the zero-shear viscosity. The Carreau model [2] is given by:

$$\eta=\frac{\eta_0}{[1+(\lambda\dot{\gamma})^2]^m} \tag{1.4}$$

where m is a material constant, and the viscosity shows power law behavior with

$m=(1-n)/2$ at high shear rates. Yasuda [3] added another constant, a, to facilitate curve fitting, to give Equation 1.5:

$$\eta=\frac{\eta_0}{[1+(\lambda\dot{\gamma})^{a}]^{(1-n)/a}} \tag{1.5}$$

where n is the traditional power-law constant.

1.2.2. Temperature and Pressure Dependency

In 1883 Barus [4] carried out high pressure experiments with "sea glue" using an apparatus similar to a capillary rheometer and analyzed the data using Poiseuille's law. He suggested that the form of the relationship between the viscosity and pressure is that shown in Equation 1.6:

$$\log\eta_0=a+\beta P \tag{1.6}$$

In 1903 de Guzmán [5] proposed the following form of the relationship between the viscosity and temperature:

$$\log\eta_0=a'-\frac{B}{T} \tag{1.7}$$

Only much later were such relationships derived theoretically.

1.2.2.1. Two theories of temperature and pressure dependency

Knowledge of the pressure and temperature dependence of the rheological properties of polymer melts is important for understanding the mechanism of the flow process and the relation between molecular structure and rheological behavior. Two approaches have been proposed to describe the pressure and temperature dependence of the rheological properties of polymers. Both approaches involve the concept of free volume, but one is associated with the change of reaction rate with pressure and temperature, while the other is based on the change of free volume with pressure or temperature. Each approach considers the flow mechanism in a different way, and their predictions and applicable operating ranges are thus different. Figure 1.3 summarizes the difference between the two approaches.

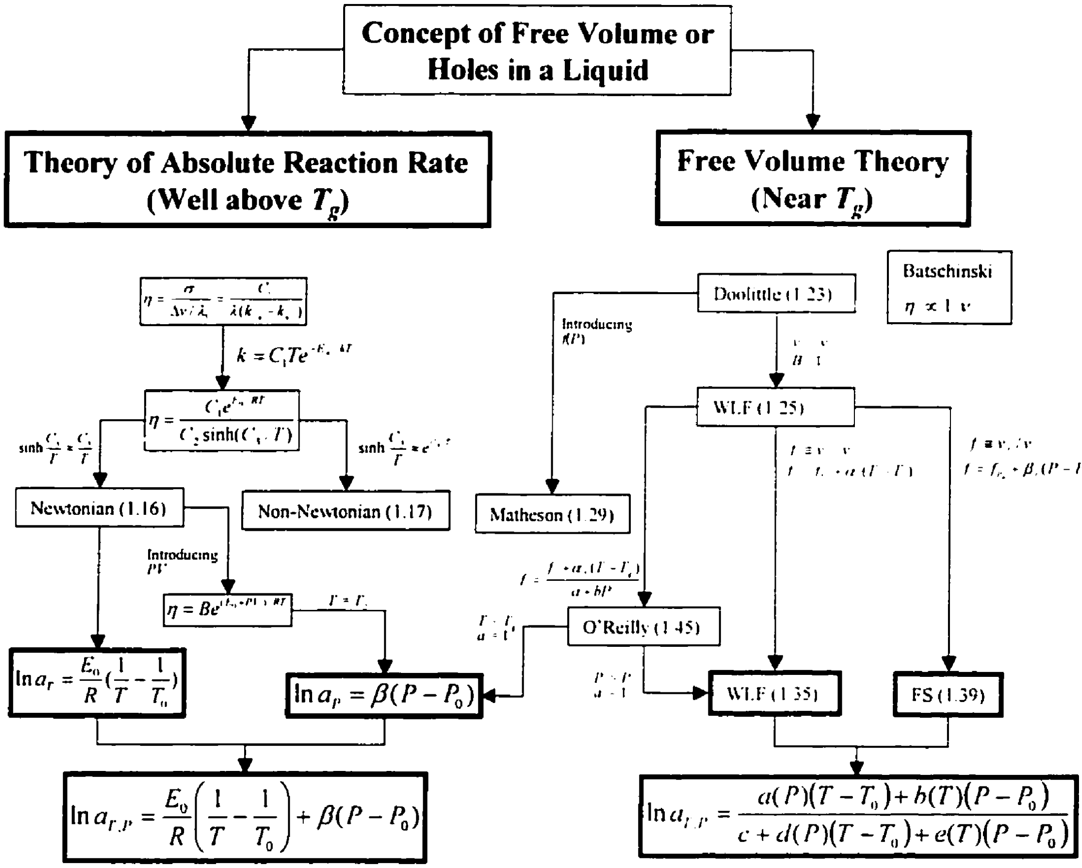

Figure 1.3. Schematic diagram of derivation and relationship between two approaches.

1.2.2.1.1. The absolute rate theory

The theory of absolute rates of chemical reaction was developed after Arrhenius [6] proposed the concept of an activated molecule in 1889. In the 1930's researchers tried to apply the concept of potential energy barriers to physical problems involving viscosity, diffusion, and plasticity. They combined Arrhenius' equation, which is the relationship between chemical reaction rate and temperature, with equations that describe physical flow process to describe the temperature dependency of the viscosity. The theory assumes that a liquid contains free volume or holes that jump or move about in a material, and flow results from these jumps, which occur with the same probability in every direction. This situation is treated as a process of transporting a molecule from one equilibrium position to another over a potential barrier [7], and the process is thus similar to a chemical reaction (Fig. 1.4). The theory also assumes that while the potential barrier changes with pressure but not temperature, the rate changes with both P and T.

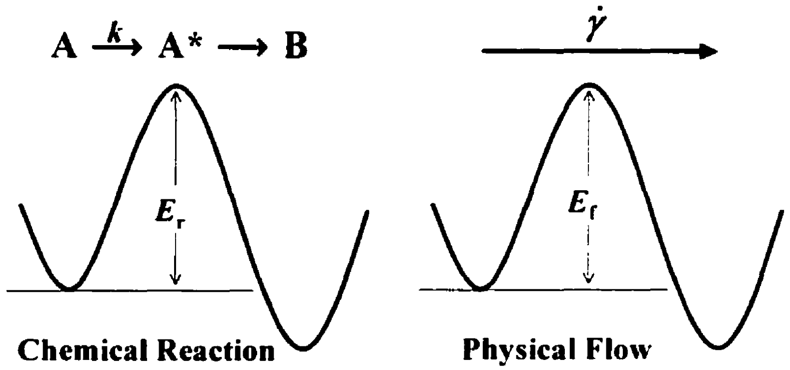

Figure 1.4. Similarity of energy profiles of the paths of a chemical reaction system and a physical flow process.

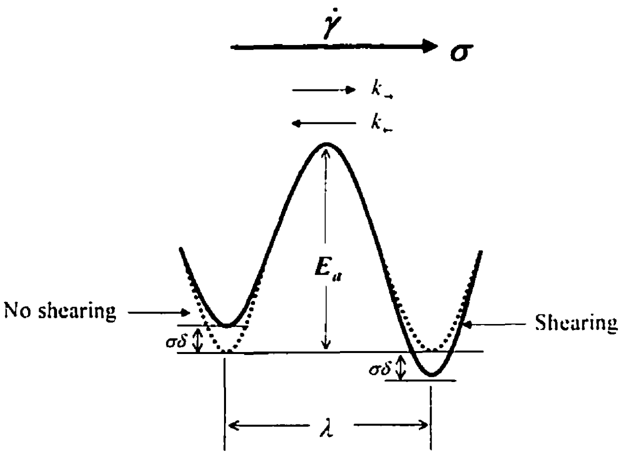

Figure 1.5. Energy profile for the path of a flowing molecule.

If no velocity gradient exists in a liquid sample, the energy profile can be expressed by the dashed curve in Fig. 1.5. A molecule will diffuse equally to the right or to the left at a rate, k_1, having units of reciprocal time [7]:

$$k_1 = C_1 T e^{-\varDelta E_a / kT} \tag{1.8}$$

where T is the absolute temperature, k is the Boltzman constant, C_1 is a constant, and $\triangle E_a$⁽¹⁾ is the activation energy for diffusion; there is no net flow. If a shearing force is applied to the right, there will be a decrease in the activation energy of $\sigma\delta$ in the direction to the right, and an equal increase in the opposite direction. The rates of the flow in each direction are:

$$k\ . = C_1 T e^{-(\varDelta E_a - \sigma\delta)/kT} = k_1 e^{\sigma\delta/kT} \tag{1.9}$$

$$k.\ = C_1 T e^{-(\varDelta E_a + \sigma\delta)/kT} = k_1 e^{-\sigma\delta/kT} \tag{1.10}$$

The net velocity is then:

$$\varDelta\nu = \lambda(k\ . - k.\ ) \tag{1.11}$$

where λ is the distance between equilibrium positions in the direction of flow. The viscosity is given by:

$$\eta = \frac{\sigma}{\varDelta\nu/\lambda_1} = \frac{\sigma\lambda_1}{\lambda(k\ . - k.\ )} \tag{1.12}$$

where λ_1 is the perpendicular distance between adjacent layers of molecules. By combining Equations 1.9 to 1.12, Equation 1.12 can be rewritten as:

$$\eta = \frac{\sigma\lambda_1}{\lambda k_1 \sinh(\sigma\delta/kT)} \tag{1.13}$$

Eyring [7] derived equations for Newtonian and non-Newtonian liquids from Equation 1.13. In the Newtonian case $\sigma\delta \ll kT$, and all terms having higher powers than the first in the Taylor series expansion of $\sinh(\sigma\delta/kT)$ are negligible, and $\sinh(\sigma\delta/kT)$ is very close to $\sigma\delta/kT$. Equation 1.13 can then be simplified by

---

(1) $\varDelta E_a$ is the activation energy per molecule, and E_a is the activation energy per mole. Since $k=R/N$, $\varDelta E_a/k = N\varDelta E_a/R = E_a/R$.

eliminating the stress term:

$$\eta = \frac{\lambda_1 kT}{\lambda k_1 \delta} \tag{1.14}$$

In the case of a non-Newtonian fluid, if $\sigma\delta$ is sufficiently large, the diffusion flow to the left can be neglected in comparison with the flow in the shearing direction, and $\sinh(\sigma\delta/kT)$ can be approximated by $e^{\sigma\delta/kT}$:

$$\eta = \frac{\sigma\lambda_1 k}{\lambda k_1 e^{\sigma\delta/kT}} \tag{1.15}$$

Substituting Equation 1.8 into Equations 1.14 and 1.15 gives the following equations:

$$\eta = \frac{\lambda_1 k e^{\Delta E_a/kT}}{\lambda\delta C_1} \quad \text{for Newtonian liquids} \tag{1.16}$$

$$\eta = \frac{\sigma\lambda_1 k e^{(\Delta E_a - \sigma\delta)/kT}}{\lambda T C_1} \quad \text{for non}-\text{Newtonian liquids} \tag{1.17}$$

Laidler and Eyring [8] derived the following equation from Equation 1.16(2):

$$\eta = \left(\frac{hN}{V} e^{-\Delta S^*/R}\right) e^{\Delta H^*/RT} \tag{1.18}$$

where h is Planck's constant, N is Avogadro's number, V is the molar volume, and ΔS^* and ΔH^* are the entropy and enthalpy for viscous flow. Eyring assumes that the molar volume varies little with temperature and that ΔS^* is also independent of temperature. The terms inside the brackets in Equation 1.18 can thus be reduced to a constant, and the equation can be rewritten as:

$$\eta = Be^{E_0/RT} \tag{1.19}$$

where E_0 is the activation energy for flow, and B is a constant. This kind of relationship was proposed empirically by de Guzmán [5], da Andrade [9], and Arrhenius [10] and was later derived theoretically by Frenkel [11] and da Andrade [12].

Ewell and Eyring [13] introduced a pressure term by assuming that additional

---

(2) Only the viscosity equations for Newtonian liquids will be discussed further, since the pressure dependence of the viscosity will be discussed in terms of the zero-shear viscosity.

work must be done against external pressure in order to make a hole in a liquid. The additional work is a result of the additional activation energy necessary for a molecule to overcome the increased barrier to flow (Fig. 6). The quantity PV was thus added to the activation energy:

$$\eta = Be^{(E_0 + PV)/RT} \tag{1.20}$$

From Equation 1.16 Laidler and Eyring [8] also derived the following equation involving a free volume without assuming it independent of T and P:

$$\eta = \frac{N}{V}\sqrt{2\pi mkT}\,\sqrt[3]{\nu_f}\,e^{(E_0 + PV)/RT} \tag{1.21}$$

where m is the mass of a molecule, and ν_f is the free volume. However, this equation is rarely used.

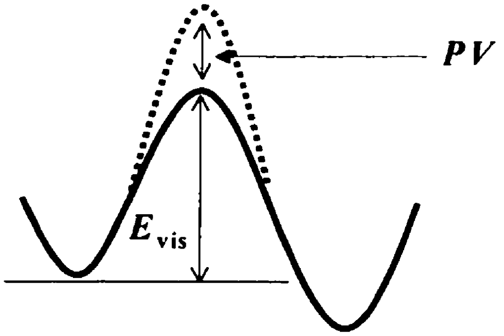

Figure 1.6. Increase of the activation energy due to external pressure.

1.2.2.1.2. The free volume theory

Another approach to the theory of the pressure and temperature dependence of viscosity involves the change of free volume with temperature and pressure. The choice of relationship between free volume and T or P leads to different predictions. The idea that the fluidity of a liquid is due to the presence of free volume was first advanced by Batschinski [14] and extensively developed by Doolittle [15,16,17]. Free volume increases with increasing temperature and decreasing pressure, and fluidity increases with increasing free volume. Batschinski [16] proposed a direct relationship between viscosity and free volume:

$$\eta = \frac{C_2}{\nu_f} = \frac{C_2}{\nu - \nu_0} \tag{1.22}$$

where ν_f is the free volume, ν is the total specific volume, and ν_0 is the specific volume occupied by molecules or the limiting specific volume extrapolated to 0K.

The free volume theory as formulated at present is based on the observations of Doolittle, who measured the viscosities of n-alkanes and found their dependence on free volume. He proposed that specific free volume rather than temperature should be the primary variable for viscosity. Such a relationship is expressed by the following equations, often called the Doolittle equations:

$$\eta = Ae^{B_0\nu_0/\nu_f} \tag{1.23}$$

$$\ln\eta = A' + B_0\frac{\nu_0}{\nu_f} = A' + B_0\frac{\nu_0}{\nu - \nu_0} \tag{1.24}$$

where A, A', and B_0 are constants. For the temperature to be explicitly introduced into Equation 1.23, the temperature dependence of the free volume is required. Williams, Landel, and Ferry [18] assumed B_0 is unity, and replaced ν_0 with ν since $\nu_f \ll \nu$ and $\nu \simeq \nu_0$:

$$\eta = Ae^{\nu/\nu_f} \tag{1.25}$$

They further suggested the following form for the temperature dependency of the free volume:

$$\nu_f = \nu_{f,g} + \alpha_0\nu(T - T_g) \tag{1.26}$$

where T_g is the glass transition temperature, $\nu_{f,g}$ is the free volume at T_g, ν_f is the free volume at T, and α_0 is the coefficient of thermal expansion of free volume. The following equation is obtained by combining Equations 1.25 and 1.26:

$$\ln\eta = A' + \frac{\nu}{\nu_{f,g} + \alpha_0\nu(T - T_g)} \tag{1.27}$$

This equation is valid when $T_g < T < T_g + 100$℃. It is usually assumed that when

$T < T_g$ the free volume remains unchanged and equal to $\nu_{f,g}$ due to the freezing of the conformation(3) of polymeric chains at temperatures below T_g. Thus, when $T < T_g$, a change of volume occurs only as a result of a change in the volume occupied by the molecules, *i.e.* $\Delta\nu = \Delta\nu_0$.

It is well known that the viscosities of ordinary liquids increase at elevated pressures [19], and the same effect has been observed for polymers [20]. Matheson [21] discussed this behavior qualitatively in terms of the relation between free volume, temperature and pressure. He suggested that an increase of pressure at constant temperature leads to a decrease in ν_0 and that the compressibility of a liquid has the same mathematical form as that found by Bridgman [19] for solids:

$$\nu_0^P = \nu_0(-aP + bP^2) = \nu_0 f(P) \tag{1.28}$$

where ν_0^P is the limiting specific volume of the liquid at the pressure P. Matheson showed that by substituting ν and ν_0 with ν^P and ν_0^P respectively, Equation 1.27 can be rewritten as:

$$\ln\eta = A' + B_0 \frac{\nu_0 f(P)}{\nu^P - \nu_0 f(P)} \tag{1.29}$$

where ν^P is the specific volume of the liquid at the pressure P.

1.2.2.2. Temperature and Pressure Shift Factor

According to the time-temperature superposition principle, viscosity equations can be modified to account for the effect of temperature by dividing the viscosity and multiplying the shear rate by a shift factor, $a_T(T)$ that is defined as:

$$a_T(T) \equiv \frac{\eta_0(T)}{\eta_0(T_0)} b_T \tag{1.30}$$

---

(3) Conformation and configuration are used interchangeably to mean the spatial arrangement of atoms in a molecule. However, in this work these terms have different meanings. A change of conformation requires rotation about a single bond, and a change in configuration requires breaking a bond or reforming a bond.

$$b_T(T) \equiv \frac{T_0\rho_0}{T\rho} \tag{1.31}$$

where T_0 is a reference temperature, ρ_0 is the density at T_0, and ρ is the density at T. Thus, a temperature independent flow curve can be obtained by plotting $\eta(\dot{\gamma})/a_T$ versus $\dot{\gamma}a_T$. Sharda and Tschoegl [22] have shown that ρ_0/ρ should be replaced by $(\rho_0/\rho)^{-\varepsilon}$ where ε is a material parameter. However, because the difference between (ρ_0/ρ) and $(\rho_0/\rho)^{-\varepsilon}$ is quite small, Equation 1.31 is assumed to be valid. Since b_T changes relatively little with temperature in the usual range of rheological measurements, an effective temperature shift factor is:

$$a_T(T) = \frac{\eta_0(T)}{\eta_0(T_0)} \tag{1.32}$$

As long as the temperature is at least 100℃ above the glass transition temperature, an exponential equation based on the absolute rate theory (Equation 1.19) can often be used to describe the temperature shift factor:

$$\ln a_T(T) = \frac{E_0}{R}\left(\frac{1}{T} - \frac{1}{T_0}\right) \tag{1.33}$$

where E_0 is the activation energy for flow. From the glass transition temperature to 100℃ above the glass transition temperature, the WLF equation, based on the free volume theory, provides a better fit to data [18]:

$$\ln a_T(T) = \frac{-B_0(T-T_0)}{\frac{\nu_{f_0}}{\nu}\left[\frac{\nu_{f_0}}{\nu}\frac{1}{\alpha_0} + (T-T_0)\right]} \tag{1.34}$$

where ν_{f_0} is the free volume at T_0. By using the fractional free volume, $f \equiv \nu_f/\nu$, Equation 1.34 can be rewritten in the following well-known form:

$$\ln a_T(T) = \frac{-(B_0/f_{T_0})(T-T_0)}{\frac{f_{T_0}}{\alpha_0} + (T-T_0)} \tag{1.35}$$

where B_0 is an empirical constant usually taken to be unity, f_{T_0} is the fractional free volume at T_0, and α_0 is the isobaric compressibility of the free volume, which equals $(1/v)(\partial v_f/\partial T)_P$.

By analogy, an effective pressure shift factor can be expressed as:

$$a_P(P) = \frac{\eta_0(P)}{\eta_0(P_0)} \tag{1.36}$$

Well above the melting temperature an exponential equation, which can be derived from Barus' exponential equation (1.6), can often be used to describe the pressure shift factor:

$$\ln a_P(P) = C'(P - P_0) \tag{1.37}$$

where C' is a constant often called the pressure coefficient, β_0 and is given by:

$$\beta_0 = \frac{1}{\eta_0}\left(\frac{d\eta_0}{dP}\right)_T \tag{1.38}$$

The pressure coefficient is a function of molecular structure but not of T, P, or $\dot{\gamma}$. Ferry and Stratton [23] have suggested an analog of Equation 1.35 to describe the pressure shift factor at temperatures near T_g:

$$\ln a_P(P) = \frac{-(B_0/f_{P_0})(P - P_0)}{\dfrac{f_{P_0}}{\beta_f} - (P - P_0)} \tag{1.39}$$

where f_{P_0} is the fractional free volume at P_0, and β_f is the isothermal compressibility of the free volume, $(1/v)(\partial v_f/\partial P)_T$, which is independent of P. This expression predicts qualitatively the well-known increase in viscosity and relaxation time with pressure. If it is quantitatively applicable, a plot of $(P-P_0)/\log a_p$ against $(P-P_0)$ will be linear, and the parameters can be determined from the slope and intercept.

To take into account the effects of both temperature and pressure, the general shift factors are defined as:

$$a_{T,P}(T, P) \equiv \frac{\eta_0(T, P)}{\eta_0(T_0, P_0)} b_{T,P} \tag{1.40}$$

$$b_{T,P}(T,P) \equiv \frac{T_0 \rho_0^0}{T\rho} \tag{1.41}$$

where ρ_0^0 is the density at T_0 and P_0. However, the ratio $b_{T,P}$ changes relatively little with temperature and pressure, and an effective temperature and pressure shift factor is:

$$a_{T,P}(T,P) = \frac{\eta_0(T,P)}{\eta_0(T_0,P_0)} \tag{1.42}$$

For fully molten polymers a general shift factor is often described by the combination of Equations 1.33 and 1.37:

$$a_{T,P}(T,P) = \exp\left[\frac{E_0}{R}\left(\frac{1}{T} - \frac{1}{T_0}\right)\right]\exp[\beta(P-P_0)] \tag{1.43}$$

For other cases, the Fillers-Moonan-Tschoegl equation [24,25], based on the free volume theory, was developed to describe time-temperature-pressure superposition:

$$\ln a_{T,P}(T,P) = -\frac{B_0}{f_{T_0P_0}} \frac{\alpha_f(P)[T-T_0] - \beta_f(T)[P-P_0]}{f_{T_0P_0} + \alpha_f(P)[T-T_0] - \beta_f(T)[P-P_0]} \tag{1.44}$$

where $f_{T_0P_0}$ is the fractional free volume at T_0 and P_0, $\alpha_f(P)$is the thermal expansion coefficient of the free volume as a function of P at T_0, and $\beta_f(T)$ is the isothermal compressibility of the free volume at P_0. This equation can be used to predict the viscosity at a given T and P and reduces to Equation 1.35 at $P = P_0$ and to Equation 1.39 at $T = T_0$.

However, O'Reilly [26] found that a plot of $\ln(a_{T,P})$ versus P was linear while $\ln(a_{T,P})$ versus T exhibited considerable curvature as described by the WLF equation (1.35). He proposed a general shift factor that is different from Equation 1.44 in that it has no pressure term in the denominator:

$$\ln a_{T,P}(T,P) = -\frac{\alpha_f a[T-T_g] - bf_0[P-P_0]}{f_0[f_0 + \alpha_f(T-T_g)]} \tag{1.45}$$

where a and b are fitting constants, f_0 is the fractional free volume at a reference state, and α_f is the isobaric compressibility of the free volume. From this equation

a_T and a_P are given by the following equations:

$$\ln a_T(T) = \frac{-C_1(T-T_g)}{C_2 + C_3(T-T_g)} \tag{1.46}$$

$$\ln a_P(P) = C_4(P-P_0) \tag{1.47}$$

where C_1, C_2, C_3, and C_4 are constants. Equation 1.46 is the WLF equation, and Equation 1.47 is the Barus' equation (1.6). Pressure and temperature are expected to have an important effect on any characteristic times that describe the melt's behavior. For example, referring to the Cross model (Equation 1.3), it is known that the same shift factor that is useful for viscosity, a_p, also governs the shift of the shear rate. This can be expressed as follows.

$$\lambda(T,P) = a_{T,P}(T,P)\lambda(T_0,P_0) \tag{1.48}$$

Thus, the Cross model can be represented in the following form:

$$\frac{\eta(\dot{\gamma},T,P)}{a_{T,P}(T,P)} = \frac{\eta_0(T_0,P_0)}{1+\left|\lambda(T_0,P_0)a_{T,P}(T,P)\dot{\gamma}\right|^m} \tag{1.49}$$

We see from Equation 1.49 that if $\eta(\dot{\gamma},P,T)/a_{T,P}$ is plotted as a function of $a_{T,P}\dot{\gamma}$, the resulting curve will be independent of temperature and pressure. Such a representation is called a master curve. To generate master curves for other rheological properties, the same shift factor can be used.

1.2.3. Molecular Structure Dependency

The rheological properties of a polymer vary with its molecular structure, *i.e.*, its molecular weight, molecular weight distribution, branching level, and branching distributions. It is of interest to know how these structure parameters and distributions affect rheological properties.

1.2.3.1. Molecular weight and molecular weight distribution

Typically a synthetic polymer contains a mixture of chains with degrees of polymerization that can range from one to millions. The molecular weight distribution is actually a discrete distribution, but it is usually represented as a continuous function (Fig. 1.7). The polydispersity (or polydispersity index) describes the breadth of the molecular weight distribution and is defined as the ratio of two average molecular weights; the weight average molecular weight, M_w, and the number average molecular weight, M_n:

$$\text{Polydispersity} \equiv \frac{M_w}{M_n} \geq 1 \tag{1.50}$$

$$M_n = \frac{\Sigma M_i n_i(M_i)}{\Sigma n_i(M_i)} \tag{1.51}$$

$$M_w = \frac{\Sigma M_i w_i(M_i)}{\Sigma w_i(M_i)} = \frac{\Sigma M_i^2 n_i(M_i)}{\Sigma M_i n_i(M_i)} \tag{1.52}$$

where M_i is the molecular weight of i-mer, $n_i(M_i)$ is the mole fraction of i-mer, and $w_i(M_i)$ $(= M_i n_i(M_i))$ is the weight fraction of i-mer. The discrete functions, M_i, n_i and w_i, are often expressed as continuous functions of molecular weight, M, and average molecular weights can then be expressed in terms of the continuous molecular weight distribution:

$$M_n = \frac{\int_0^\infty Mn(M)dM}{\int_0^\infty n(M)dM} \tag{1.53}$$

$$M_w = \frac{\int_0^\infty Mw(M)dM}{\int_0^\infty w(M)dM} = \frac{\int_0^\infty M^2 n(M)dM}{\int_0^\infty Mn(M)dM} \tag{1.54}$$

M_w is the more appropriate average molecular weight when the contribution of high molecular weight chains dominates a rheological property.

The molecular weight dependence of the zero-shear viscosity of linear, monodisperse polymers is known to be:

$$\eta_0 \cong K_1 M \quad \text{for} \quad M < M_c \tag{1.55}$$

$$\eta_0 \cong K_2 M^a \quad \text{for} \quad M > M_c \tag{1.56}$$

where K_1 and K_2 are proportionality constants, M_c is a critical molecular weight of the polymer, M is the molecular weight, and a is a power law constant. The value of M_c for polyethylene is about 3800 g/mol. At low molecular weight η_0 is proportional to the length of the molecules. At molecular weights above M_c, the increase of η_0 with M^a has been explained in terms of entanglement coupling by Bueche [27]. Bueche found that $a = 3.5$, Berry and Fox [28] suggested 3.4, and the value of 3.6 was proposed for polyethylene by Raju *et al.* [29] and Wood-Adams and Dealy [30]. It was found that η_0 for linear polydisperse polymers depends primarily on the weight average molecular weight and only weakly on the polydispersity [31]:

$$\eta_0 \cong K'_1 M_w \quad \text{for} \quad M_w < M_c \tag{1.57}$$

$$\eta_0 \cong K'_2 M_w^a \quad \text{for} \quad M_w > M_c \tag{1.58}$$

where K'_1 and K'_2 are proportionality constants.

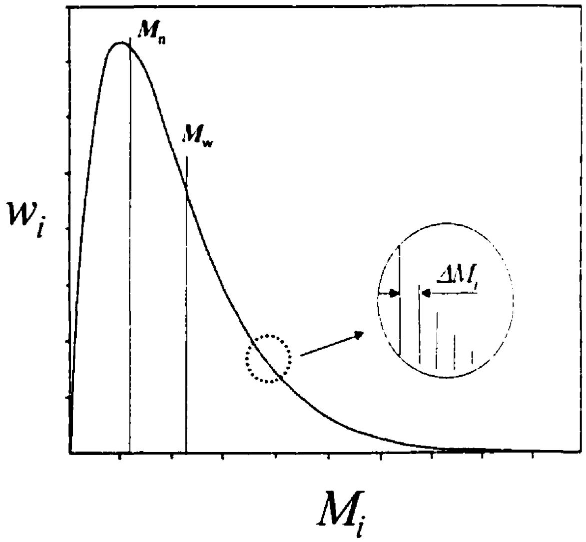

Figure 1.7. A typical molecular weight distribution curve illustrating the actual discrete distribution and its continuous approximation.

1.2.3.2. Long and Short Chain Branching

It has been generally believed that long chain branching (LCB) has an important effect on the rheological properties of polymers but that short chain branching (SCB) has very little effect, often of the order of 1% [32]. Due to entanglements of the backbone as well as long branches at low shear rates, the zero-shear viscosity of a branched polymer is higher than that of a less branched or linear polymer having the same backbone molecular weight. However, at high shear rates the viscosity decreases with increasing shear rate more sharply than less branched or linear polymers. The impact of LCB on rheological properties depends on the number of branch points and the branch length distribution [33]. It has been reported [34] that the presence of both SCB and LCB increases the zero-shear viscosity synergistically. The number of long chain branches can be determined by subtracting the number of short chain branches from the total number of branching points, *i.e.*, the number of methine carbons (Fig. 1.8).

Several methods have been used to detect the level of branching: Temperature rising elution fractionation (TREF) [35], crystallization analysis fractionation (CRYSTAF) [36,37], gel permeation chromatography (GPC) [38], nuclear magnetic resonance (NMR) [39], and rheological data [40]. Carbon 13 NMR considers a branch having more than five carbons to be a long chain branch, because NMR can count the number of carbons, up to five, on a branch [41,42]. From a rheological point of view, a long chain branch is a branch having a molecular weight higher than 2.5M_c

In this work "molecular weight" means the molecular weight of the backbone. It is assumed that the length distribution of LCB is the same as the distribution of the backbones in the same system. This assumption is based on what is known about the branching mechanism during the synthesis of the polymers used [43].

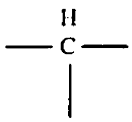

Figure 1.8. A methine carbon, which is a branching point.

1.3. Creep and Creep Recovery

While modified capillary rheometers have been used to determine approximate values of the viscosity at elevated pressures, these instruments are not useful for the determination of viscoelastic properties. The sliding plate rheometer is well-suited to such measurements, because the shear strain is uniform throughout the sample, and it can be easily programmed to generate any desired shear strain as a function of time. In addition, by use of feedback control based on the signal from the shear stress transducer, it is possible to carry out experiments in which the shear stress is the controlled variable. In particular, creep and creep recovery experiments can be carried out in this way.

1.3.1. Creep

In a creep experiment the stress is increased suddenly from 0 to σ_0 at $t=0$, and the strain is recorded as a function of time. Polymeric liquids continue to deform as long as the stress is applied, approaching a steady rate of strain. Data are usually expressed in terms of $J(t)$, the creep compliance, which is independent of stress in the region of linear viscoelasticity:

$$J(t) \equiv \frac{\gamma(t)}{\sigma_0} \tag{1.59}$$

At long times the compliance of a melt becomes linear with time:

$$J(t) \equiv J_s^0 + \frac{t}{\eta_0} \tag{1.60}$$

where J_s^0 is the steady state compliance that is determined by extrapolation of the limiting slope back to $t=0$. Compliance has dimensions of reciprocal modulus, but it is not equal to the reciprocal of the relaxation modulus.

In the nonlinear region, *i.e.*, at sufficiently high stresses, the shear creep compliance depends also on the stress:

$$J(t,\sigma)\equiv\frac{\gamma(t)}{\sigma} \tag{1.61}$$

and at long times:

$$J(t,\sigma)\equiv J_s(\sigma)+\frac{t}{\eta(\sigma)} \tag{1.62}$$

where $J_s(\sigma)$ is the steady state compliance for nonlinear viscoelastic behavior. With increasing stress $J(t,\sigma)$ increases, and $J_s(\sigma)$ decreases [31]. Ye [44] has proposed that the limiting stress for linear behavior is about 10 Pa.

1.3.2. Creep Recovery

At $t=t_0$ during a creep test, if the stress is suddenly decreased to zero, a polymeric liquid recoils in the reverse direction. Figure 1.9 shows the essential features of creep recovery. The recoil strain and recoil function (recovered or recoverable compliance) are defined respectively as follows:

$$\gamma_r(t-t_0,t_0,\sigma)\equiv\gamma(t_0)-\gamma(t) \tag{1.63}$$

$$R(t-t_0,t_0,\sigma)\equiv\frac{\gamma_r(t-t_0,t_0,\sigma)}{\sigma} \tag{1.64}$$

If t_0 is sufficiently long that the creep test has reached steady state, the recoil strain is independent of t_0. The time at which the stress is removed, t_0, can then be set equal to zero. The recoil strain and recoil function then become:

$$\gamma_r(t,\sigma)\equiv\gamma(0)-\gamma(t) \tag{1.65}$$

$$R(t,\sigma)\equiv\frac{\gamma_r(t,\sigma)}{\sigma} \tag{1.66}$$

The ultimate recoil and ultimate recoil function are obtained at sufficiently long times:

$$r_\infty(\sigma)\equiv\lim_{t\to\infty}\gamma_r(t,\sigma) \tag{1.67}$$

$$R_\infty(\sigma)\equiv\lim_{t\to\infty}R_r(t,\sigma) \tag{1.68}$$

In the linear region the creep and creep recovery functions are closely related:

$$J(t) - \frac{t}{\eta_0} = R(t) \tag{1.69}$$

$$J_s^0 = R_\infty^0 \tag{1.70}$$

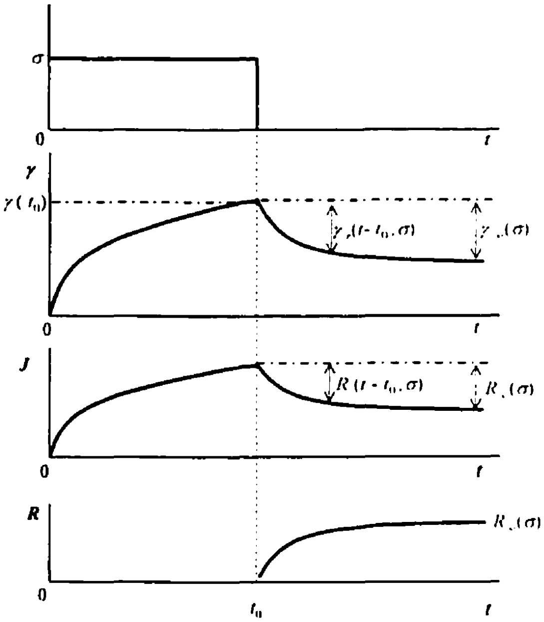

Figure 1.9. Essential features of stress, strain, creep and recoil curves.

1.3.3. Temperature and Pressure Dependency

The creep compliance increases with increasing temperature [45] (Fig. 1.10), but the steady state compliance of a monodisperse, linear polymer decreases with increasing temperature. The steady state compliance of an unentangled melt as a function of M and T is predicted by the Rouse theory [31] to be:

$$J_s^0 = \frac{0.4M}{\rho RT} \quad \text{for} \quad M < M'_c \tag{1.71}$$

where M'_c is a critical molecular weight. The M'_c of polyethylene is about 14400 g/mol. The steady state compliance of a highly entangled polymer is found to be a function only of T [31]:

$$J_s^0 = \frac{0.4 M_c'}{\rho RT} \quad \text{for} \quad M > M_c' \tag{1.72}$$

Wagner and Laun [46] reported that creep compliance and creep recovery curves at various temperatures can be superposed onto a single curve by a horizontal shift along the time axis using a_T, the temperature shift factor from viscosity experiments:

$$\gamma(t/a_T, \sigma, T) \equiv \gamma(t, \sigma, T_0) \tag{1.73}$$

$$\gamma_r(t/a_T, \sigma, T) \equiv \gamma_r(t, \sigma, T_0) \tag{1.74}$$

Usually time-temperature shifting is carried out on a semi log plot [47]. If the $J(t)$ curves are plotted using logarithmic time scales, changing the temperature has the same effect as a horizontal shift by a distance, $\log[a_T(T)]$. Thus, creep compliance data at a higher temperature must be shifted by $-\log[a_T(T)]$ to construct a master curve at the reference temperature (Fig. 1.10). This approach is useful when the extrapolation of the creep curve to short or long times is desired.

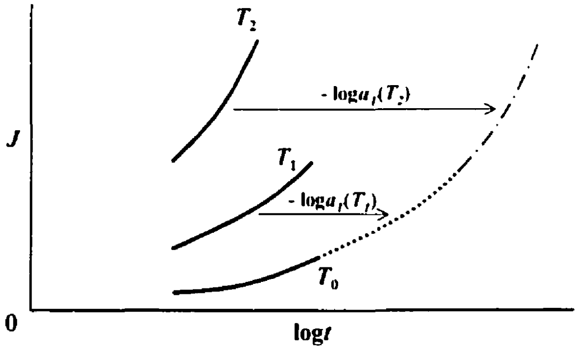

Figure 1.10. Horizontal shifts of creep compliance curves at T_1 and T_2 onto the curve at the reference temperature, T_0 ($T_1, T_2 > T_0$).

Since it is known that the effect of increasing the pressure is similar to that of decreasing the temperature, the same analysis can be used, although there have been very few creep experiments at high pressure:

$$\gamma(t/a_P, \sigma, P) \equiv \gamma(t, \sigma, P_0) \tag{1.75}$$

$$\gamma_r(t/a_P, \sigma, P) \equiv \gamma_r(t, \sigma, P_0) \tag{1.76}$$

1.3.4. Molecular Structure Dependency

The creep compliance of a polymer with a molecular weight higher than a critical molecular weight, M'_c, shows two types of behavior depending on polydispersity. Monodisperse polymers show a plateau compliance, J_S^0 followed by a further increase at longer times, while a polydisperse polymer does not have a plateau compliance (Fig. 1.11) [31].

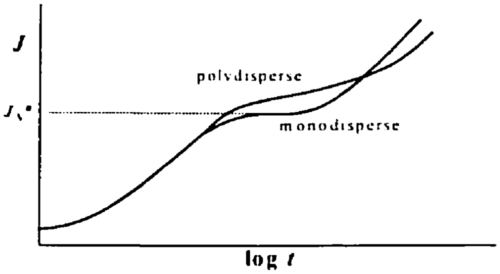

Figure 1.11. Polydispersity effect on the creep compliance curves of high molecular weight polymers.

It is known that J_S^0 of a branched polymer with high molecular weight is higher than that of a linear polymer having the same molecular weight [31]. Moreover, a branched polymer has a higher zero-shear viscosity than a linear polymer having the same backbone molecular weight. This trend holds for various branching levels, as shown in Fig. 1.12.

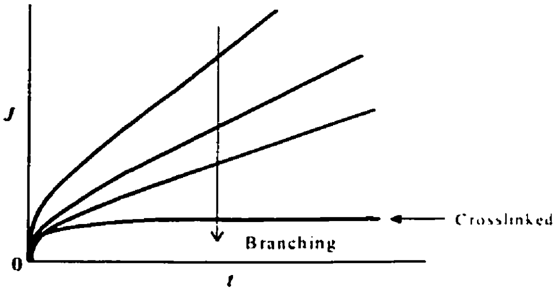

Figure 1.12. The effect of branching level on creep.

References

1. M.M. Cross, in *Polymer Systems: Deformation and Flow*, Wetton and Whorlow, editors, Macmillan, London, 1968.
2. P.J. Carreau, Ph.D. Thesis, Univ. of Wisconsin, Wisconsin, U.S.A., 1969.
3. K.Y. Yasuda, R.C. Armstrong, and R.E. Cohen, *Rheol. Acta* 20:163 (1981).
4. C. Barus, *American J. Science*, XLV:87 (1983).
5. J. de Guzmán, *Anales de la Sociedad Espanola de Fisica Y Quimica* 11:353 (1903).
6. S. Arrhenius, *Zeitschrift für Physickalische Chemie* 226 (1889).
7. H. Eyring, *J. Chem. Phys.* 4:283 (1936).
8. K.J. Laidler and H. Eyring, *The Theory of Rate Processes*, McGraw Hill, New York, 1940.
9. E.N. da C. Andrade, *Nature* 125:309 and 582 (1930).
10. S. Arrhenius, *Meddelanden Från K. Vetenskapsakademiens Nobelinstitut* 3(20):1 (1916).
11. J. Frenkel, *Zeitschrift für Physickalische Chemie* 35:652 (1926).
12. E.N. da C. Andrade, Philosophical Magazine and J. Science 17:497 and 698 (1934).
13. R.H. Ewell and H. Eyring, *J. Chem. Phys.* 5:726 (1938).
14. A.J. Batschinski, *Zeitschrift für Physickalische Chemie* 84:643 (1913).
15. A.K. Doolittle, *J. Applied Physics* 22:1471 (1951).
16. A.K. Doolittle, *J. Applied Physics* 23:236 (1952).
17. A.K. Doolittle, *J. Applied Physics* 28:901 (1957).
18. M.L. Williams, R.F. Landel, and J.D. Ferry, *J. American Chemical Society* 77:3701 (1955).
19. P.W. Bridgman, *The Physics of High Pressure*, Dover Publications, New York, 1931.
20. Von K.H. Hellwege, W. Knappe, F. Paul, and V. Semjonow, *Rhol. Acta* 6:165 (1967).
21. A.J. Matheson *J. Chem. Phys.* 44:695 (1966).
22. S.C. Sharda and N.W. Tschoegl, *J. Rheology* 20:361, (1976).
23. J.D. Ferry and R.A. Stratton, *Kolloid-Zeitschrift* 171:107, (1960).
24. R.W. Fillers and N.W. Tschoegl, *Trans. Society of Rheology* 21:51 (1977)
25. W.K. Moonan and N.W. Tschoegl, *Macromolecules*, 16:55 (1983)
26. J.M. O'Reilly, *J. Polymer Science* 57:429 (1962).

27. F. Bueche, *J. Chemical Physics* 36:2940 (1962).
28. G.C. Berry and T.G. Fox, *Advances in Polymer Science* 5:261 (1968).
29. V.R. Raju, G.G. Smith, G. Marin, J.R. Knox, and W.W. Graessley, *J. Polymer Science* 17:1183 (1979).
30. P.M. Wood-Adams and J.M. Dealy, *Macromolecules*, 33:7481 (2000).
31. J.M. Dealy and K.F. Wissbrun, *Melt Rheology and Its Role in Plastics Processing*, Chapman and Hall, London, 1995.
32. A.C. Ouano, E.M. Barrall II, and Julian F. Johnson, "Gel Permeation Chromatography", Chapter 6 of *Polymer Molecular Weights Part II*, edited by P.E. Slade, Jr., Marcel Dekker, New York, 1975.
33. P.M. Wood-Adams, J.M. Dealy, A.W. deGroot, and O. D. Redwine, *Macromolecular* 33:7489 (2000).
34. P.M. Wood-Adams and S. Costeux, in preparation (2001).
35. L. Wild, T.R. Ryle, D.C. Knobeloch, I.R. Peat, *J. Polymer Science* 20:441 (1982).
36. B. Monrabal, *J. Applied Polymer Science* 52:491 (1994).
37. B. Monrabal, J. Blaco, J. Nieto, and J.B.P. Soares, *J. Polymer Science: Part A: Polym. Chem.* 37:89 (1999).
38. Th.G. Scholte, N.L.J. Meijerink, *Br. Polymer J.* 9:133 (1977).
39. J.C. Randall, *J. Macromolecular Science, Rev. Macromol. Chem. Phys.*, C29:201 (1989).
40. P.M. Wood-Adams and J.M. Dealy, *J. Rheology* 40:761 (1996).
41. J.C. Randall, *J. Polymer Science* 11:275 (1973).
42. Q.T. Pham, R. Pétiaud, H. Waton, and M.-F. Llauro Darricades, *Proton and Carbon NMR Spectra of Polymers*, Penton Press, London, 1991.
43. D. Beigzadeh, Personal communication 2000.
44. Y. Ye, M.Eng. Thesis, McGill University, Montreal, Canada, 2001.
45. P.E. Tomlins, B.E. Read, and G.D. Dean, *Polymer* 35:4376 (1994).
46. M.H. Wagner and H.M. Laun, *Rheol. Acta* 17:138 (1978).
47. R.W. Whorlow, *Rheological Techniques*, Ellis Horwood, New York, 1980.

Chapter 2. High-Pressure Rheometers

There are many kinds of rheometer for atmospheric pressure measurements but only a few that are capable of operation at high pressure. Two types of rheometer have been used for high pressure studies: pressure-driven rheometers, in which flow is generated by a pressure drop, and drag flow rheometers, in which one bounding wall moves relative to another to generate the shearing deformation. A pressure-driven rheometer forces the sample through a capillary or slit, and the resulting pressure drop is measured. Such a unit can be used to measure the approximate viscosity at high shear rates, but because the pressure and shear rate are neither uniform nor independent, these instruments are not useful for viscoelasticity studies and are not ideal for the study of the effect of pressure on viscosity. A drag flow rheometer, on the other hand, such as a concentric cylinder rheometer, generates a deformation that is independent of the applied pressure. However, seal friction, end effects, and flow instability limit its usefulness at high pressures and shear rates. Table 2.1 lists the various high-pressure rheometers that have been used in the past. Figure 2.1 shows the velocity and the stress profiles in the two types of instrument.

The stress profiles are material-independent, and these can be derived from Cauchy's equations:

$$\rho \frac{D\vec{v}}{Dt} = -\rho g \nabla h - \nabla P + \nabla \cdot \vec{\tau} \tag{2.1}$$

For steady-state, fully-developed flow, Equations 2.1 can be reduced to the following equations for pressure driven flow in a slit and for simple shear (drag) flow:

$$0 = -\frac{\partial P}{\partial x} + \frac{\tau_{yx}}{\partial y} \qquad \text{Slit flow} \tag{2.2}$$

$$0 = \frac{\tau_{yx}}{\partial y} \qquad \text{Simple shear flow} \tag{2.3}$$

Table 2.1. Summary of High-Pressure Rheometers.

Type	Feature*	Researchers	Year	P (MPa)	T_{max}(°C)	$\dot{\gamma}$ (s^{-1})	Comments*			
							1	2	3	4
Sliding Plate	SST	Koran & Dealy	1999	0 ~ 70	225	$1 \cdot 10^{-3} \sim 5 \times 10^{2}$				×
Couette	Rotating Disk	Mooney	1934	Nr	100	Nr			×	
		Semjonow	1962	0.1 ~ 152	200	$6 \cdot 10^{-3} \sim 5 \times 10^{2}$			×	
		Cogswell	1973	0.1 ~ 300	300	0.5 ~ 25			×	
	Laser	Bair *et al.*	1993	0.1 ~ 1000	200	Nr ~ 10^{6}			×	
	Magnedrive	Khandare *et al.*	2000	0.1 ~ 7.6	500	Nr			×	
Falling sphere		Foltz *et al.*	1973	0.1 ~ 100	220	Nr				
	Magnetic force	Mattischek & Soeczak	1994	0.1 ~ 100	70	Nr				
Capillary	2B · 2P	Westover	1961	0.1 ~ 172	300	$1 \sim 2 \times 10^{3}$	×	×		
	2B · 2P	Karl	1979	0.1 ~ 500	200	Nr ~ 5×10^{2}	×	×		
	2D · 1NV	Driscoll & Bogue	1990	0.1 ~ 124	Nr	Nr	×	×		
	2B · Pin	Baker & Thomas	1993	0.1 ~ 207	300	Nr ~ 2.5×10^{3}	×	×		
	2B · 2P	Mackley *et al.*	1995	0.1 ~ 25	190	$0.1 \sim 2 \times 10^{5}$	×	×		
	2D	Chakravorty *et al.*	1996	0.1 ~ 152	200	Nr ~ 4×10^{3}	×	×		
	2D · 1V	Binding *et al.*	1998	0.1 ~ 70	230	$50 \sim 2.5 \times 10^{3}$	×	×		
Slit	3PT	Laun	1983	0.1 ~ 200	Nr	$0.1 \sim 1 \times 10^{5}$	×			
	2B · 2P · 3PT	Kadijk & Van den Brule	1994	0.1 ~ 179	300	Nr ~ 3×10^{3}	×			
	9PT	Langelaan	1994	Nr	Nr	50 ~ 3150	×			

* Legend

B: barrel, P: piston, D: die, NV: needle valve, V: valve, PT: pressure transducer, and SST: shear stress transducer

1: Generates inhomogeneous flow

2: Requires end corrections

3: Requires edge corrections

4: Can be used to study viscoelasticity

Nr: Not reported

where τ_{yx} is the shear stress, σ. The above equations show that the shear stress in a slit flow is a linear function of y, while that in a simple shear flow is constant. However, the velocity profile for pressure flow depends on the properties of the sample, while in simple shear flow it is independent of fluid properties.

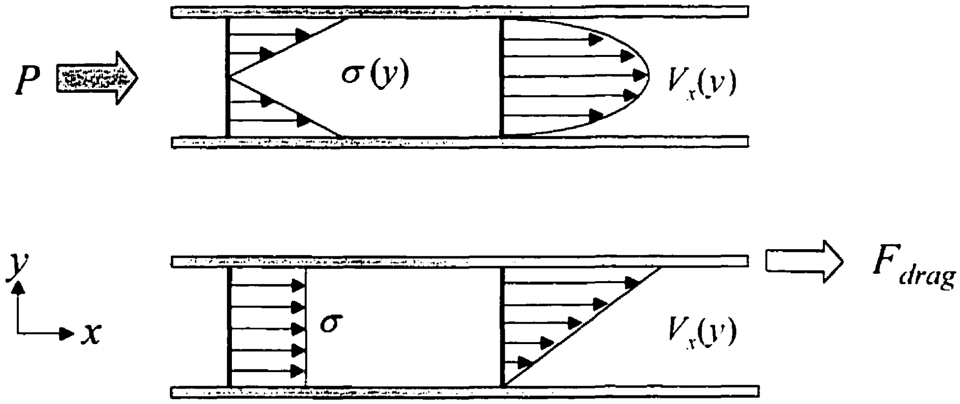

Figure 2.1. The stress and the velocity profiles of pressure-driven flow and drag flow.

2.1. Pressure-driven Rheometers

A rheometer based on pressure-driven flow consists of a heated barrel, a piston or pressurization system, and a die. A capillary rheometer has a circular die, and in a slit rheometer it is a thin rectangular slit. A moving piston or pressurization system generates flow in the die, and the resulting pressure drop is measured.

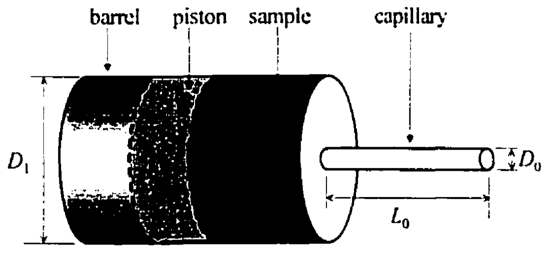

Figure 2.2. Geometry of a capillary rheometer.

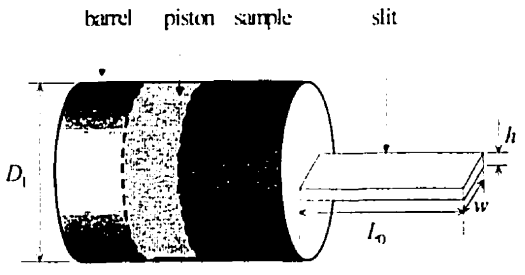

Figure 2.3. Geometry of a slit rheometer.

Capillary and slit rheometers are popular for measurements at high shear rates, since they simulate to some degree flows occurring in plastics processing. However, the shear stress and the shear rate must be inferred indirectly from the driving pressure and volumetric flow rate. Since the pressure and shear rate are inhomogeneous, the molecules in a sample will have various pressure and deformation histories.

2.1.1. High Pressure Capillary Rheometer

A capillary rheometer consists of a barrel, a piston, and a capillary. Data from a capillary rheometer are usually reported in terms of the wall shear stress, σ_w, and the wall shear rate, $\dot{\gamma}_w$. However, since those quantities can only be inferred from the measured pressure drop and flow rate, several assumptions must be made in the treatment of the raw data. The Bagley end correction [1] is often used to obtain σ_w, and the Rabinowitch correction [2] is used to estimate $\dot{\gamma}_w$. Figure 2.4 [3] shows the pressure distribution in a capillary rheometer, where P_d is the driving pressure, P_a is the pressure at the exit, ΔP_{ent} is the entry pressure drop, ΔP_{cap} is pressure drop in the capillary, and ΔP_{ex} is the exit pressure drop. The two excess pressure drops, ΔP_{ent} and ΔP_{ex}, are related to the elasticity of the melt [1].

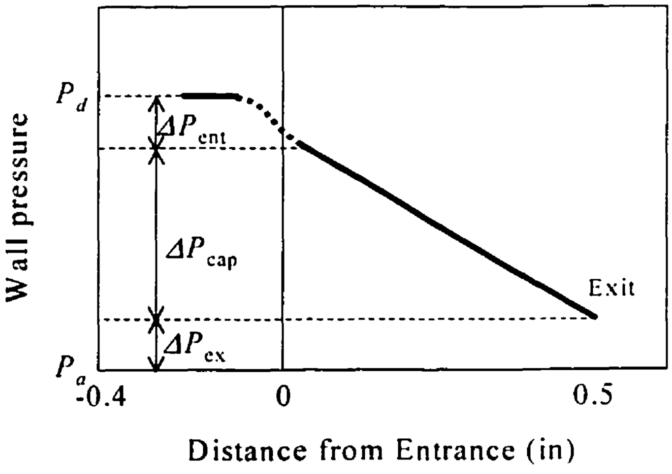

Figure 2.4. Pressure distribution in a capillary rheometer [3].

The Bagley end correction is used to correct for the excess pressure drops, and the true wall shear stress is given by:

$$\sigma_w = \frac{P_d}{2(L_0/R + e)} \tag{2.4}$$

where L_0 is the length of the capillary, R is $D_0/2$, and e is the Bagley end correction, which is the intercept on the L_0/R axis of a P_d versus L_0/R plot, *i.e.*, a Bagley plot. The wall shear rate can be obtained from the apparent shear rate by use of the Rabinowitch correction. The apparent shear rate is the shear rate that would obtain for a Newtonian fluid:

$$\dot{\gamma}_A \equiv \left(\frac{4Q}{\pi R^3}\right) \tag{2.5}$$

where Q is the flow rate. The Rabinowitch correction takes into account the shear rate dependence of the viscosity and gives the true wall shear rate, $\dot{\gamma}_w$:

$$\dot{\gamma}_w = \left(\frac{3+b}{4}\right)\dot{\gamma}_A \tag{2.6}$$

where

$$b \equiv \frac{d(\log \dot{\gamma}_A)}{d(\log \sigma_w)} \tag{2.7}$$

High-pressure capillary rheometers are similar in basic design to standard instruments, but do not exhaust to the atmosphere. Westover [5] installed a second barrel and piston at the exit of the capillary to provide independent control of the hydrostatic pressure and the pressure drop driving the flow. The primary piston

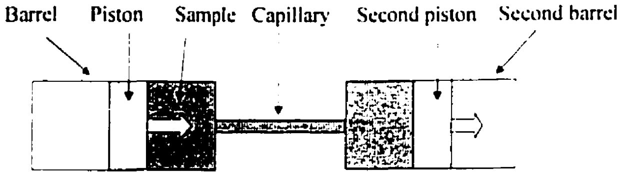

Figure 2.5. Schemetic of the high-pressure capillary rheometer with a double piston system [5].

pressurizes the sample, while the secondary piston is stationary until the desired pressure is reached. Both pistons are moved at the same speed to obtain the desired flow rate. Karl [6] built a double-piston, high-pressure capillary rheometer with pressure transducers installed at both ends of the capillary for measurements up to 500 MPa.

Driscoll and Bogue [7] used two dies: upstream and downstream (Fig. 2.6). They installed a needle valve between them to make the downstream pressure independent of Q. The pressure drop was obtained from the pressure in the barrel and the pressure measured by the pressure transducer in the downstream chamber.

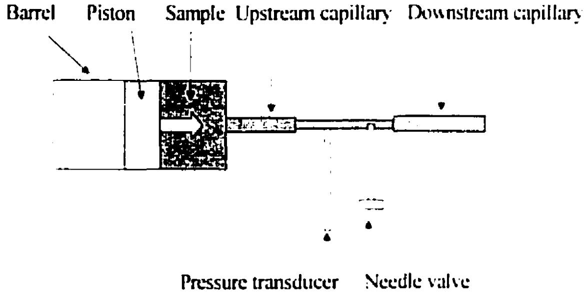

Figure 2.6. Schemetic of the high-pressure capillary rheometer with two dies and a needle valve [7].

Baker and Thomas [8] used two barrels but only one piston and a spirally grooved pin to control the pressure level in the die (Fig. 2.7). The pin partially blocks the second barrel at the exit of the die, and the length of the pin and the groove size control the pressure level in the die by adjusting the resistance to the flow in the second barrel.

Mackley *et al.* [9] developed a "Multi-pass Rheometer" able to pump melt in either direction through a capillary. The basic configuration is similar to that of the Westover rheometer, but the two pistons are driven by independent servo-hydraulic actuators, which can move separately or in unison. Forward, backward, and oscillatory flows can thus be generated.

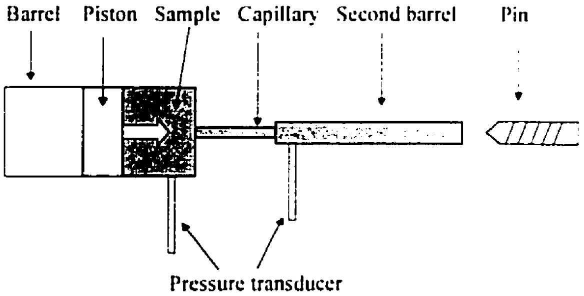

Figure 2.7. High-pressure capillary rheometer with two barrels, a piston, and a pin [8].

Chakravorty *et al.* [10] used a second capillary to create additional flow resistance (Fig. 2.8). Pressure transducers mounted in the barrel and at the exit of the upper capillary are used to determine the pressure drop in the upper capillary.

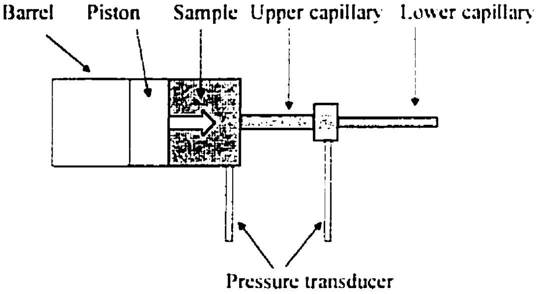

Figure 2.8. Schemetic of the high-pressure capillary rheometer with two dies [10].

Binding *et al.* [11] used a rheometer similar to that of Baker and Thomas (Fig. 2.9), but they used a conical secondary die and a conical valve instead of a pin to control the back pressure. A Teflon™ washer was used on the piston to eliminate leakage.

2.1.2. High Pressure Slit Rheometer

The hydrostatic pressure varies along the length of a capillary die, but it is difficult to determine precisely the local pressure gradient, which is necessary for

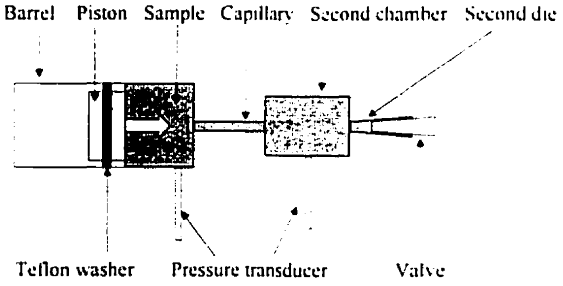

Figure 2.9. Schemetic of the high-pressure capillary rheometer with a conical die and valve [11].

the determination of the viscosity. If a slit die is used, however, pressure transducers can be installed directly in the wall of the slit, and the pressure distribution in the die can be determined. However, a correction for the wall shear rate is still required.

The wall shear stress is given by:

$$\sigma_w = \left(\frac{-\Delta P}{L} \right) \frac{h}{2} \tag{2.8}$$

where ΔP is the pressure drop for a slit of length L. The wall shear rate is given by [12]:

$$\dot{\gamma}_w = \left(\frac{6Q}{h^2 w} \right) \left(\frac{2+\beta}{3} \right) \tag{2.9}$$

where:

$$\beta \equiv \frac{d[\log(6Q/wh^2)]}{d[\log(\sigma_w)]} \tag{2.10}$$

Laun [13] used a pressurized slit rheometer (Fig. 2.10) in which the pressure was measured by three pressure transducers. No Bagley correction was required.

Kadijk and Van den Brule [14] used a double barrel and piston system (Fig. 2.11). It is possible to generate a reverse flow and to carry out multiple experiments on the same sample by controlling the two pistons independently.

Langelaan *et al.* [15] developed a slit rheometer (Fig. 2.12) with nine pressure transducers to investigate the nonlinearity of the pressure distribution in a slit die, and they used an injection cylinder and extruder instead of a piston.

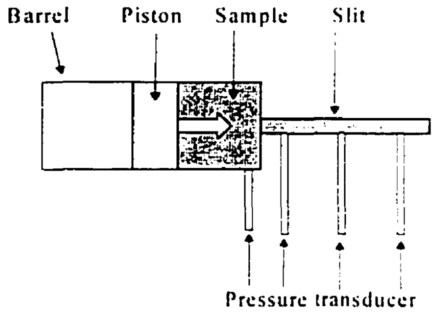

Figure 2.10. Schemetic of the high-pressure slit rheometer of Laun [13].

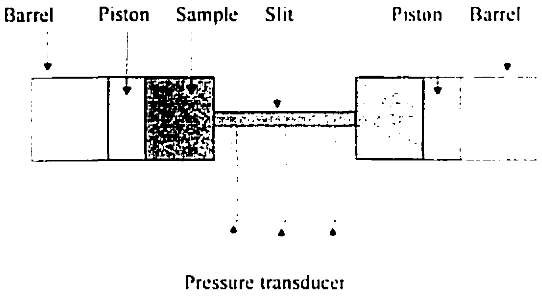

Figure 2.11. Schemetic of the high-pressure slit rheometer with a double piston system [14].

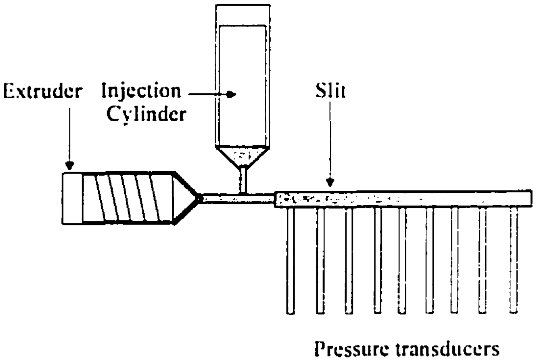

Figure 2.12. Schemetic of the high-pressure slit rheometer with nine pressure transducer [15].

2.2. Drag Flow Rheometers

The advantage of drag flow rheometers is that the hydrostatic pressure is independent of the force driving the deformation, and the shear rate and hydrostatic pressure can thus be controlled independently. The pressure is uniform throughout the sample, but corrections may be required for some geometries.

2.2.1. High Pressure Couette Flow Rheometer

A concentric cylinder (Couette) rheometer consists of two concentric cylinders, a rotational drive, and a torque measuring device. The sample fills the gap between the two cylinders, and one cylinder is rotated. The shear rate is obtained from the rotational speed, while the torque is used to calculate the shear stress. Stress relaxation experiments can also be carried out.

Mooney [16] developed a "Plastometer" to characterize raw rubbers (Fig. 2.13). The upper platen is removed, and a rubber sample is placed around the rotor. After the platen is replaced, the sample is heated. Applying hydrostatic pressure to the cavity allows high-pressure measurements to be made. This instrument is used to determine the "Mooney viscosity", which is proportional to the torque rotation after a certain time has passed [17].

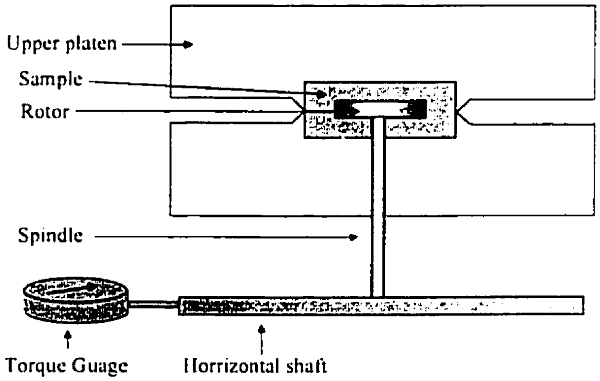

Figure 2.13. Schemetic of a rotating disk or Mooney viscometer [16].

Semjonow [18] used a a pressurized Couette rheometer (Fig. 2.14). A sample is pumped into the gap between the two cylinders, and the desired pressure is generated by means of a ram. The drive rotates the outer cylinder, and the the torque on the inner cylinder is measured. However, Highgate and Whorlow [19] have shown that end effects make a substantial contribution to the measured torque in such a device. They defined the end effect in terms of an increase in the effective cylinder length due to the ends and suggested several methods to avoid or minimize end effects.

Cogswell [20] used a Couette flow viscometer similar to that of Somjonow and pointed out that there are substantial effects of secondary flow, but he argued that the rheometer was useful even with end effects and secondary flow.

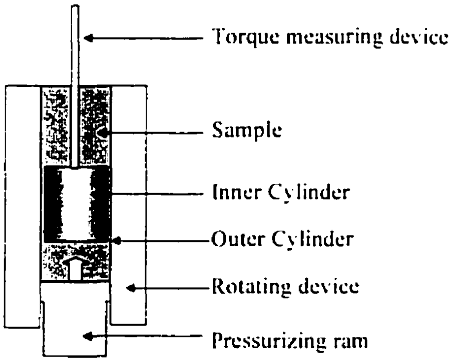

Figure 2.14. Schemetic of the Semjonow high-pressure concentric cylinder rheometer [18].

Bair *et al.* [21] used a Couette viscometer to study the rheological properties of lubricants at high pressure (Fig. 2.15). They visualized the liquid flow at high pressure by means of a "High Pressure Flow Visualization Cell". Bair *et al.* [22] developed another high-pressure Couette viscometer in which a laser was used to measure the torque more precisely than is possibile with mechanical or electrical sensors. While the high pressure may deform the windows, and the deformation might affect the laser beam and torque measurements, these possibilities were not discussed in the paper.

Recently, Khandare *et al.* [23] developed a Couette type "High-temperature High-pressure Rheometer" for the rheological investigation of pitch (Fig. 2.16). The most remarkable feature of this rheometer is a magnetic rotational drive system. The motor generates the torque, which is transmitted to the spindle by a "Magnedrive". Leak-proof rotation of the spindle at high pressure is thus possibile. Taylor instability was not a problem, because the maximum Taylor number was fifty times smaller than the Taylor number for instability. Macosko [24] argued that the Weissenberg number, Wi_{cr}, is more important for instability in the case of a viscoelastic fluid, but Khandare *et al.* did not discuss the role of this parameter.

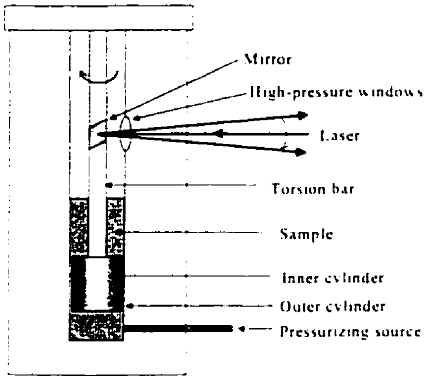

Figure 2.15. Schemetic of the high-pressure concentric cylinder rheometer with a laser tool [21].

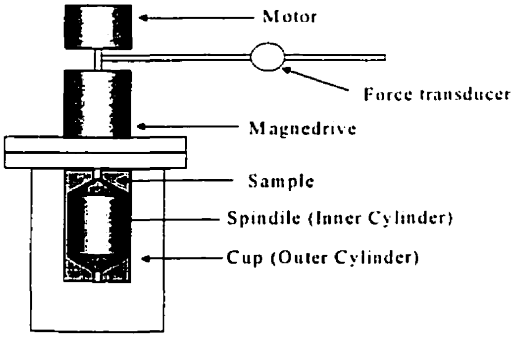

Figure 2.16. Schemetic of the high-pressure concentric cylinder rheometer with a magnedrive [23].

2.2.2. High Pressure Falling Sphere Viscometer

Falling sphere viscometers have been used for the measurement of the pressure dependence of the zero-shear viscosity, which is determined by measuring the terminal velocity of a sphere falling in pressurized melt. No dynamic seals are required, and the apparatus is easy to construct and operate. A falling sphere viscometer is not suitable for the study of viscoelasticity, but it can be used to determine the very important rheological property, η_0, at high pressure.

Foltz *et al.* [25] used a falling sphere viscometer in which the driving force is gravity. The experiments take at least one day, during which time the sample may degrade due to the long exposure to high temperature.

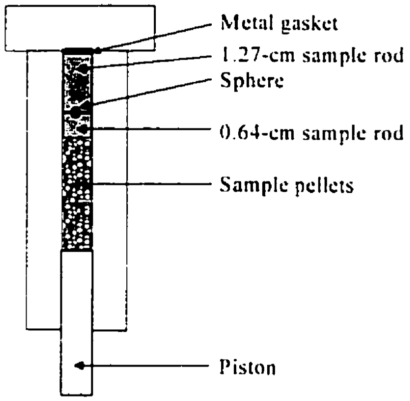

Figure 2.17. Schemetic of the high-pressure falling sphere viscometer [25].

Sobczak [26] developed a falling sphere viscometer in which the driving force is a magnetic field. A laser beam is used to measure the displacement of the sphere. The magnetic force generates faster movement of the sphere than is possible using only gravity and reduces the time required for a measurement. Thermal degradation is thus avoided. Gahleitner and Sobczak [27] used a falling sphere viscometer to determine and investigated the shear rate dependence of the viscosity. They also used the start-up behavior of the zero-shear viscosity to apply the principle of Gleissle's mirror relation [28]:

$$\eta(\dot{\gamma}) = \eta_0^+(t) \qquad \text{for} \quad \dot{\gamma} = 1/t \tag{2.11}$$

where $\eta_0^+(t)$ is the start-up zero-shear viscosity function until the velocity of the sphere reaches the terminal velocity. Hermann and Sobczak [29] used an inductive detection system in a falling sphere viscometer (Fig. 2.18). In contrast to the laser method, windows are not required. Mattischek and Sobczak [30] developed a high pressure cell for use with this viscometer (Fig. 2.19). The pressure generator consists of two parts: a dynamic seal and a pressurizing screw. Mattischek and Sobczak [31] developed another falling sphere viscometer, which was capable of achieving temperatures of up to 250℃, and has a built-in pressure sensor at the bottom of the sample chamber.

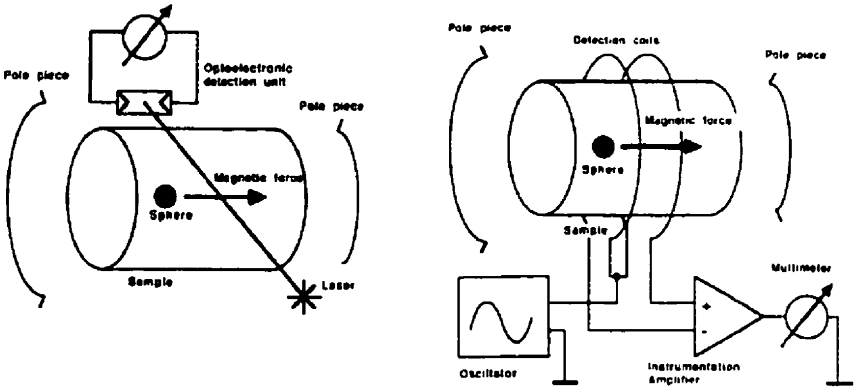

Figure 2.18. Optical and inductive measuring principles [29].

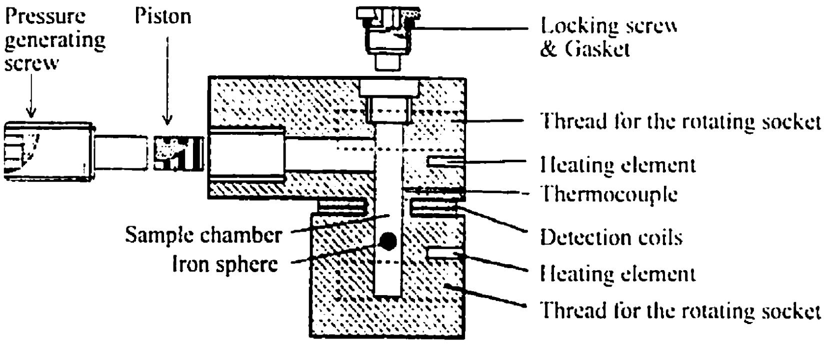

Figure 2.19. High pressure cell of the high-pressure falling sphere viscometer [31].

References

1. E.B. Bagley, *J. Applied Physics* 28:624 (1957).
2. B. Rabinowitch, *Zeitschrift für Physikalische Chemie* 145:1 (1929).
3. C.D. Han, *Rheology in polymer processing*, Academic Press, New York, 1976.
4. J.M. Dealy and K.F. Wissbrun, *Melt Rheology and Its Role in plastics processing*, Chapman and Hall, London, 1995.
5. R.F. Westover, *Polymer Engineering and Science* 83 (1966).
6. V.-H. Karl, *Die Angewandte Makromolekulare Chemie* 79:11 (1979).
7. P.D. Driscoll and D.C. Bogue, *J. Applied Polym. Sci.* 329:1755 (1990).
8. F.S. Baker and M. Thomas, *Makromol. Chem., Macromol. Symp.* 68:13 (1993).
9. M.R. Mackley, R.T.J. Marshall, and J.B.A.F. Smeulders, *J. Rheology* 39:1293 (1995).
10. S. Chakravorty, M. Rides, C.R.G. Allen, and C.S. Brown, *Plast., Rubber Compos. Pcocess. Appl.* 25:260 (1996).
11. D.M. Binding, M.A. Couch, and K. Walters, *J. Non-Newt. Fluid Mech.* 79:137 (1998).
12. K. Walters *Rheometry*, Chapman and Hall, London, 1975.
13. H.M. Laun, *Rhologica Acta* 22:171 (1983).
14. S.E. Kadijk and Van den Brule, *Polym. Engineering and Science* 30:1535 (1994).
15. H.C. Langelaan, A.D. Gotsis, and A.P. de Boer, *J. Rheology* 38:1353 (1994).
16. M. Mooney, *Industrial and Engineering Chemistry* 6:147 (1934).
17. ASTM:D 1646-92, *ASTM Standards*, American National Standards Institute, 1994.
18. V. Semjonow, *Rheologica Acta* 2:138 (1962).
19. D.J. Highgate and R.W. Whorlow, *Rheologica Acta* 8:142 (1969).
20. F.N. Cogswell, *Plastics and Polymers* Feb:39 (1973).
21. S. Bair, W. O. Winer, and F. Qureshi, *Lubrication Science* 5:189 (1993).
22. S. Bair, M. Khonsari, and W.O. Winer, *Tribology International* 31:573 (1998).
23. P.M. Khandare, J.W. Zondlo, P.B. Stansberry, and A.H. Stiller, *Carbon* 38:881 (2000).
24. C. Macosko, *Rheology: principles, measurements, and applications*, VCH, New York, 1994.
25. R.G. Foltz, K.K. Wang, and J.F. Stevenson, *J. Non-Newt. Fluid Mech.* 3:347 (1978).

26. R. Sobczak, *Rheologica Acta* 25:175 (1986).

27. M. Gahleitner and R. Sobczak, *J. Physics E: Scientific Instruments* 21:1074 (1988).

28. W. Gleissle, in *Rheology Vol.2: Fluids*, G. Astarita, and G. Marrucci, and L. Nicolais, editors, 1980.

29. W. Hermann and R. Sobczak, *J. Applied Polymer Science* 37:2675 (1989).

30. J.-P. Mattischek and R. Sobczak, *Meas. Sci. Technol.* 5:782 (1994).

31. J.-P. Mattischek and R. Sobczak, *Rev. Sci. instrum.* 68:2101 (1997).

Chapter 3. The High Pressure Sliding Plate Rheometer

Giacomin and Dealy [1-3] developed a sliding plate rheometer (SPR) incorporating a shear stress transducer, which has significant advantages over the types of rheometer discussed in the previous chapter. The parallel plate geometry and drag flow allow the direct measurement of shear strain, and the shear stress transducer measures stress with no end or edge effects. Giacomin [1] describes the sliding plate rheometer in detail in his doctoral thesis. Koran and Dealy [4] developed a high-pressure version of the sliding plate rheometer to study the effect of pressure on the rheological properties of molten polymers.

3.1. The Sliding Plate Rheometer

Figure 3.1 shows the basic features of a sliding plate rheometer. The rheometer generates a shear deformation by moving one plate relative to the other. The basic rheological quantities, stress and strain, are related to the measured quantities as follows:

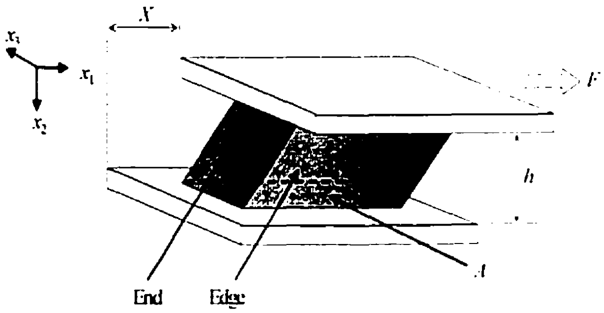

Figure 3.1. Basic elements of sliding plate flow. An edge is a free surface parallel to the moving direction, and an end is normal to the direction.

$$\sigma = F/A \tag{3.1}$$

$$\gamma = X/h \tag{3.2}$$

$$\dot{\gamma}\equiv\frac{\partial v_1}{\partial x_2}=V/h=\frac{d\gamma}{dt} \tag{3.3}$$

where F is the shear force, X is the displacement of the moving plate, V is its velocity, and h is the gap between the two plates.

The sliding plate rheometer has some limitations. The length of the rheometer limits the total strain and shear rate, and edge and end effects induce inhomogeneity in the deformation of elastic materials. These effects arise from a stress mismatch at the free surfaces [5]. Sample degradation is much less severe than in a parallel disk or cone-plate rheometer, since the maximum torque is obtained at the edge in the latter instruments where the sample is exposed to the environment. Secondary flow in the sliding plate rheometer arises from the normal stress differences [6]:

$$N_1\equiv\sigma_{11}-\sigma_{22} \tag{4.4}$$

$$N_2\equiv\sigma_{22}-\sigma_{33} \tag{4.5}$$

Since the shape of the wetted area of a sliding plate rheometer is not precisely controlled, it is difficult to establish this area. It is thus difficult to obtain the true stress by measuring the total force on one of the plates.

To eliminate the surface area problem and edge/end effects, the shear stress transducer (SST) was developed by Dealy [7] and used by Giacomin and Dealy [1-3] in the SPR. Figure 3.2 [8] shows the essential features of the rheometer. The stress is measured in the center of the sample by means of the SST, and the measurement is free from the free-surface phenomena and degradation at the edges of the sample. The area over which the shear force is equal to that of the SST active face, and there is no problem arising from the uncertainty about the total wetted area. Figure 3.3 shows the SST and the beam that deflects in response to a shear force on the active face. This SST is called a "disc spring transducer", because the elastic member is a steel diaphragm [9]. Figure 3.4 shows the basic dimensions of the SST.

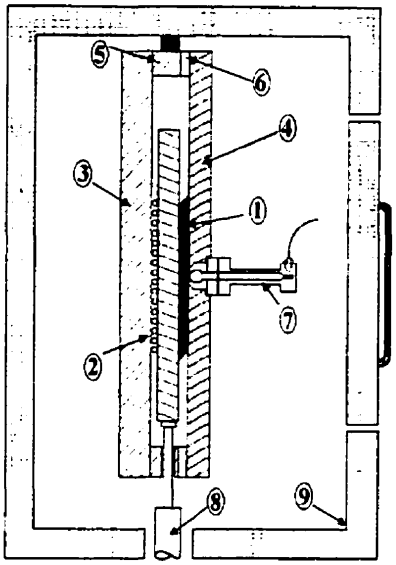

Figure 3.2. Cross section showing the essential elements of the SPR incorporating a disk-spring-type shear stress transducer. 1 sample; 2 moving plate; 3 back support; 4 stationary plate; 5 end frame; 6 gap spacer; 7 shear stress transducer incorporating a rigid beam supported by a steal diaphragm disk spring; 8 linear actuator; and 9 oven [8].

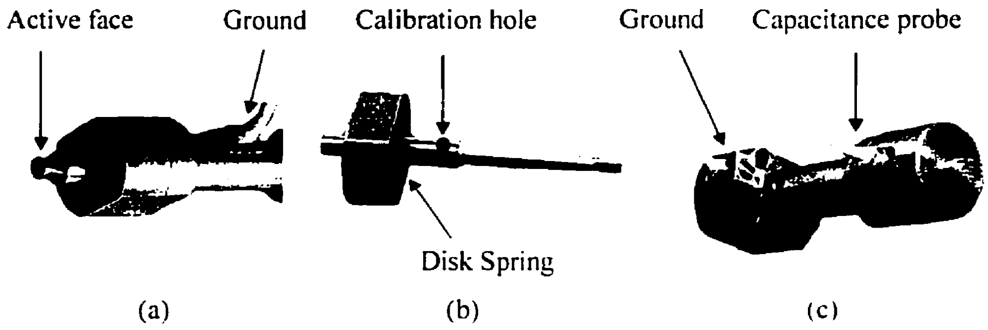

Figure 3.3. SST and beam (a) Left-top view of the SST. (b) Cantilever beam in the SST. (c) Right-top view.

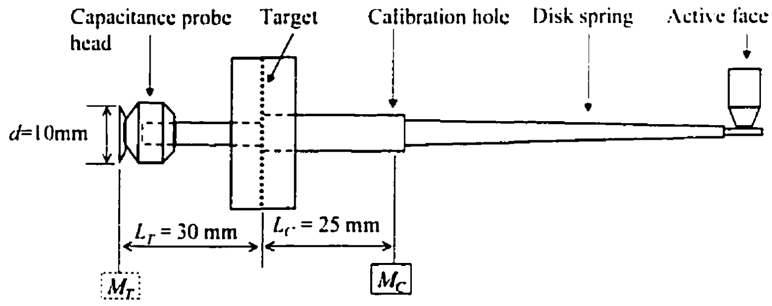

Figure 3.4. Dimensions of the SST of the SPR.

The capacitance proximity probe provides a signal related to the distance between the probe tip and the target. A shear stress causes deflection of the beam and a change in the probe signal. A Capacitec^R signal conditioner and amplifier (Fig. 3.5) provide a signal that is proportional to stress, and an A/D convertor provides a digital output.

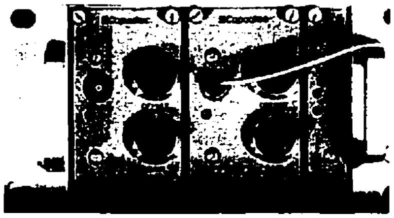

Figure 3.5. Capacitec^R amplifier.

User-defined deformation histories can be generated by means of the servohydraulic linear actuator with computer control. It is possible, for example, to generate the following histories: steady shear, single or multi step strains, start-up and cessation of steady shear, interrupted shear, large amplitude oscillatory shear, exponential shear, and creep and creep recovery. A precision linear bearing table supports the movement of the moving plate. High temperature lubricant is required in the bearing system to keep the movement smooth.

In controlled strain experiments, the command displacement is compared with the actual displacement of the moving plate, and a feedback loop controls the displacement of the moving plate. In controlled stress experiments, a command stress is compared with the stress sensed by the SST, and a feedback loop controls the displacement of the moving plate. This latter type of experiment requires very careful tuning of the controller.

3.2. The High Pressure Sliding Plate Rheometer

The high-pressure sliding plate rheometer (HPSPR) [4,10] developed at McGill University can generate controlled, homogeneous shearing deformations at uniform pressure. This rheometer can be used to determine the effects of pressure, temperature and shear deformations on the rheological behavior of elastomers and molten thermoplastics. Koran [10] describes this rheometer in detail in his doctoral thesis.

3.2.1. Basic Features

The HPSPR has been used to study several materials, and its capabilities and limitations have been explored. Figures 3.6 to 3.8 show the HPSPR system. It operates over a temperature range from 25 to 225℃, and under a vacuum or at pressures up to 70 MPa. It can generate shear rates of 10^{-5} to 500 s^{-1} and can measure shear stresses over a range from 0.146 to 300 kPa. The HPSPR is similar in basic design to the earlier ambient-pressure SPR, but its design required a special housing and SST due to the high-pressures involved. A vessel able to withstand an operating pressure of 70 MPa at a temperature of 225℃ encases the two parallel plates and most parts of the shear stress transducer. One part of the vessel consists of the cover plate, which swings open for sample loading. It is fixed to the main body of the pressure vessel by sixteen 7/8-in bolts, which are tightened by an air-powered torque wrench. Openings at the top and bottom of the rheometer allow actuation rods to translate, so that the volume inside the vessel remains constant.

The rheometer is pressurized by a hand pump made by Enerpac. The pressurizing medium is Krytox General Purpose Oil 107 made by Dupont. This oil is thermally stable, nonflammable, non-volatile, a good lubricant and does not swell either polar or nonpolar materials. Koran [4] found that there was no rheological effect of this oil on Dowlex™ 2049 linear low density polyethylene. After filling the HPSPR with Krytox oil, the approximate desired pressure is obtained by means of the hand pump. The pressure is then adjusted precisely by the piston pump. A Dynisco pressure transducer is used to determine the pressure in the HPSPR. The transducer is calibrated by means of a dead weight tester. The most convenient method of sample preparation is by compression molding, which produces a rectangular sheet. Using this method the sample can be prepared quickly in order to minimize strain and thermal history. Detailed experimental procedures are described in the Appendix.

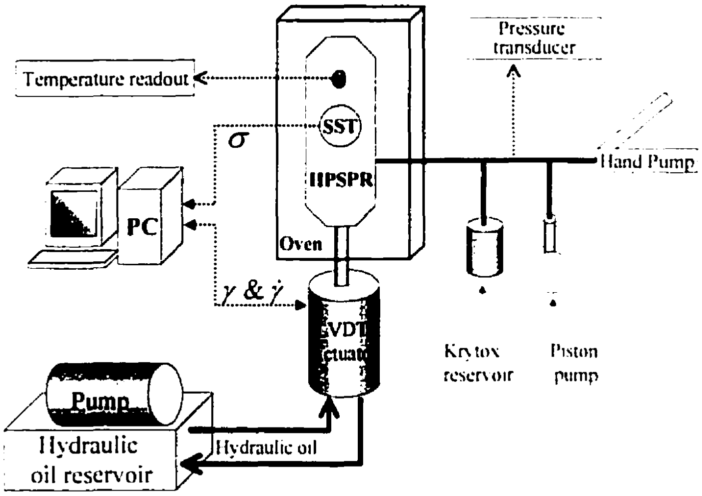

Figure 3.6. Overall system of the HPSPR.

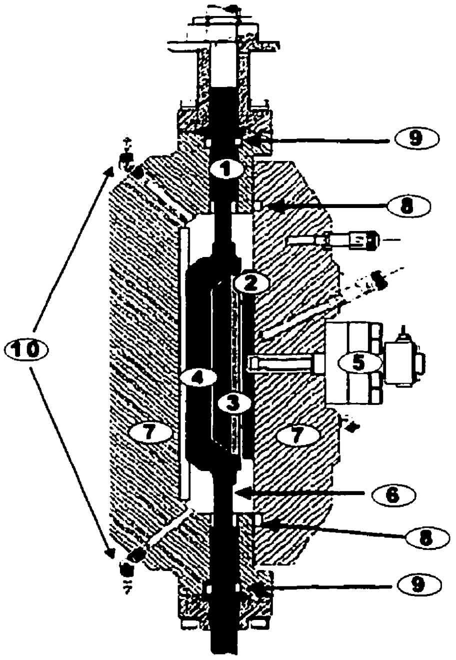

Figure 3.7. The side view of HPSPR:
1 Actuating Rod; 2 Fixed Plate; 3 Moving Plate; 4 Carriage; 5 SST; 6 Pressurizing Oil; 7 Pressure Vessel; 8 O-ring; 9 Cup seal; and 10. Filling ports [10].

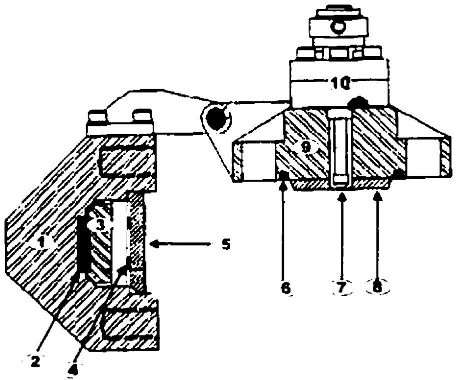

Figure 3.8. Top view of the HPSPR: 1 main body of pressure vessel; 2 bearing plate; 3 moving plate carriage; 4 spacers; 5 moving plate; 6 O-ring; 7 SST active face head; 8 fixed plate; 9 cover plate of pressure vessel; and 10 SST [10].

3.2.2. Shear Stress Transducer

Figures 3.9 and 3.10 show the details and method of installation of the SST.

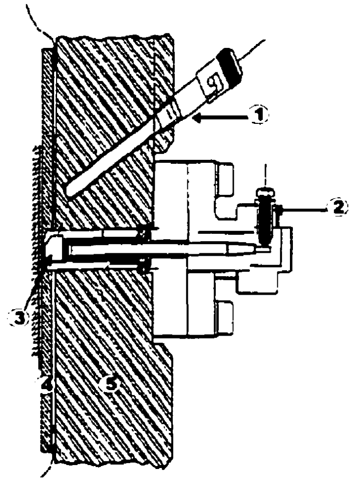

Figure 3.9. Schematic of SST in the HPSPR: 1 thermocouple; 2 Capacitance probe; 3 SST active face head; 4 fixed plate; and 5 Cover plate of pressure vessel [10].

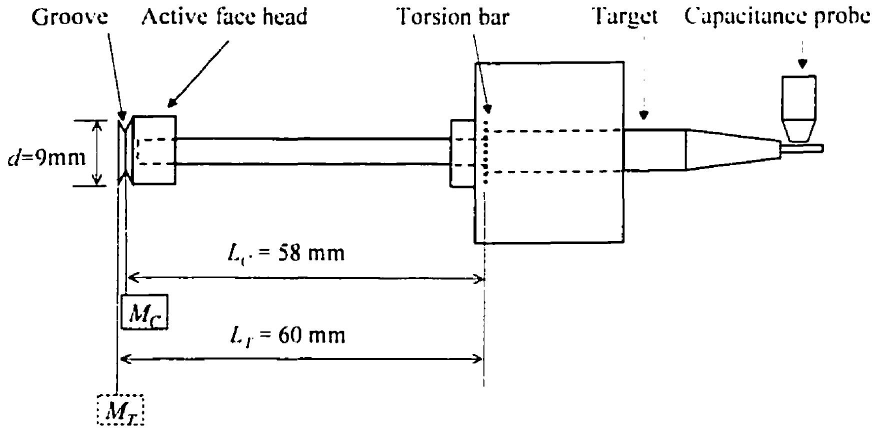

Figure 3.10. Dimensions of SST of HPSPR.

3.2.2.1. Calibration of SST

Calibration is performed by suspending masses from the SST active face head (Fig. 3.11). The linearity of the calibration is confirmed by use of a series of masses (Fig. 3.12). This calibration can be performed at any temperature but only at atmospheric pressure, since the cover plate of the pressure vessel must be open for calibration.

Because a mass cannot be suspended from the surface of the active face, it is hung instead from a groove in the head by a length of wire. This groove is located 2.5 mm from the active face (Fig. 3.10). The stress corresponding to a given mass is given by:

$$\sigma \equiv \frac{F}{A} = \frac{\left(M_C \dfrac{L_C}{L_T} g\right)}{\pi (d/2)^2} \tag{3.6}$$

where M_C is the mass suspended from the groove.

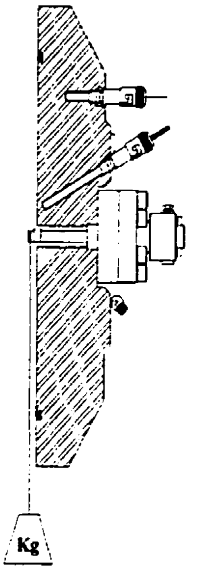

Figure 3.11. Suspended mass calibration at atmospheric pressure [10].

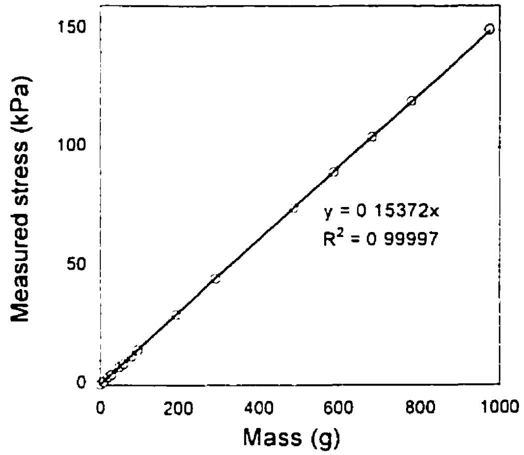

Figure 3.12. Confirmation of the linearity of the calibration line.

3.2.2.2. Temperature dependence of SST

Figure 3.13 shows the temperature dependence of the SST response. The calibration was performed at 170℃, and the responses at three other temperatures were also obtained. The nominal shear stress was calculated using Equation 3.6. Eight masses were used at each temperature. The linearity is quite good. The slope of the lines varies little, but the offset (intercept), which is the SST response for the zero-mass, varies dramatically. Figure 3.14 shows the change of the slope with temperature, and Fig. 3.15 shows the change of the offset. The relations between T and the slope and the offset are given by:

$$S(T) = -1.894 \times 10^{-5} T^2 + 7.635 \times 10^{-3} T + 0.249 \tag{3.7}$$

$$O(T) = 0.0515 T^2 - 19.826 T - 1881.040 \tag{3.8}$$

where T is in ℃, S is the slope of the calibration line, and O is the offset in kPa. The change of the offset can be eliminated by zeroing the SST at the operating temperature in the software before starting a run. To account for the change of slope, separate calibration at each temperature is required. However, temperature variation during a run can still cause a variation in the measured stress. After the SST is calibrated at T, its response at another temperature is given by Equations 3.7 and 3.8:

$$\sigma = S(T)\sigma_n + O(T) \tag{3.9}$$

where σ_n is the nominal stress. The normal temperature fluctuation during a run at 170℃ is ±0.03℃, and the calibration line at 170.03℃ is:

$$\sigma = 1.000036\sigma_n + 0.0067 \tag{3.10}$$

and the response of the SST for a stress of 100 kPa at 170.03℃ is 100.07 kPa. Since the minimum measured stress is 0.146 kPa, the variation of measured stress due to a temperature change of 0.03℃ is negligible. The SST response at 171℃ for 100 kPa is 102.37 kPa, but the response change due to a slope change is 0.117 kPa, which is negligible, while 2.25 kPa is due to the offset change. As long as the SST is zeroed at the beginning of each run, a temperature variation of 1℃ has very little effect on the SST response. However, Fig. 3.14 shows there is about 1% difference in slope between 170 and 180℃, and re-calibration is thus required for experiments at an operating temperature much higher than the calibration temperature.

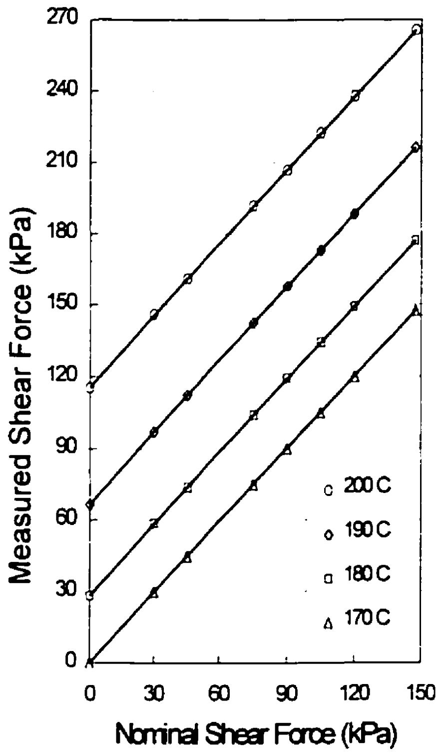

Figure 3.13. Temperature dependence of SST response. Calibration was carried out at 170℃, and the response of SST with temperature and mass was recorded.

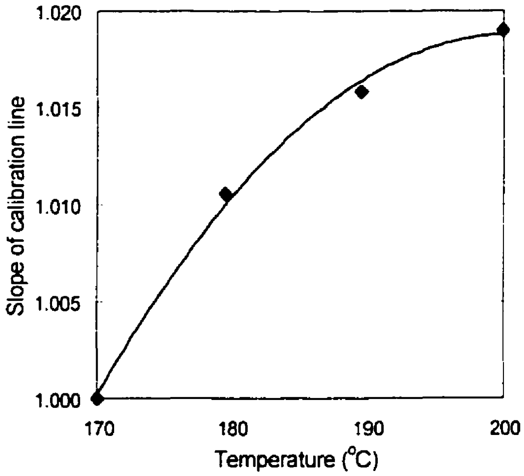

Figure 3.14. Temperature dependence of slope of SST response.

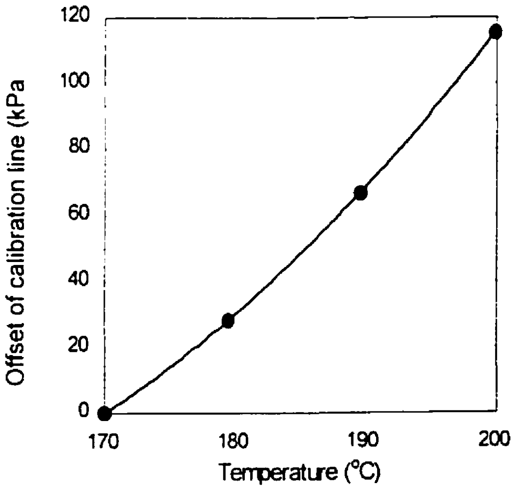

Figure 3.15. Temperature dependence of offset of SST response.

3.2.2.3. Pressure dependence of SST response

The response of the SST also depends on pressure. The pressure was increased from atmospheric to 70 MPa, and the resulting offset values are shown in Fig. 3.16. As in the case of the temperature dependence, the variation in the offset can be compensated by zeroing the SST at each pressure.

The dependence of the slope on pressure was determined by use of a spring. One end of the spring is fixed to the SST active face head, and the other to the moving plate carriage (Fig. 3.17). The actuator pulls down the carriage to produce the desired displacement of the spring. The resulting force applied to the SST is give by Hooke's law:

$$F = -kX \tag{3.11}$$

where k is the spring constant, and X is the displacement of the spring. Forces corresponding to eighteen displacements are imposed, and the stress signals are

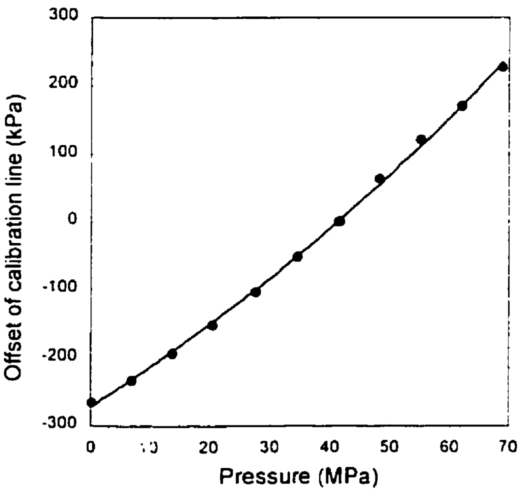

Figure 3.16. Pressure dependence of the offset of SST response.

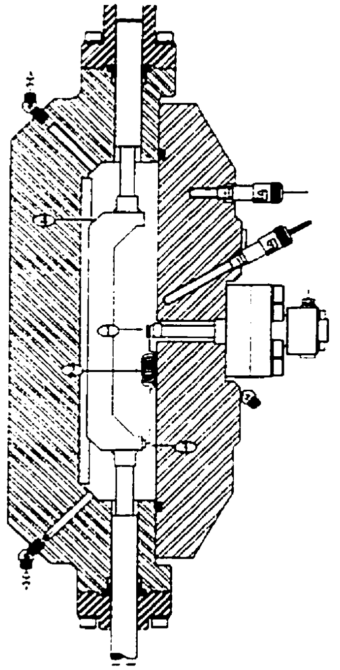

Figure 3.17.
Spring calibration method. 1 SST head; 2 Spring; 3 connection; and 4 Carriage [10].

recorded. Calibration is first carried out at atmospheric pressure. Another test was performed at 69 MPa, keeping the calibration at atmospheric pressure, but the signal was zeroed at 69 MPa. The variation of the offset with pressure in the range from 0.1 to 70 MPa is around 500 kPa, which is well above the normal measurement range, ±300 kPa. Figure 3.18 shows that there is a 1.3% variation between the slopes at 1 atm and 69 MPa, which is negligible. The calibration constant for atmospheric pressure can thus be used at all pressures.

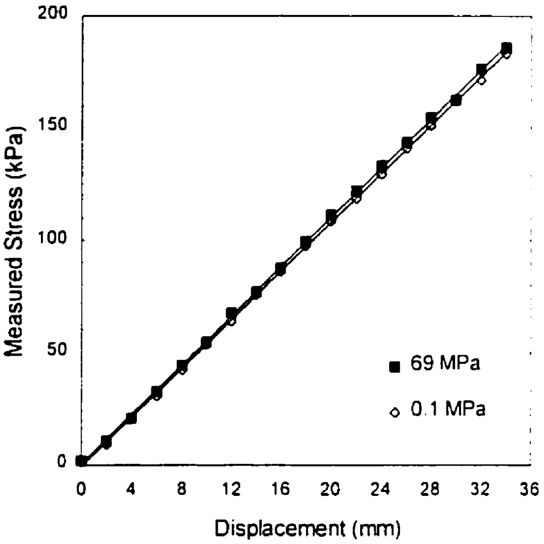

Figure 3.18. Pressure dependence of the slope of the calibration lines.

3.2.3. Sealing

Both dynamic and static seals are required. Cup-seals prevent oil leaks around the actuating rods during their linear motion, and an O ring prevents oil leaks through the gap between the two plates of the pressure vessel.

3.2.3.1. Cup-seals

A cup-seal consists of two parts: a graphite-filled Teflon^{TM} cup and a metal spring. According to the specifications, the cup-seals used are supposed to withstand a pressure of 70 MPa at 250℃, but Koran [10] found that pressurization needed to start at a temperature below 180℃ to avoid leakage past the cup-seals above the following critical pressures: 20.6 MPa at 180℃ to 2.06 MPa at 200℃. McGlashan [11] used modified cup-seals to eliminate this problem, as shown in Fig. 3.19. However, two new problems arose. An oil leak around the top actuating rod seal was observed at shear rates above 100 s^{-1} at 70 MPa and 170℃, and a new cup left dark material when it was rubbed on white paper, indicating that it may have been eroded.

Figure 3.20 shows the way cup-seals work. When there is no pressure, there is a small gap between the cup-seal and the actuating rod. Pressure, which is applied by means of the pressurizing oil, pushes the cup wall outward, closing the gap and sealing the rod.

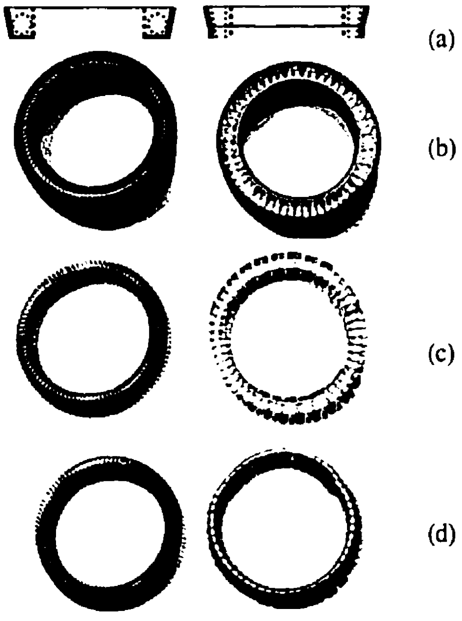

Figure 3.19. Left: old cup-seals and right: new cup-seals. (a) Side view (b) Top-view (c) Top-view of springs (d) Bottom-view of springs.

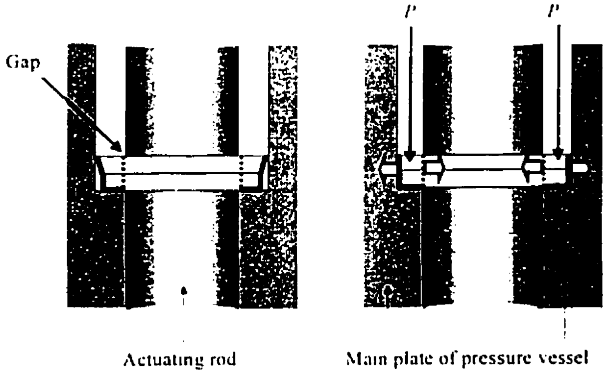

Figure 3.20. Sealing mechanism of a cup-seal around the actuating rod at the bottom.

3.2.4. O-ring

There is a groove on the inner surface of the cover plate of the pressure vessel to take the Viton^{TM} O-ring that prevents oil leakage through the gap between the main body and cover plate of the pressure vessel. However, if the sixteen, 7/8-inch bolts are not tightened sufficiently, the O-ring will be damaged as shown in Fig. 3.21, even if the pressure holds. The torque on the tightening bolts is controlled by adjusting the air pressure on the Qix Modular FRL combination regulator (Fig. 3.22). Table 3.1 shows the values used at various test pressures.

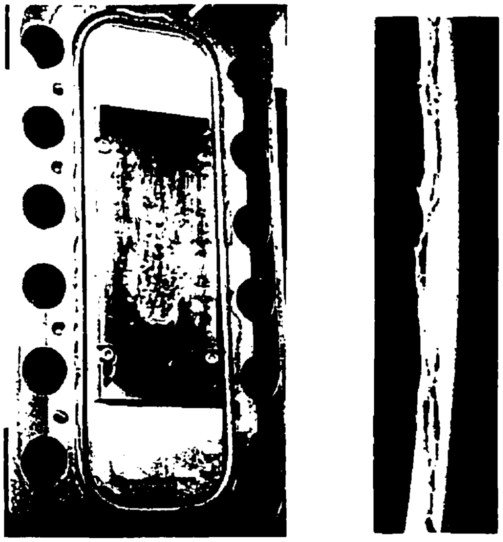

(a) (b)

Figure 3.21. Defective O-ring due to weak tightening. (a) the defective O-ring on the cover plate (b) enlarged defective part.

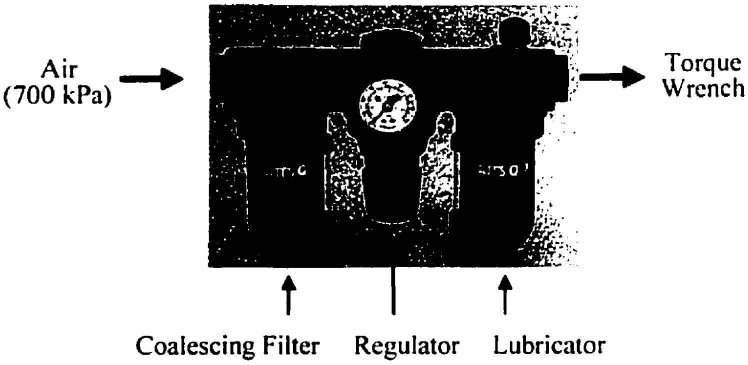

Figure 3.22. Regulator combination.

Table 3.1. Torques for bolt-tightening.

Test Pressure (MPa)	Required torque for the wrench (Nm)	Air Pressure of the regulator	
		(psi)	(kPa)
~ 35	310	33	230
~ 52	465	52	360
~ 69	615	69	480

3.2.5. Pressurizing System

The pressure inside the HPSPR is increased by a hand pump after filling the rheometer with Krytox oil, which is stored in a reservoir (Fig. 3.23). Fine tuning of the pressure level is carried out by a piston pump, and the resulting pressure is measured by the Dynisco pressure transducer.

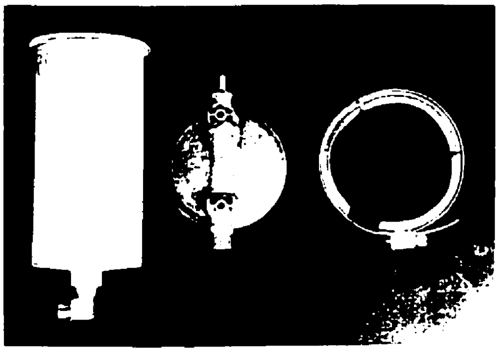

Figure 3.23. Disassembled Krytox reservoir.

3.2.5.1. Pressure transducer

A Dynisco pressure transducer Model 830 (Fig. 3.24) was used to measure the pressure inside the HPSPR. The operating range of this transducer is -54 to 120℃ and 0 to 70 MPa. The specified effect of temperature on span is ±0.036% full scale per ℃, and the nominal accuracy is ±0.5%. A Dynisco Model 1290 Strain Gauge Input Indicator is used to display the pressure value. The indicator was calibrated at the factory, but the calibration was verified by use of a dead weight tester (Fig. 3.25). The calibration line (Fig. 3.26) was obtained by recording the indicated pressure values for the weights on the tester, and it exhibited good linearity but a -1.15% deviation from the applied pressure. Table 3.2 shows the indicated pressure values for various applied pressures.

Figure 3.24. Pressure transducer.

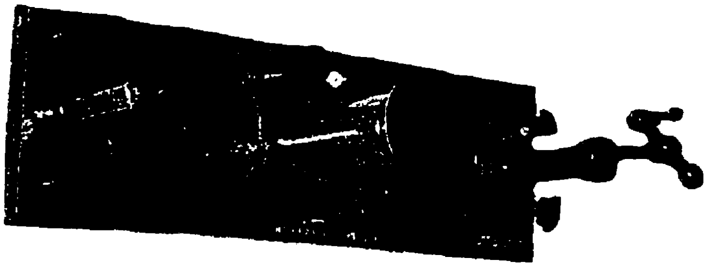

Figure 3.25. Dead weight tester.

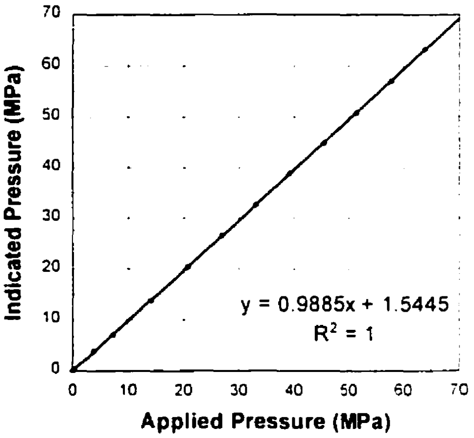

Figure 3.26. Calibration line of the pressure transducer.

Table 3.2. Indicated pressures at various applied pressures.

Applied Pressure		Indicated Pressure
(MPa)	(psia)	(psig)
0.1	15	0
23.0	3330	3280
45.9	6660	6570
68.9	10000	9870

3.2.5.2. Hand pump

The pump used to pressurize the HPSPR was an Enerpac P-2282 hand pump (Fig. 3.27), which can generate pressures up 275 MPa. The hand pump provides two-speed operation for faster filling. It takes about 30 minutes to increase the pressure to 70 MPa. Table 3.3 shows the specifications of the hand pump. When the high pressure is released, the release valve must be opened a little. If the valve is turned by more than 30° at 70 MPa, the sealing system of the pump will be damaged. It is recommended that the valve be opened by 5° and increased gradually with decreasing pressure.

Table 3.3. Basic features of the Enerpac hand pump P-2282.

Oil Capacity (ℓ)	Pressure Rating (MPa)		Oil Displacement per Stroke (㎖)		Piston Stroke (cm)
	1st Stage	2nd Stage	1st Stage	2nd Stage	
1	1.4	275	16	0.6	2.54

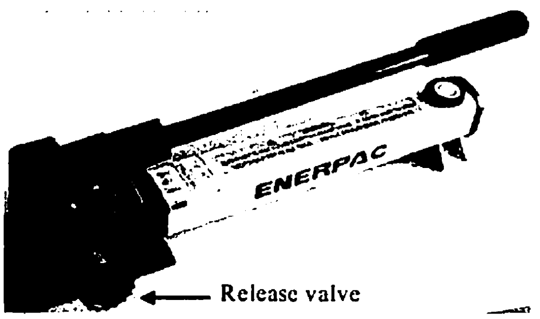

Figure 3.27. Enerpac hand pump P-2282.

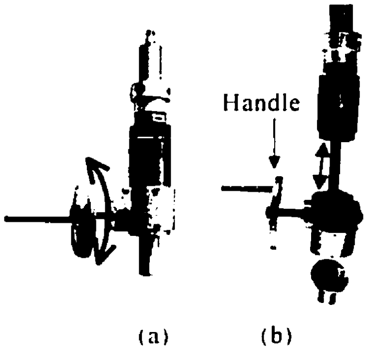

Figure 3.28. Worm-drive piston pump. (a) whole pump (b) disassembled pump.

3.2.5.3. Piston pump

Since one stroke of the hand pump increases the pressure by 2 to 7 MPa, an additional system was required to set the desired pressure. A worm-drive piston pump (Fig. 3.28) makes it possible to increase the pressure by 0.02 MPa for each revolution of the pump handle. Revolving the handle causes a linear displacement of the piston in the piston pump housing.

References

1. A.J. Giacomin, Ph.D. Thesis, McGill University, Montreal, Canada, 1987.
2. A.J. Giacomin and J.M. Dealy, *SPE ANTEC*, 32:771 (1986).
3. A.J. Giacomin, T. Samurkas, and J.M. Dealy, *Polym. Eng. Sci.* 29:499 (1989).
4. F. Koran and J.M. Dealy, *J. Rheology* 43:1279 (1999).
5. J.M. Dealy and A.J. Giacomin, "Sliding Plate and Sliding Cylinder Rheometers", Chapter 8 of *Rhelogical Measurement* 2nd Ed. edited by A.A. Collyer and D.W. Clegg, Chapman & Hall, London, 1998.
6. J.M. Dealy, *Rheometers for molten plastics*, Van Nostrand Reinhold, New York, 1982.
7. J.M. Dealy, U.S. Patent No. 04464928 (1984).
8. J.M. Dealy and R.S. Jeyaseelan, *J. Rheology* 42:833 (1998).
9. J.M. Dealy, K.R. Bubic, and S.R. Doshi, US Patent No. 5,094,100 (1992).
10. F. Koran, Ph.D. Thesis, McGill University, Montreal, Canada, 1998.
11. S. McGlashan, Personal communication 1999.

Chapter 4. Materials Studied

Polyethylene (PE) has the simplest basic structure of any polymer and is widely used due to its low cost, chemical resistance, good processibility, toughness, and flexibility. Three polyethylenes, with similar molecular weights but varying molecular structures, were chosen for this work. The rheological properties of these PEs are well known, since they have been studied by Koran [1], Heuzey [2], Hatzikiriakos *et al.* [3] Hatzikiriakos and Rosenbaum [4], Wood Adams [5], and Kim [6].

4.1. Linear Low Density Polyethylene and Metallocene Polyethylenes

Dowlex 2049AC is a commercial, linear, low-density polyethylene (LLDPE) manufactured by Dow Chemical Company. It is manufactured by a solution process with octene comonomer and has a polydispersity of 3.8. It has been previously characterized at McGill and has good stability over a long period.

Metallocene polyethylene is a new polymer class that is distinguished from traditional PEs, including LLDPE, low density polyethylene (LDPE), and high density polyethylene (HDPE). Metallocene polyethylene, or mPE, is produced using metallocene catalysts that have a single active site, while Ziegler-Natta catalysts, which are used to produce traditional linear polymers, have multiple active sites. Metalocene PEs are interesting not only as commercial polymers due to their processability and good physical properties, but also as experimental materials because of their well controlled structure. They have higher toughness, better optical properties and better heat-sealing characteristics than traditional PEs. There are two subclasses of mPE: linear mPE (LmPE), which has short chain branching (SCB) or no branching, and branched mPE (BmPE), which has low levels of LCB. Exact

3025, which is made by Exxon, is a LmPE with a polydispersity of 2.3, butene comonomer, and no LCB. One BmPE made by Dow Chemical Company was also used. It has a low level of LCB and a polydispersity of 2.32.

In Fig. 4.1 the molecular structures of the materials studied are sketched. Broad SCB distributions are present in the LLDPE. By comparison, the mPEs exhibit narrow and well controlled SCB and molecular weight distributions.

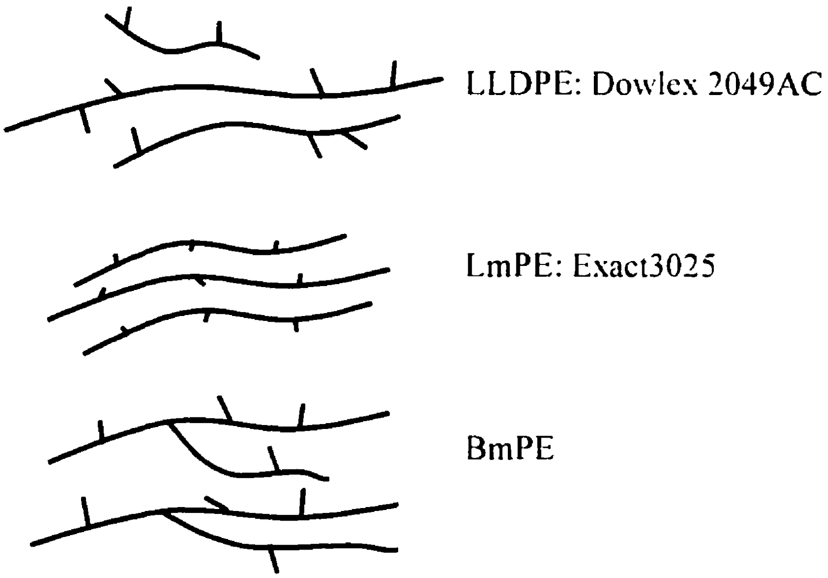

Figure 4.1. Schematic of molecular structures of the polyethylenes studied.

4.2. Physical Properties of the PEs

To determine the effect of polydispersity on the pressure sensitivity of the rheological properties, the results for the LLDPE and the LmPE, which have a similar M_w and no LCB but different polydispersities, were compared. To determine the effect of LCB, the results of the LmPE and the BmPE, which have a similar M_w and polydispersity but different levels of LCB, were used. Table 4.1 lists some physical and rheological properties of the polymers studied.

The zero-shear viscosity, η_0, was determined from creep compliance experiments at 170℃ and atmospheric pressure using an SR5000 controlled stress rheometer made by Rheometric Scientific. This instrument was operated in the parallel plate configuration (255 mm diameter) with a gap of 1 mm. The stress value was 10 Pa, which was thought to be the limiting stress for linear behavior [7]. The melting temperatures were determined by Kim [6] using a differential scanning calorimeter (DSC) with a heating rate of 10℃/min. Two melting temperatures were identified, one ($T_{m,h}$) from the minimum in the endothermic curve, and the other $T_{m,e}$ from the end of the peak (Fig. 4.2). The density, molecular weight, and the polydispersity were provided by Kim [6].

Table 4.1. Physical properties of the materials studied, 1 atm.

Resin	Comonomer	η_0(170℃) (kPa.s)	T_m (℃) [6]		Density (g/㎤) [6]	M_w (g/㏖) [6]	M_w/M_n [6]	LCB/10^3C [8]	
			$T_{m,h}$	$T_{m,e}$				Rheol.	GPC
LLDPE	Octene	13.0	126	138-140	0.923	119,600	3.8	0	0
LmPE	Butene	8.1	105	112-117	0.910	108,800	2.3	0	0
BmPE	Octene	46.1	104	113	0.908	89,100	2.32	0.053	0.06

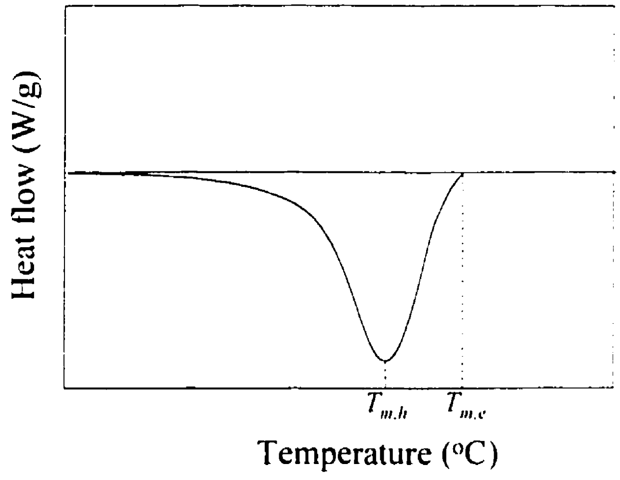

Figure 4.2. Schematic endothermic DSC curve.

Wood-Adams and Dealy [8,9] developed a technique to determine the level of LCB. It is based on rheological and GPC data [10] . The result is the number of

LCB per 1,000 carbons in the back-bone. Carbon-13 NMR could not be used to determine the LCB level of the BmPE, since it cannot distinguish SCB with 6 carbon branches, which arise from the use of octene comonomer, and much longer branches.

4.2.1. Effect of Pressure on T_m and T_g

Since the melting point, T_m, and the glass transition temperature, T_g, increase with pressure, to prevent pressure induced crystallization, the high-pressure measurements must be carried out at temperatures above the elevated T_m and the elevated T_g. The pressure dependencies of T_g and T_m are thus required to establish the minimum operating temperature.

Heuzey [2] obtained pressure-volume-temperature (PVT) data for the LLDPE using a PVT-Gnomix apparatus. The measurements were carried out at constant pressures of 10, 60, an 120 MPa over a temperature range from 220 to 70℃ at a scanning rate of -3℃/min. She proposed the following expression to describe the effect of pressure on the crystallization temperature (T_c):

$$\Delta T_c = 0.281P \tag{4.1}$$

where P is in MPa, and T_c is in ℃. A pressure increase of 70 MPa, which is the maximum operating pressure of the HPSPR, results in a 20℃ increase in T_c. Since the $T_{m,e}$ of LLDPE is around 140℃, the operating temperature must be above 160℃. The value of 170℃ was chosen as the operating temperature for this study.

Nielsen [11] proposed that the T_g of PE is -120℃. Shen and Eisenberg [12] reviewed glass transitions in polymers and showed that values of $\partial T_g / \partial P$ are in the range of 0.1 to 0.3℃/MPa. A pressure increase of 70 MPa will thus cause an increase of T_g in the range of 7 to 21℃, but even after such an increase, the operating temperature of 170℃ is well above the increased T_g.

4.3. Small Amplitude Oscillatory Shear

Small amplitude oscillatory shear (SAOS) experiments are usually used to determine the linear viscoelastic (LVE) properties of molten polymers. In this test, a sinusoidal strain is imposed on a sample:

$$\gamma(t) = \gamma_0 \sin(\omega t) \tag{4.2}$$

where γ_0 is the strain amplitude, and ω is the frequency. If γ_0 is sufficiently small, the resulting stress is also sinusoidal with a phase angle δ:

$$\sigma(t) = \sigma_0 \sin(\omega t + \delta) \tag{4.3}$$

where δ is the loss angle in radians. The absolute value of the complex viscosity is:

$$|\eta^*(\omega)| = \sqrt{(\eta')^2 + (\eta'')^2} \tag{4.4}$$

and can be obtained from the storage (G') and loss (G'') moduli:

$$\eta' = G''/\omega = G_d \cos(\delta)/\omega \tag{4.5}$$

$$\eta'' = G'/\omega = G_d \sin(\delta)/\omega \tag{4.6}$$

G_d is called the amplitude ratio. In this thesis "complex viscosity" is used to mean the absolute value of the complex viscosity. Figure 4.3 shows $|\eta^*|$ versus ω at 170℃ for the three PEs [6]. The LmPE data approach a plateau at low frequency, while the BmPE does not have such a region within the accessible frequency range. Moreover, it is obvious that it has a much higher η_0 than the LmPE. LCB narrows the plateau region and increases η_0. The LLDPE curve shows that polydispersity has an effect similar to that of LCB.

Cox and Merz [13] noted that there is a close relationship between the complex viscosity and that measured in steady shear for linear flexible polymers:

$$|\eta^*(\omega)| \cong \eta(\dot{\gamma}) \quad \text{where} \quad \omega = \dot{\gamma} \tag{4.7}$$

This is called the Cox-Merz rule, and the validity of the rule will be discussed in the next chapter.

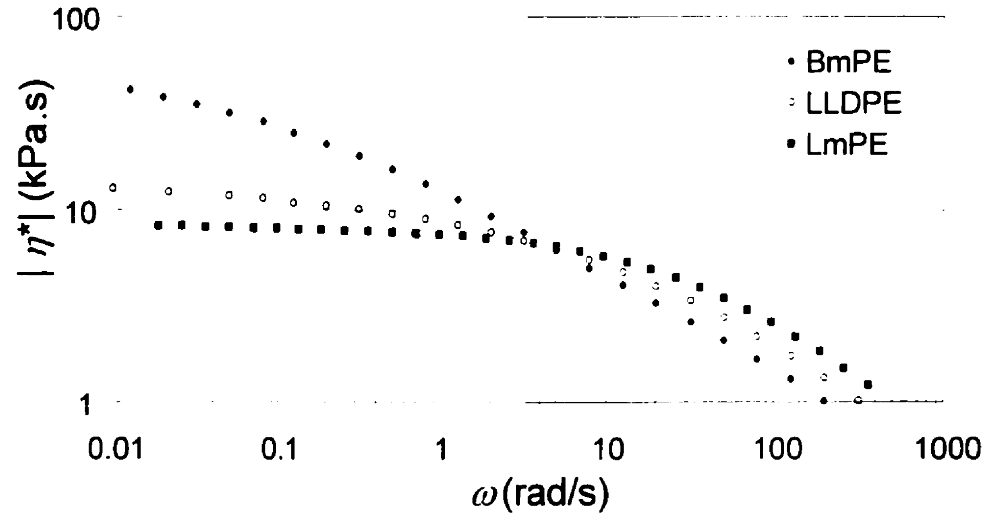

Figure 4.3. Complex viscosity with frequency for the PEs at 170℃, in parallel plate (25 mm diameter) configuration with a gap of 1 mm [6].

4.4. Degradation

A polymer exposed to oxygen and/or heat over a period of time will be degraded either by chain scission or cross-linking. Since degradation affects rheological properties, the experimental time must be kept within a strict limit. The mechanisms of degradation have been thoroughly studied [14].

At relatively low temperatures or at the beginning of degradation, PE undergoes branching, which causes an increase in the viscosity, while polypropylene (PP) undergoes chain scission, which results in a decrease in the viscosity. By measuring the change of viscosity with time, the degree of degradation can be inferred.

To confirm the effect of the degradation on the complex viscosity, time sweep SAOS experiments were carried out at 170℃ with $\gamma_0 = 0.2$ and $\omega = 0.1$ rad/s for four hours for the LLDPE and the LmPE and for five hours for the BmPE. The latter requires more experimental time than the linear samples, since a branched PE has a longer relaxation time than linear PEs having the same back bone length. All tests were carried out in a nitrogen environment to protect the sample from external O_2. Figures 4.4 to 4.6 show the complex viscosity variation with time for the three PEs. The overall trend line was obtained by the least squares method, and the increase in the complex viscosity for each PE was found to be below 1%, which was considered acceptable.

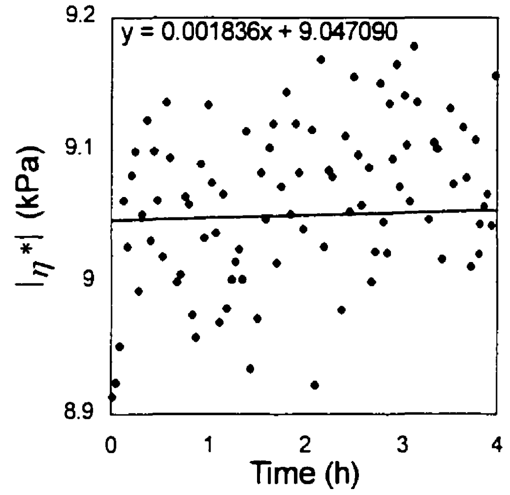

Figure 4.4. Time sweep SAOS for the LmPE at 170℃.

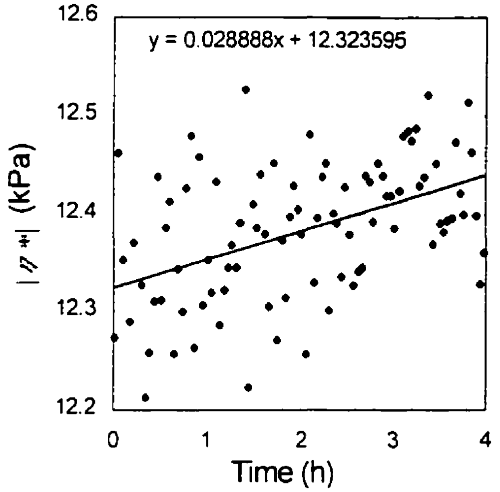

Figure 4.5. Time sweep SAOS for the LLDPE at 170℃.

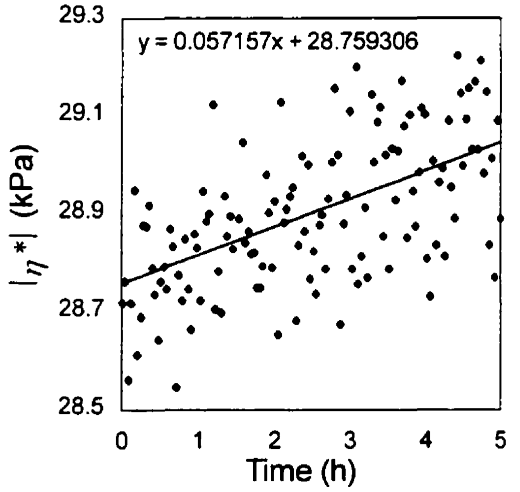

Figure 4.6. Time sweep SAOS for the BmPE at 170℃.

References

1. F. Koran, M.Eng. Thesis, McGill University, Montreal, Canada, 1994.
2. M.-C. Heuzey, M.Eng. Thesis, McGill University, Montreal, Canada, 1996.
3. S.G. Hatzikiriakos, W.H. Hong, and C.W. Stewart, *J. Appl. Polym. Sci.* 55:595 (1995).
4. S.G. Hatzikiriakos and E.E. Rosenbaum, *AIChE. J.* 43:598 (1997).
5. P.M. Wood-Adams, Ph.D. Thesis, McGill University, Montreal, Canada, 1998.
6. S. Kim, Ph.D. Thesis, McGill University, Montreal, Canada, 2000.
7. Y. Ye, M.Eng. Thesis, McGill University, Montreal, Canada, 2001.
8. P.M. Wood-Adams, M.Eng. Thesis, McGill University, Montreal, Canada, 1995.
9. P.M. Wood-Adams and J.M. Dealy, *J. Rheology*, 40:761 (1996).
10. P.M. Wood-Adams and J.M. Dealy, *Macromolecules* 33:7481 (2000).
11. L. Nielsen, *Mechanical Properties of Polymers*, Van Nostrand Reinhold, New York, 1965.
12. M.C. Shen and A. Eisenberg, *Rubber Chemistry and Technology*, 43:95 and 43:155 (1970).
13. W.P. Cox and E.H. Merz, *J. Polym. Sci.* 28:619 (1958).
14. C.H. Bamford and C.F.H. Tipper, *Degradation of Polymers*, Elsevier, New York, 1975.

Chapter 5. Results and Discussion

5.1. Controlled Strain Experiments

5.1.1. Verification of HPSPR Data

The performance of the HPSPR was evaluated by comparing it with the SPR. However, the verification was problematic of the gap between the plates in the HPSPR at high temperature, since this gap is only created when the pressure vessel is closed, and a gauge is thus not useful. Lead or another plastic material is commonly used to determine the gap in such a situation. A small piece of the material somewhat thicker than the gap is placed on one plate, and the vessel is closed squeezing the material between the plates. The vessel is then opened and the thickness of the material is measured and taken to be the gap. However, this method is useful only at room temperature, since the material is squeezed at high temperature but has cooled down when it is removed and measured. The gap indicated by this method was 1 mm, which was the nominal value. However, a comparison of viscosities measured on the HPSPR and the SPR indicated a systematic bias.

The viscosity curves, calculated using the nominal gap, were obtained at 170℃ and atmospheric pressure in both the SPR and the HPSPR. Seven tests were performed, and the maximum relative standard deviation was 4% for each sample in a given instrument. Figure 5.1 shows the difference between the two instruments. It was concluded that the nominal gap of 1 mm was not the true gap in the HPSPR. Based on comparison of data from the SPR with those from other rheometers, it had been established that data from the SPR are quite reliable. Further it was found that if a value of 0.95 mm was taken to be the true gap in the HPSPR at the operating temperature, data from the HPSPR were found to be in excellent agreement with these from the SPR. Therefore a true gap value of 0.95 mm was assumed in this work.

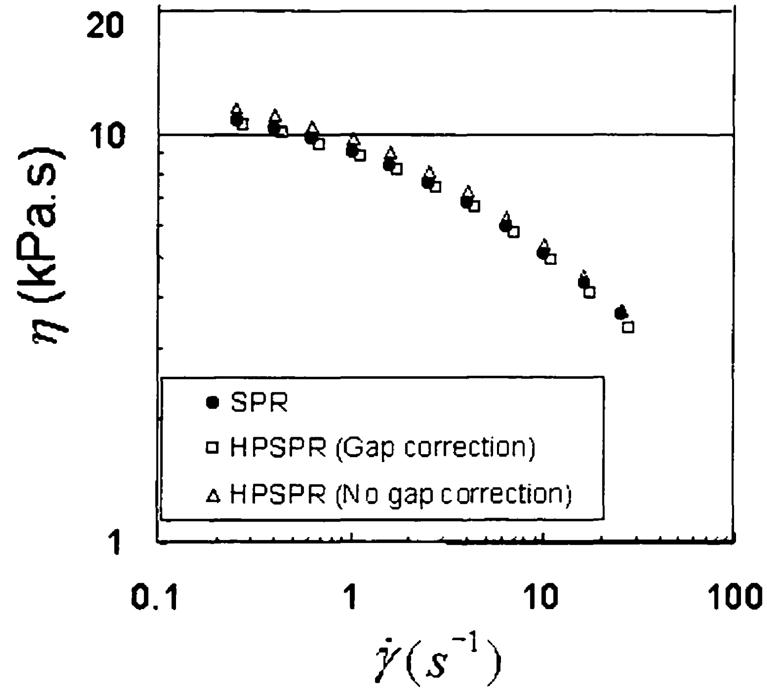

Figure 5.1. Gap correction and comparison with SPR for LLDPE at 170℃.

5.1.2. Test of the Cox-Merz Rule

As shown in Figures 5.2 to 5.4 the values of the viscosity and the complex viscosity do not agree perfectly, although the shapes of the two curves are quite similar. The viscosity curves are flatter at low shear rates and more sloped at high shear rates relative to the complex viscosity curves. The LLDPE and the BmPE exhibit crossing points due to the difference in curvature, while the LmPE has no crossing point within the range of the measurements. However, based on the trend in the LmPE curve, a crossover at a shear rate of about 50 s^{-1} is expected. The maximum deviation of the complex viscosity is greater than the standard deviation of the HPSPR data, but several data points of the complex viscosity are very close to the viscosity curve. It is thus difficult to decide whether the Cox-Merz rule is valid.

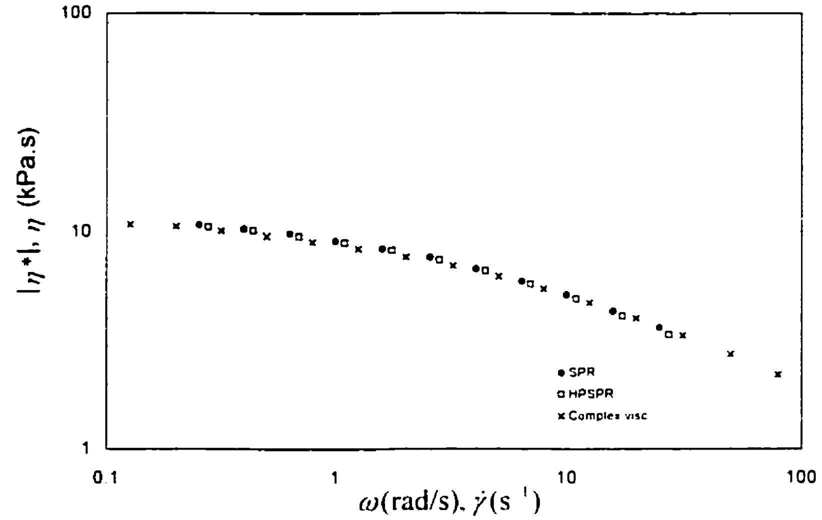

Figure 5.2. Viscosity curves of LLDPE at 170℃.

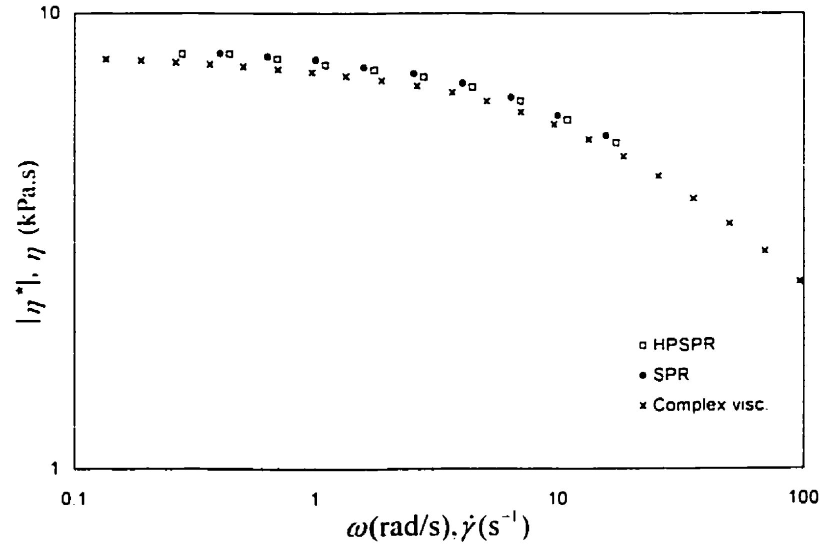

Figure 5.3. Viscosity curves of LmPE at 170℃.

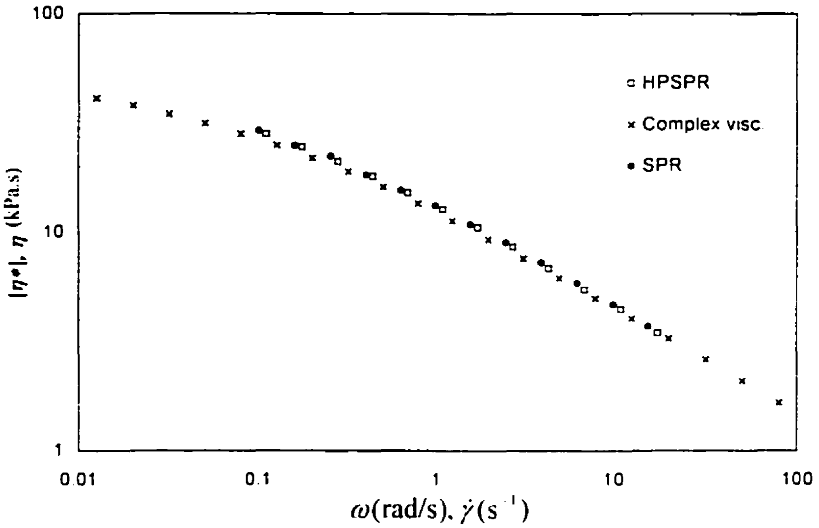

Figure 5.4. Viscosity curves of the BmPE at 170℃.

Kim [1] compared the complex viscosity curves of the same materials at low shear rates with viscosity curves obtained using a capillary rheometer at high shear rates. He found in most cases that the viscosity was lower than the complex viscosity (Figures 5.5 and 5.6). This is opposite to what was observed in the present work, and the reason for this are not fully understood at present.

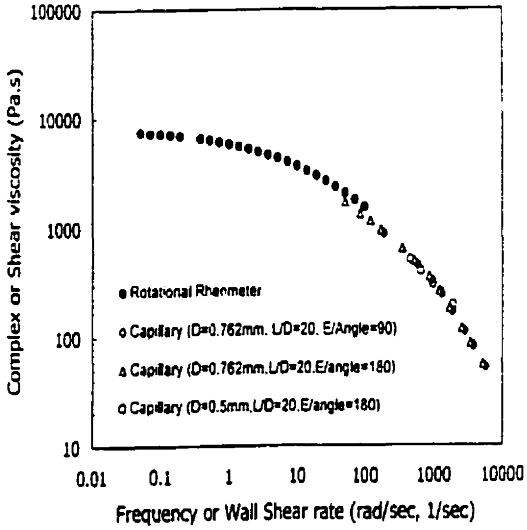

Figure 5.5. Test of Cox-Merz rule of LLDPE at 150℃ by Kim [1].

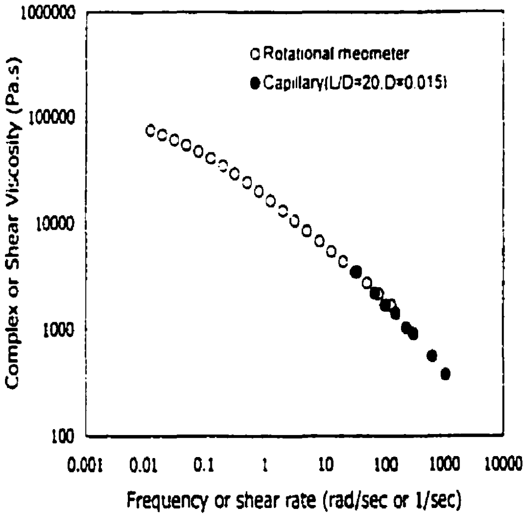

Figure 5.6. Test of Cox-Merz rule of BmPE at 150℃ by Kim [1].

5.1.3. The Effect of Pressure on Viscosity

To determine the effect of pressure on viscosity, steady shear experiments were carried out for each polymer at 170℃ at four pressures. Every experiment was carried out over a range of shear rates that started well above the lower limit of the SST but ended below the critical value for flow instabilities. Experiments were repeated four times at each pressure for each material. The maximum relative standard deviation was 5% for each pressure and material. The Cross model was used to fit the data (solid lines in the figures):

$$\eta = \frac{\eta_0}{1+|\lambda\dot{\gamma}|^m} \tag{1.3}$$

Figures 5.7 to 5.9 show viscosity curves for pressures ranging from 0.1 to 69 MPa. Figures 5.7 and 5.8 show that the viscosities of the LLDPE and LmPE have similar pressure dependencies, while in Fig. 5.9 the BmPE shows a stronger dependency. A quantitative analysis of the pressure dependence was performed by means of a pressure shift factor. To obtain pressure shift factors that could be used to construct master curves, two methods were used. One was based on the shift factor defined by Equation 1.37. The second method was to shift only along the horizontal, shear-rate axis a plot of stress versus shear rate. This is based on the following relationship, in which b_p is neglected as explained in Chapter 1.

$$\sigma(a_p\dot{\gamma}, P) = \sigma(\dot{\gamma}, P_0) \tag{5.1}$$

The curve fitting was carried out using the Cross model, Equation 1.49, where m was determined from the atmospheric pressure data and was assumed independent of pressure, while $a_p(P)$ was determined by shifting the viscosity curve for each pressure. Tables 5.1 to 5.3 show the resulting values of the parameters. Table 5.4 compares the zero-shear viscosities from the shear experiments with those from creep experiments.

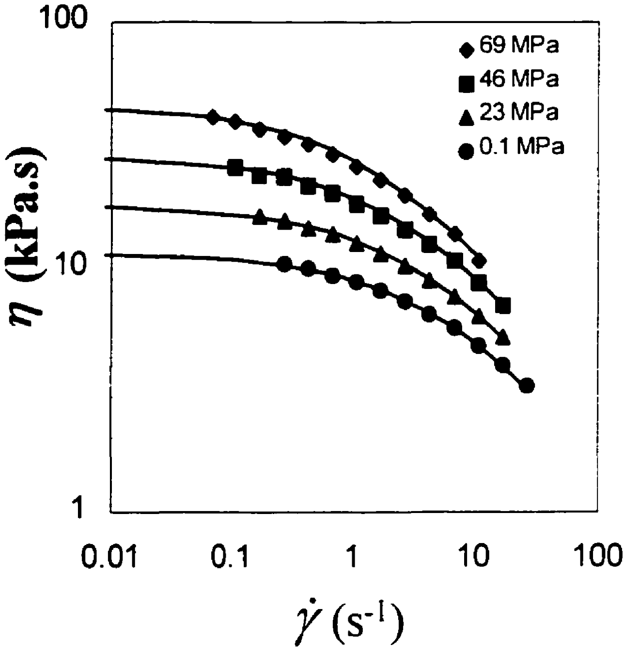

Figure 5.7. Flow curve of the LLDPE at 170℃ and at four pressures.

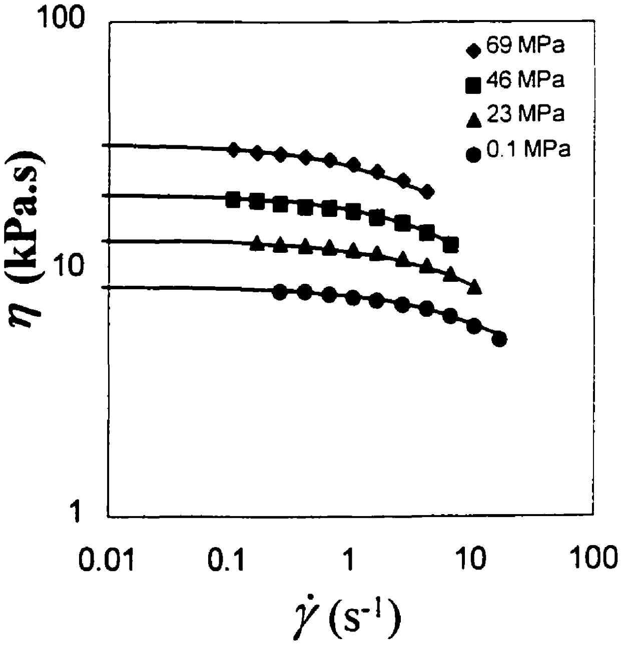

Figure 5.8. Flow curve of the LmPE at 170℃ and at four pressures.

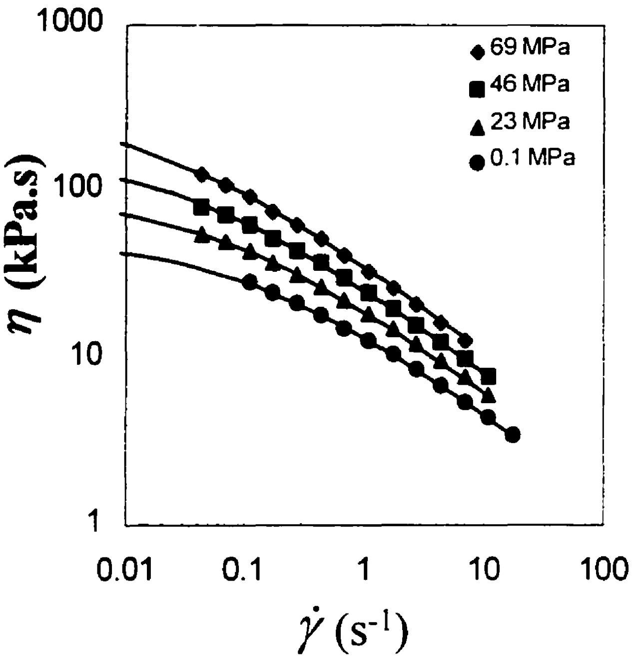

Figure 5.9. Flow curve of the BmPE at 170°C and at four pressures.

Table 5.1. Fitting parameters for LLDPE fitted with the Cross Model with m=0.66.

P (MPa)	η_0 (kPa)	λ (s)	a_P
0.1	11.44	0.15	1.00
23	18.19	0.22	1.58
46	23.30	0.30	2.47
69	42.88	0.56	3.74

Table 5.2. Fitting parameters for BmPE fitted with the Cross Model with m=0.54.

P (MPa)	η_0 (kPa)	λ (s)	a_P
0.1	53.20	7.85	1.00
23	101.88	15.04	1.92
46	172.81	25.51	3.25
69	310.17	45.79	5.83

Table 5.3. Fitting parameters for LmPE fitted with the Cross Model with m = 067.

P (MPa)	η_0 (kPa)	λ (s)	a_P
0.1	8.30	0.026	1.00
23	13.48	0.041	1.62
46	20.34	0.062	2.45
69	30.13	0.099	3.87

Table 5.4. Comparison of the zero-shear viscosity from steady shear and creep experiments.

Resin	η_0 (kPa.s) from shear experiments	η_0 (kPa.s) from creep experiments	Difference (%)
LLDPE	11.4	13.0	12.3
LmPE	8.3	8.1	2.4
BmPE	53.2	46.1	15.4

The second method involved plots of stress versus shear rate, where the shift was carried out only along the shear rate axis. Figures 5.10 to 5.15 show the stress versus shear rate plots and the pressure-shifted plots. The amount of shift was determined by visual inspection. The results of the two methods were essentially the same.

Figures 5.16 to 5.18 are master curves obtained using the pressure shift factors, and Fig. 5.19 shows the shifted results for all three materials on one plot. Figure 5.20 shows the pressure sensitivity of each PE. Long chain branched PE shows a larger pressure sensitivity than the linear PEs. Polydispersity has little effect. This trend is similar to that observed in the temperature sensitivity of viscosity. We note that $\ln(a_p)$ is linear with $(P-P_0)$. This is in agreement with the Barus equation:

$$\ln a_p(P) = \beta_0(P - P_0) \tag{5.2}$$

A pressure coefficient, β_0, can be defined as follows:

$$\beta_0 \equiv \frac{1}{\eta_0}\left(\frac{\partial \eta_0}{\partial P}\right)_T \tag{1.38}$$

This coefficient is the slope of the curve of $\ln(a_p)$ versus $(P-P_0)$.

Some reports of the pressure-dependence of viscosity make use of a shear-rate-dependent pressure coefficient. For example, Van Krevelen [2] and Goubert *et al.* [3] define this parameter as follows:

$$\beta(\dot{\gamma}) \equiv \frac{1}{\eta}\left(\frac{\partial \eta}{\partial P}\right)_{T,\dot{\gamma}} \tag{5.3}$$

This quantity can be obtained by a vertical shift of the viscosity versus shear-rate plot as shown in Fig. 5.21. Obviously this β is dependent on shear rate as shown in Fig. 5.22. Figure 5.23 shows graphically the relationship between $\beta(\dot{\gamma})$ and β_0. The solid line represents the viscosity curve whose slope is β_0. The shear-rate independent shift factor, β_0, is a material constant and should be used whenever possible to describe the pressure-dependency of rheological properties.

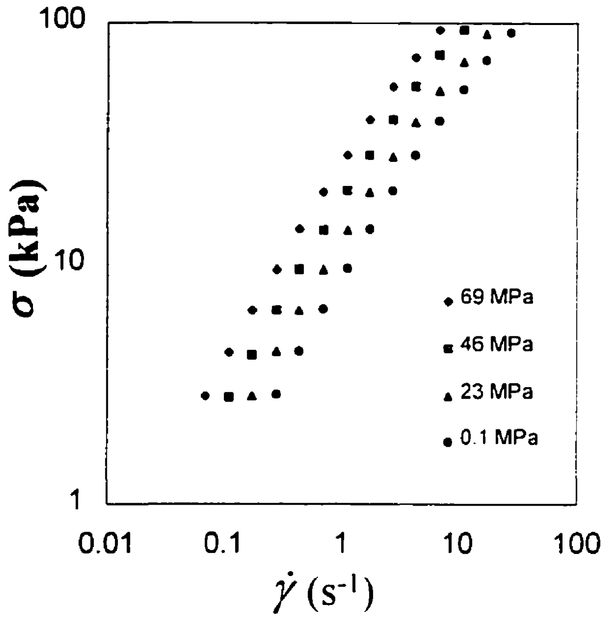

Figure 5.10. Stress with shear rate plot of the LLDPE at 170℃ and at four pressures.

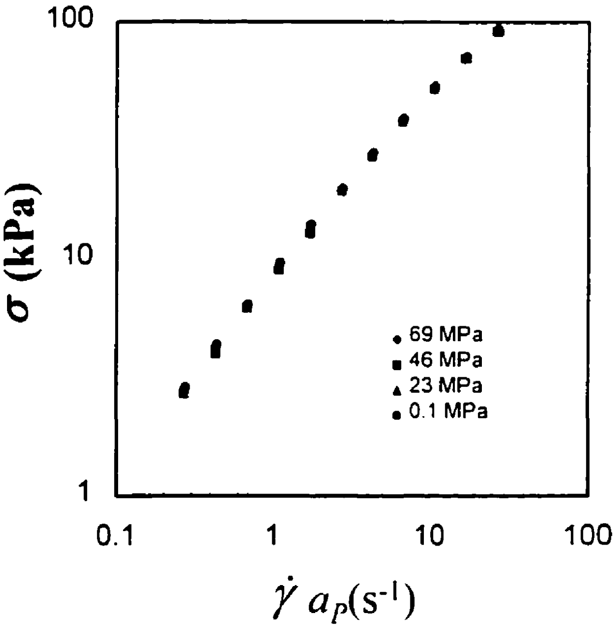

Figure 5.11. Stress with shifted shear rate plot of the LLDPE at 170℃ and at four pressures.

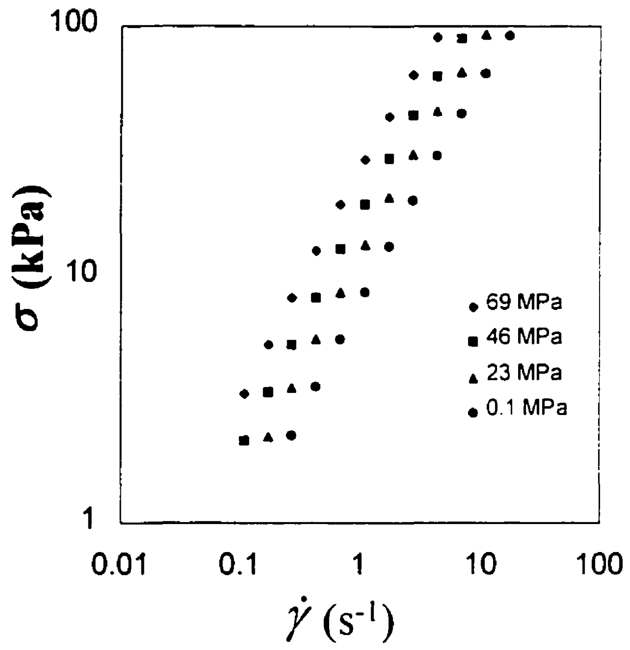

Figure 5.12. Stress with shear rate plot of the LmPE at 170℃ and at four pressures.

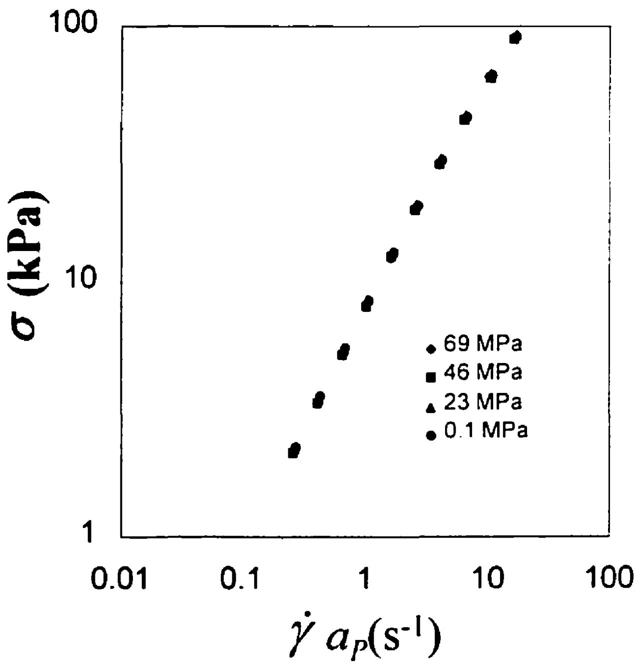

Figure 5.13. Stress with shifted shear rate plot of the LmPE at 170℃ and at four pressures.

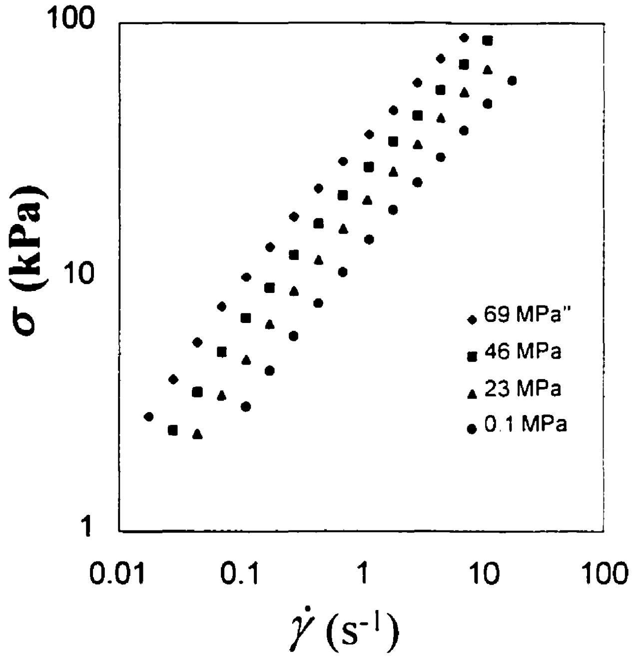

Figure 5.14. Stress with shear rate plot of the BmPE at 170℃ and at four pressures.

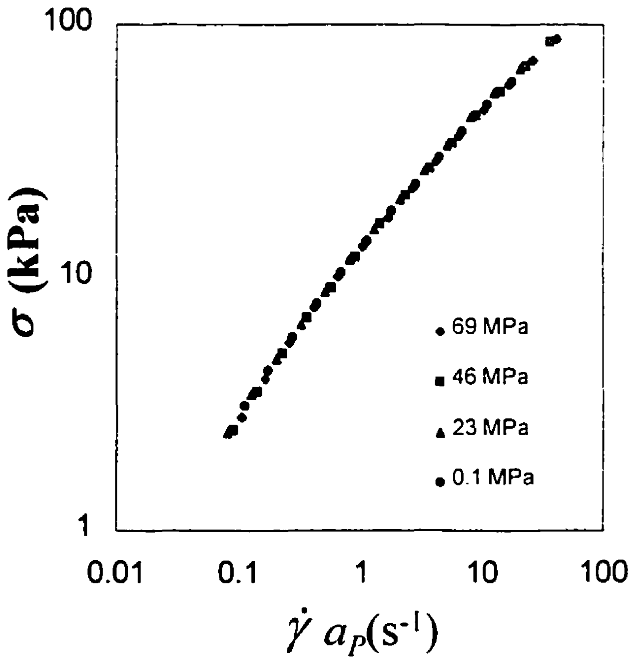

Figure 5.15. Stress with shifted shear rate plot of the BmPE at 170℃ and at four pressures.

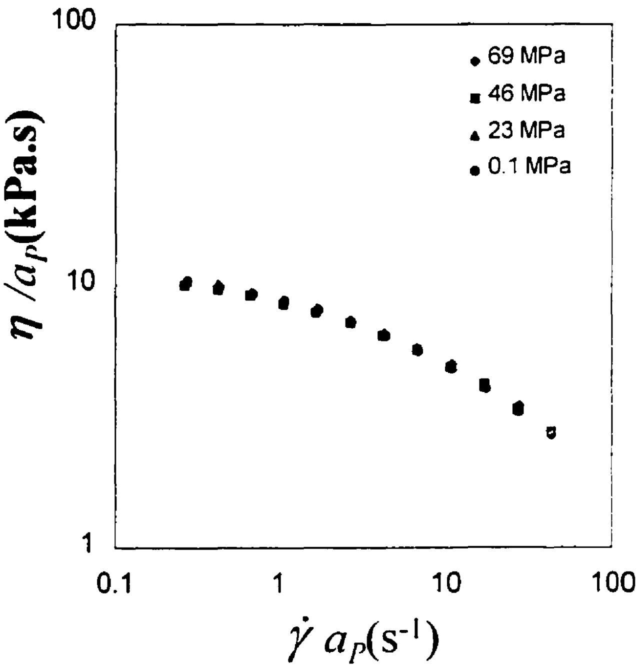

Figure 5.16. Master curve of the LLDPE.

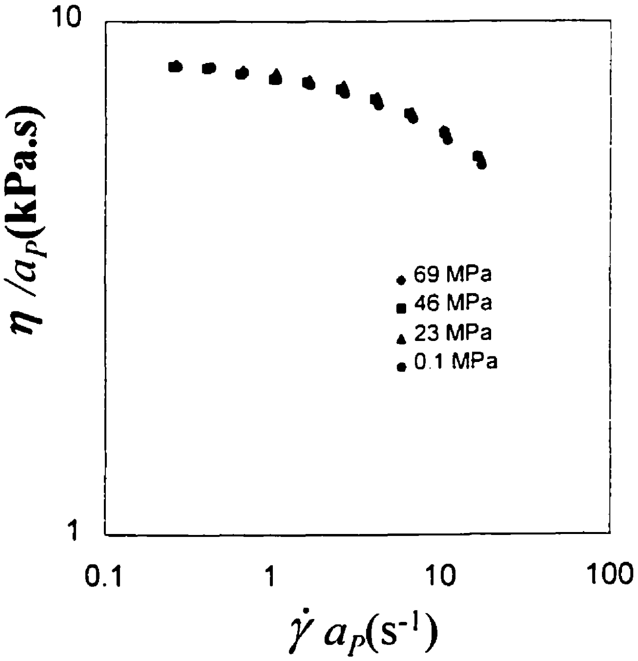

Figure 5.17. Master curve of the LmPE.

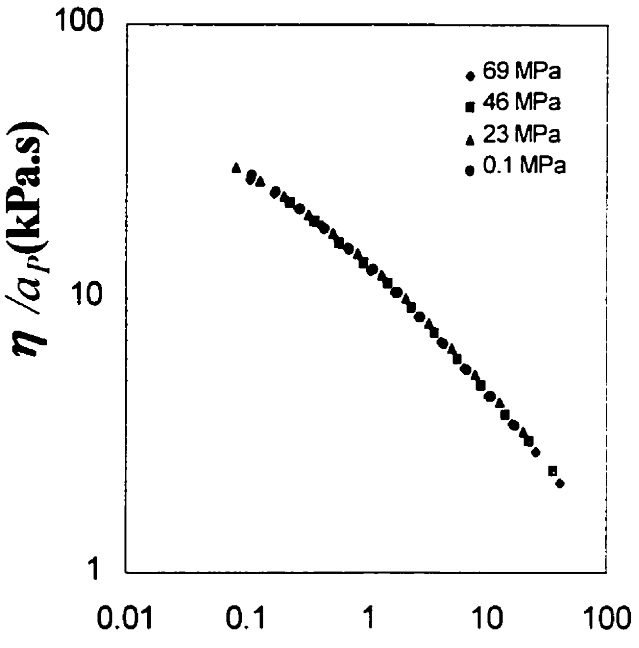

Figure 5.18. Master curve of the BmPE.

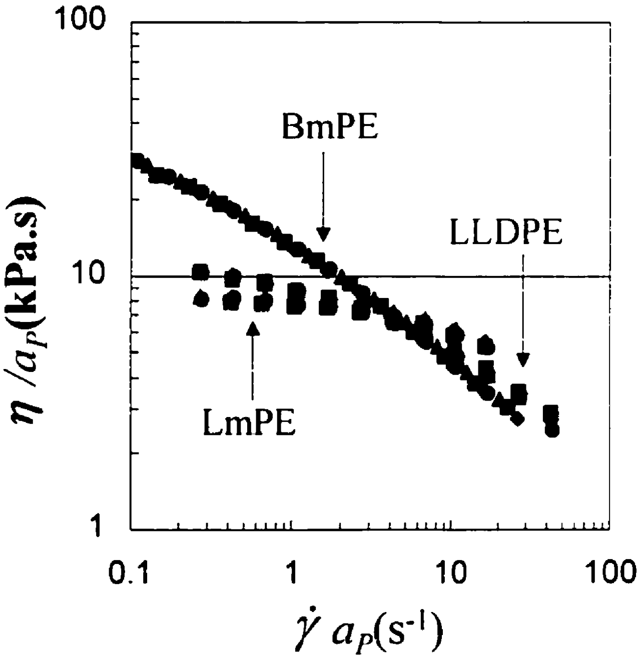

Figure 5.19. Master curves.

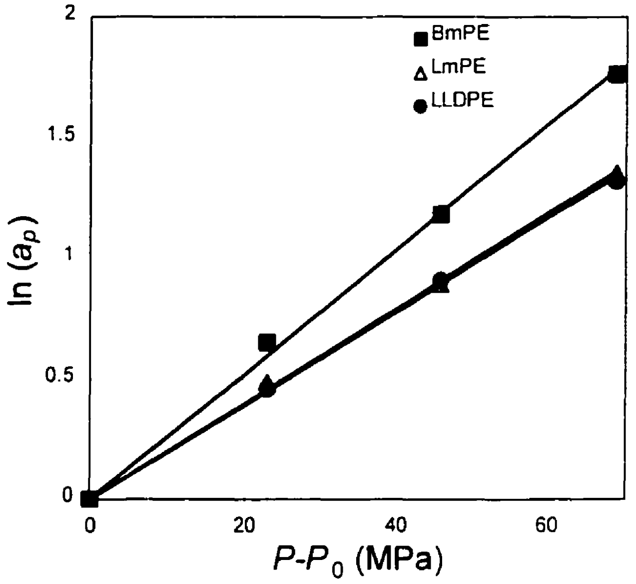

Figure 5.20. Pressure dependence of pressure shift factor.

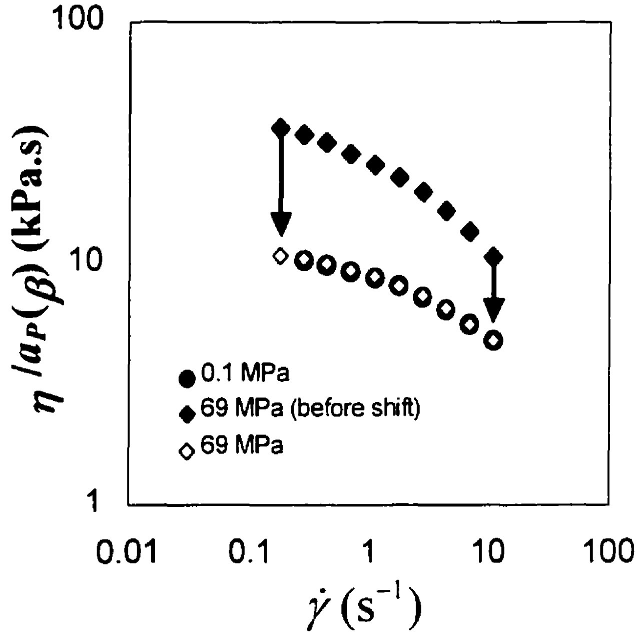

Figure 5.21. Viscosity versus shear rate for LLDPE at two pressures. Arrows show amount of shear-rate-dependent shift at the shame rates.

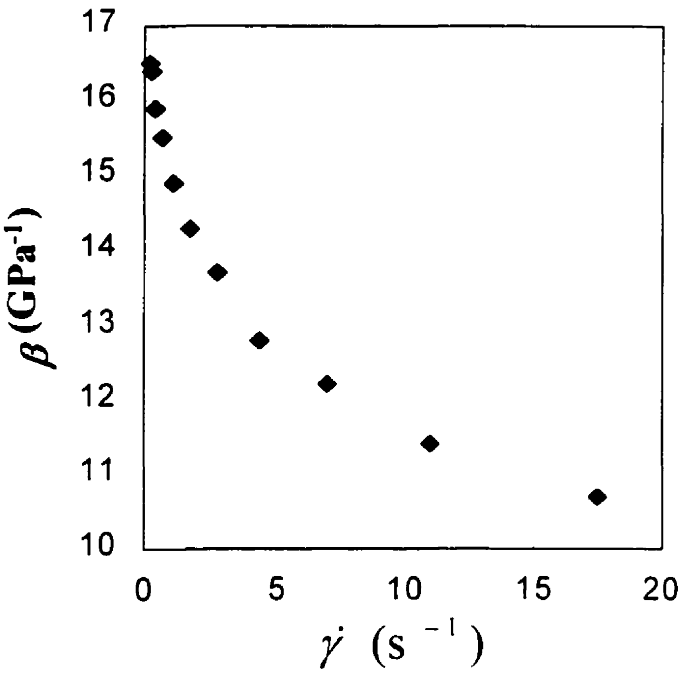

Figure 5.22. Shear rate dependence of β.

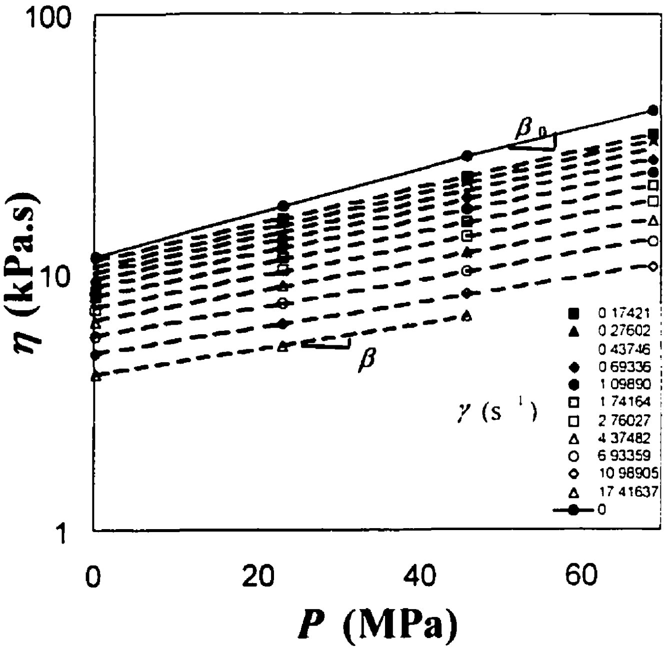

Figure 5.23. Graphical relationship between β and β_0.

5.1.4. The Effect of Pressure on the Stress Growth Function

Figures 5.24 to 5.26 show the effect of pressure on the stress transient at the start-up of steady shear. Figure 5.24 shows the results at a shear rate of 0.27 s^{-1} for BmPE. These curves exhibit an overshoot and a plateau. The viscosity can be obtained from the plateau (steady-state) value. The atmospheric pressure curve does not exhibit an overshoot, and pressure clearly amplifies the overshoot, which is a nonlinear effect. Figure 5.25 shows that at a shear rate of 1.74 s^{-1} the LmPE exhibits hardly any overshoot even at the higher shear rate. It can thus be inferred that LCB increases the maximum of the stress growth function and the time to steady state. Figure 5.26 shows stress growth functions for LLDPE at a shear rate of 1.74 s^{-1}, where the stress values are similar to those for LmPE. A longer time is required for steady state, and there is a larger overshoot than for LmPE, but there is little difference between the curves for LLDPE and LmPE. The normalized stress growth functions were obtained by dividing the stress growth function by the steady state stress, σ_{ss}, and it can be used for a direct comparison between the overshoots with P (Fig. 5.27).

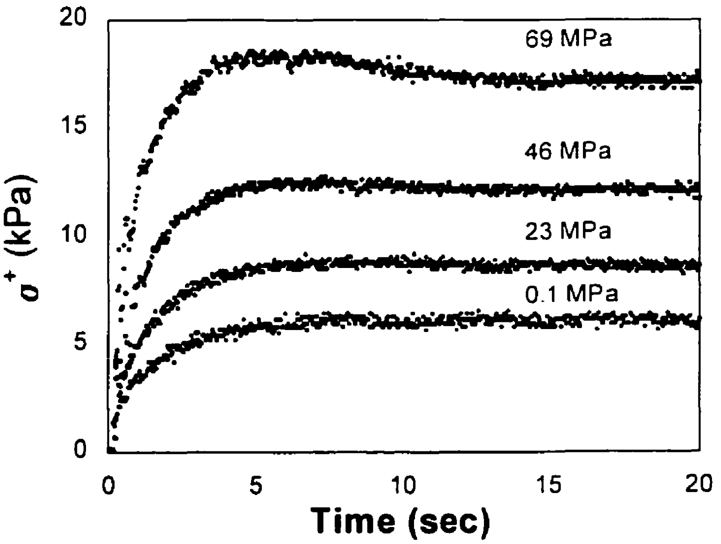

Figure 5.24. Pressure dependence of the stress growth function of BmPE with time at shear rate of 0.27 s^{-1}.

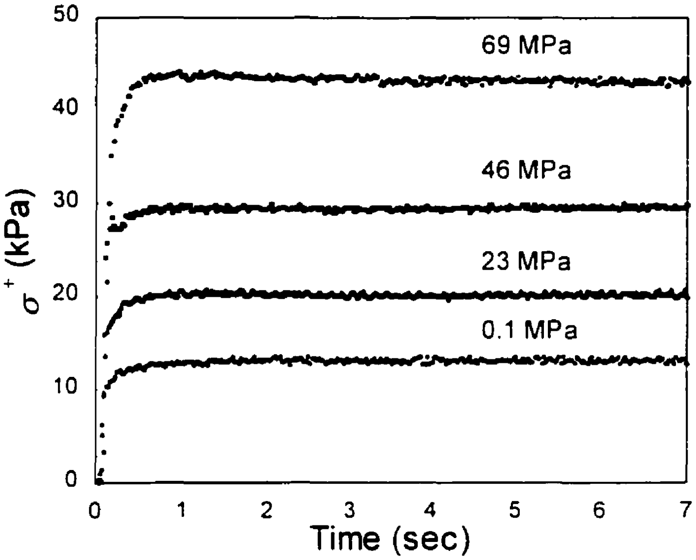

Figure 5.25. Pressure dependence of the stress growth function of LmPE with time at shear rate of 1.74 s^{-1}.

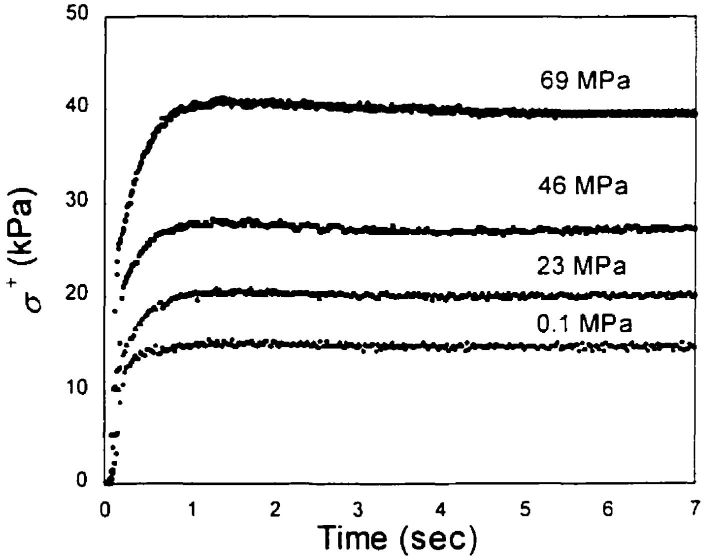

Figure 5.26. Pressure dependence of the stress growth function of LLDPE with time at shear rate of 1.74 s^{-1}.

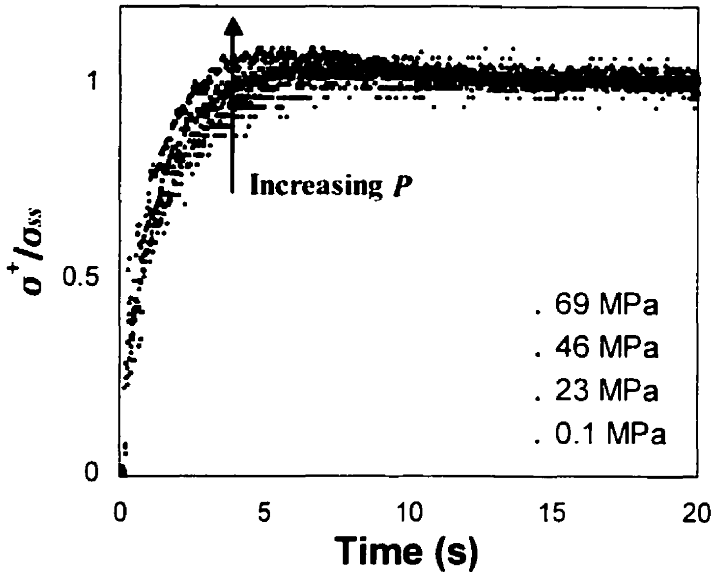

Figure 5.27. Pressure dependence of the normalized stress growth of BmPE at shear rate of 0.27 s^{-1}.

5.2. Controlled Stress Experiments

5.2.1. Comparison between Linear and Nonlinear Creep Compliance

To compare the linear and nonlinear creep, experiments first were carried out at atmospheric pressure. Nonlinear creep experiments were performed using the HPSPR at 1 atm, and linear creep experiments were peformed using an SR5000 controlled stress rheometer. This instrument was operated in the parallel plate configuration (25 mm diameter) with a gap of 1 mm. The stress was 10 Pa, and the experiments were performed for longer time than the nonlinear creep experiments since it requires more time to reach the steady state.

Figure 5.28 shows a difference between the linear and nonlinear creep compliances. The larger a stress is, the more sloped the curve is, but the curves in Fig. 5.28 exhibit this in the reverse order. However, after the curves of 5 kPa and

3 kPa exhibit a crossing point about 24 second. the order is changed. This results from the time required for reaching a steady state. The smaller a stress is, the slower the steady state is reached, and the linear creep curve at 10 Pa is not in the steady state yet in the range, and it is still curving while nonlinear curves are in the steady state. At longer time, there will be crossing points between the curves of 5 kPa and 10 Pa and then between curves at 3 kPa and 10 Pa. Eventually 5 kPa curve will be the most sloped, and 10 Pa will be the least sloped.

Figures 5.29 to 5.34 show the effect of LCB and polydispersity on the creep and recoil curves. The BmPE requires more time to reach steady state and exhibits

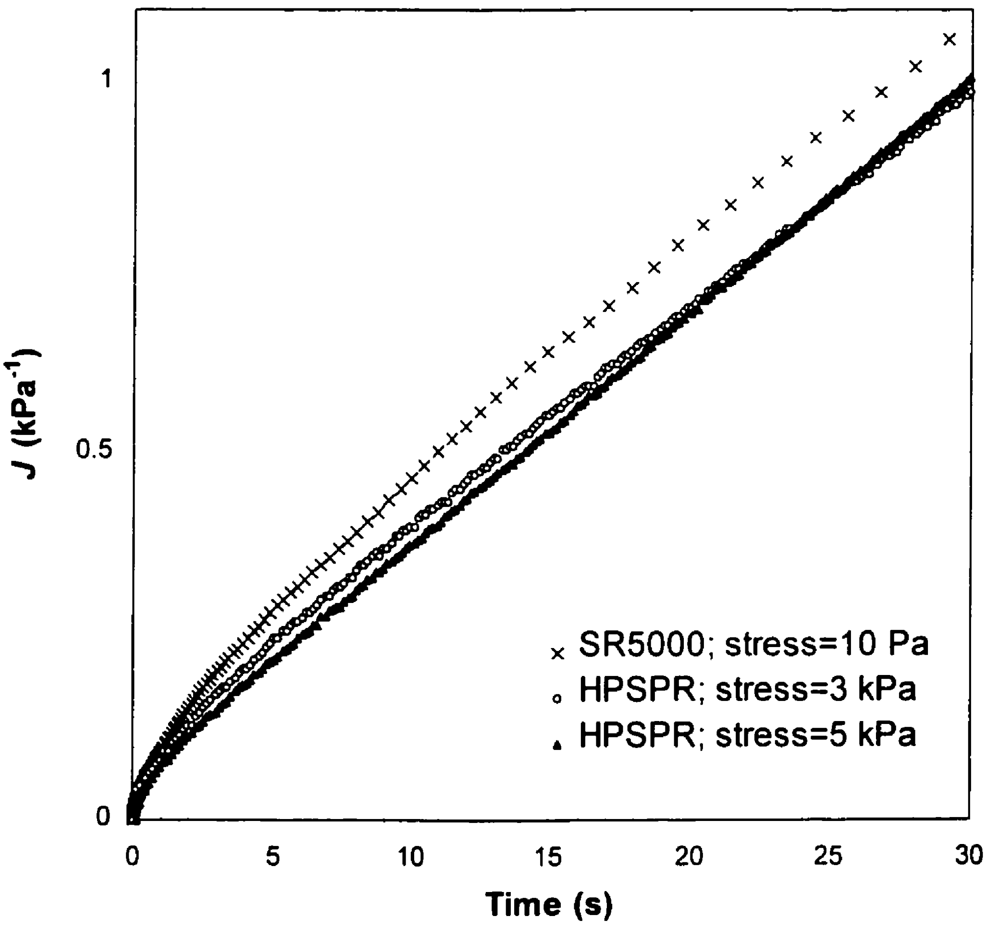

Figure 5.28. Comparison between linear and nonlinear creep compliances of BmPE at 0.1 MPa.

larger recoil than the LmPE at the stress of 3 kPa. Polydispersity has a similar effect. Both of linear and nonlinear creeps exhibit these effects. Figure 5.35 shows that 3 kPa is near the linear region of viscosity-stress plots for LmPE but not for BmPE. There is thus no significant difference between linear and nonlinear creep curve for LmPE in terms of slope (Fig. 5.30), while the creep curves for BmPE show a difference (Fig. 5.34).

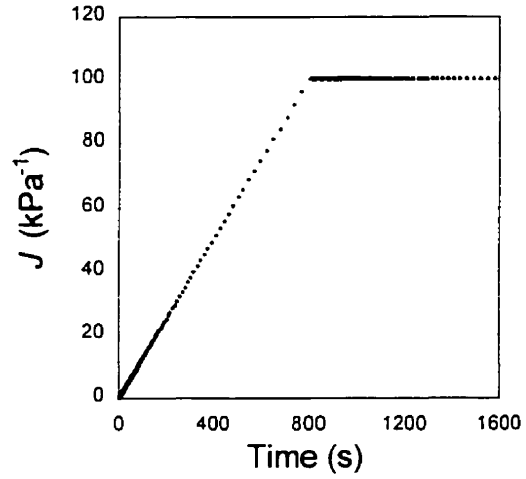

Figure 5.29. Linear creep and recovery of LmPE at 1 atm using SR5000.

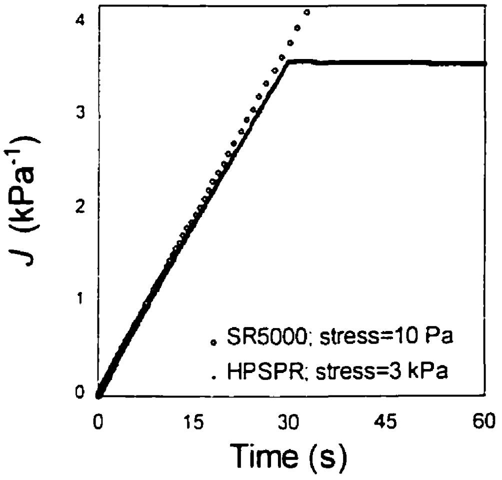

Figure 5.30. Comparison between linear and nonlinear creep of LmPE at 1 atm.

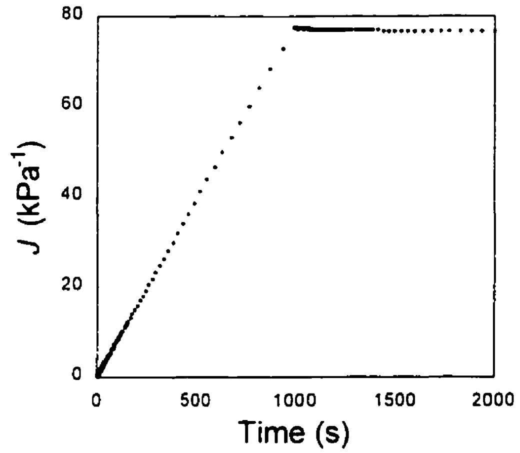

Figure 5.31. Linear creep and recovery of LLDPE at 1 atm using SR5000.

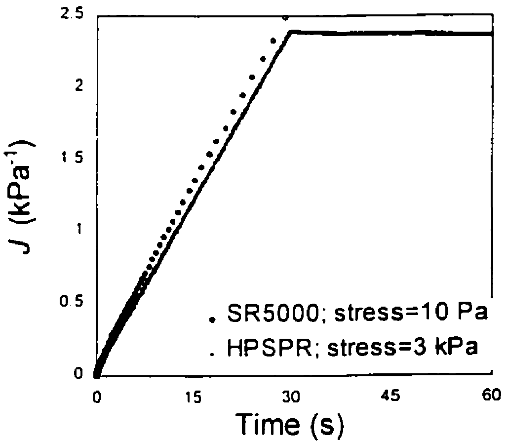

Figure 5.32. Comparison between linear and nonlinear creep of LLDPE at 1 atm.

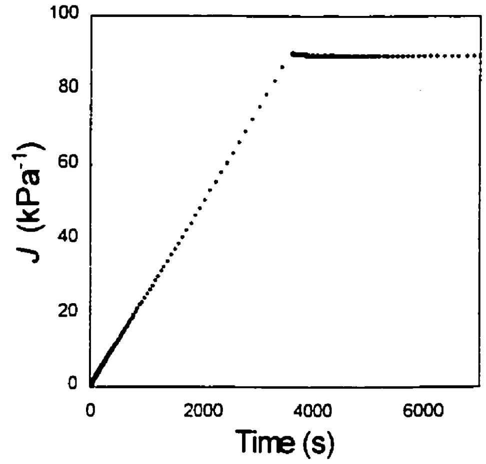

Figure 5.33. Linear creep and recovery of BmPE at 1 atm using SR5000.

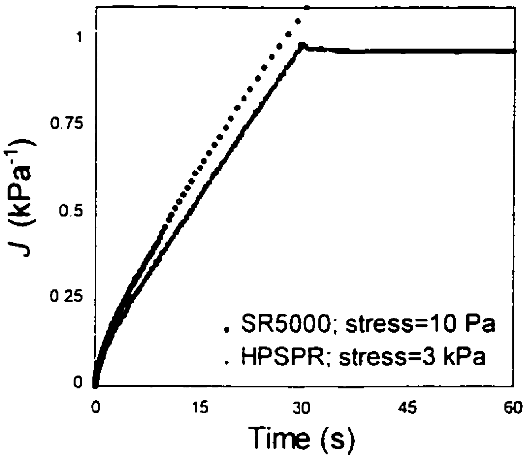

Figure 5.34. Comparison between linear and nonlinear creep of BmPE at 1 atm.

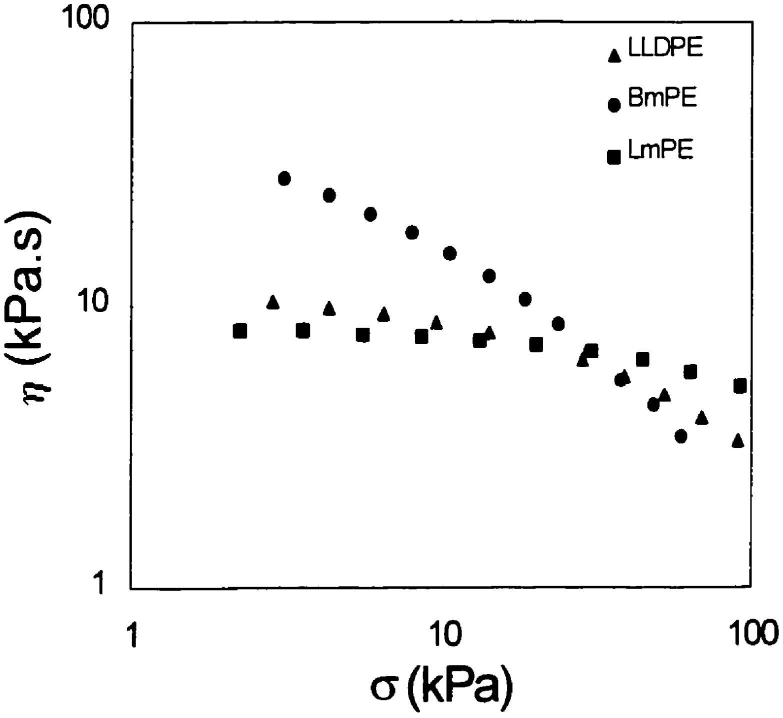

Figure 5.35. Viscosity versus stress plots by viscosity measurement experiments.

5.2.2. The Effect of Pressure on Creep Compliance

To determine the effect of pressure on the creep compliance, experiments were carried out at a constant stress of 3 kPa at four pressures and 170℃ for each PE. An instantaneous application of the stress is physically impossible, and the stress was increased at a rate of 90 kPa/s. Rates faster than this made the system highly unstable and impossible to control. At 30 s the stress was decreased to 0 kPa, and the creep recovery was recorded up to 60 s. The viscosity values were obtained from the reciprocal of the slope of the creep compliance between 25 and 30 s. Based on these viscosities, pressure shift factors were obtained and compared with those obtained in constant shear rate experiments.

Figures 5.36 to 5.38 show the effect of pressure on creep and recoil. Pressure decreases the value of the creep compliance and the slope of the creep curve, implying an increase in viscosity. The pressure shift factors were obtained from the viscosities, and Fig. 5.39 shows the shift factors as functions of pressure. This plot is similar to Fig. 5.20, which was obtained from the viscosity measurements. There is a 1 to 6% difference between the two shift factors at each pressure, which is not deemed significant.

Creep curves at high-pressure can be shifted on to the atmospheric curve by a factor of a_p. Figure 5.40 shows the shifted creep curves, and these reveal that pressure retards the time-response of a creep curve. It suggests that the zero-stress imposing time, $t_0(P)$, needs to be $t_0(P_0)a_p$ for a precise investigation of pressure effect on the recoil.

It is very difficult to tune the actuator controller for operation in the controlled stress mode due to the sensitivity and noise of the SST response, and another set of tuning parameters need to be entered at t_0 to obtain recoils. However, this tuning is essential for the determination of the early part of the creep curve and the steady state compliance. The somewhat erratic behavior seen in Figures 5.41 and 5.42 results from the non-ideal performance of the controller. Tuning the controller for BmPE was found to be more difficult than for the linear PEs. This is thought to be due to the enhanced elasticity of the branched material.

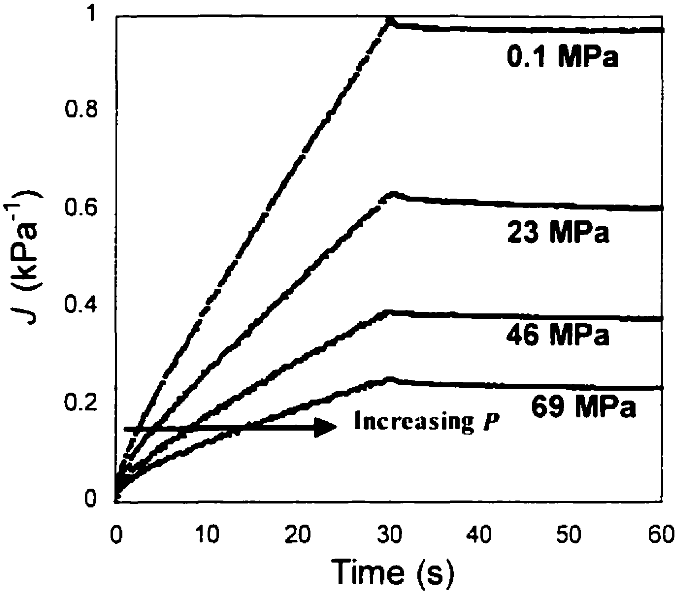

Figure 5.36. Pressure dependence of the creep of BmPE.

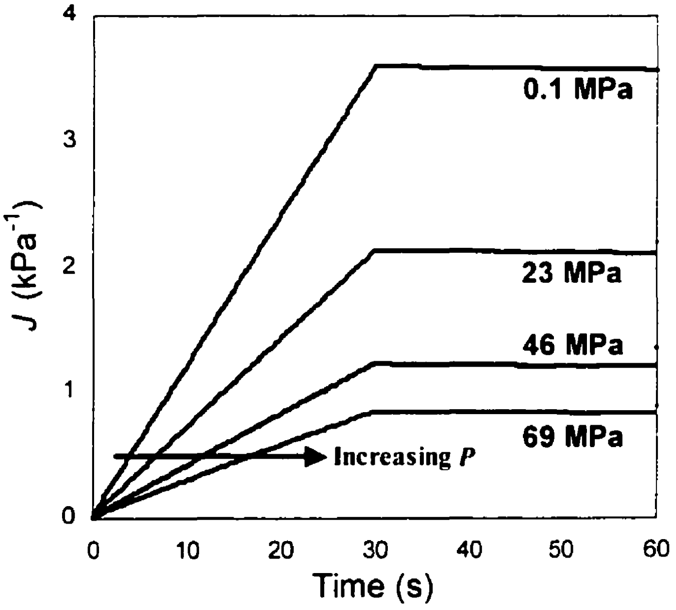

Figure 5.37. Pressure dependence of the creep of LmPE.

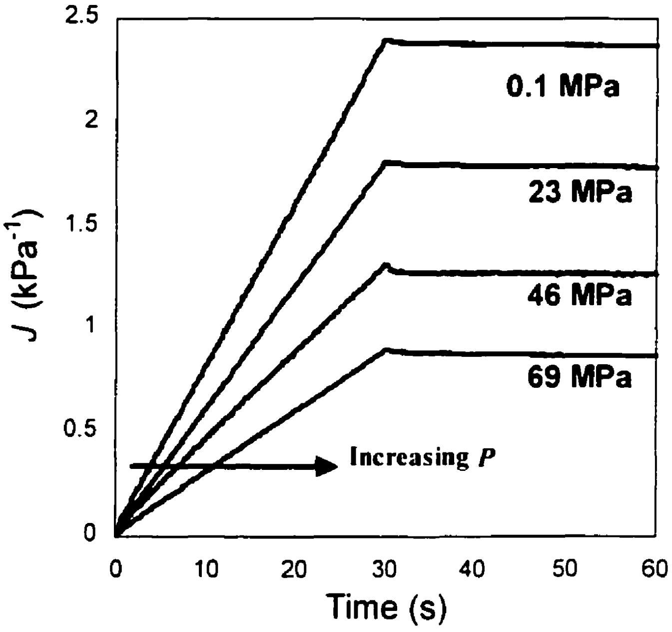

Figure 5.38. Pressure dependence of the creep of LLDPE.

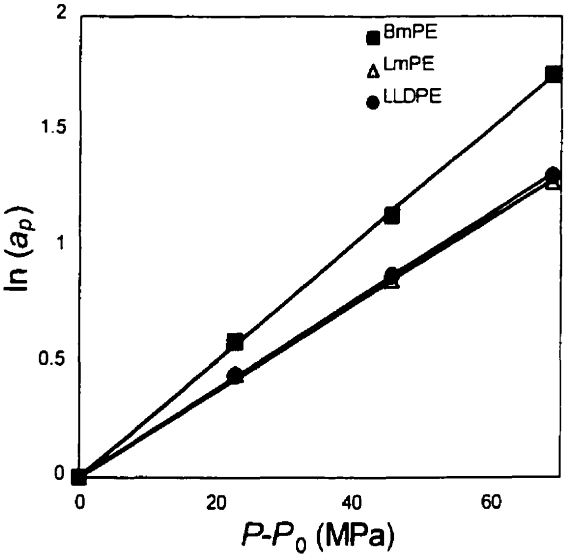

Figure 5.39. Pressure dependence of pressure shift factor from creep experiments.

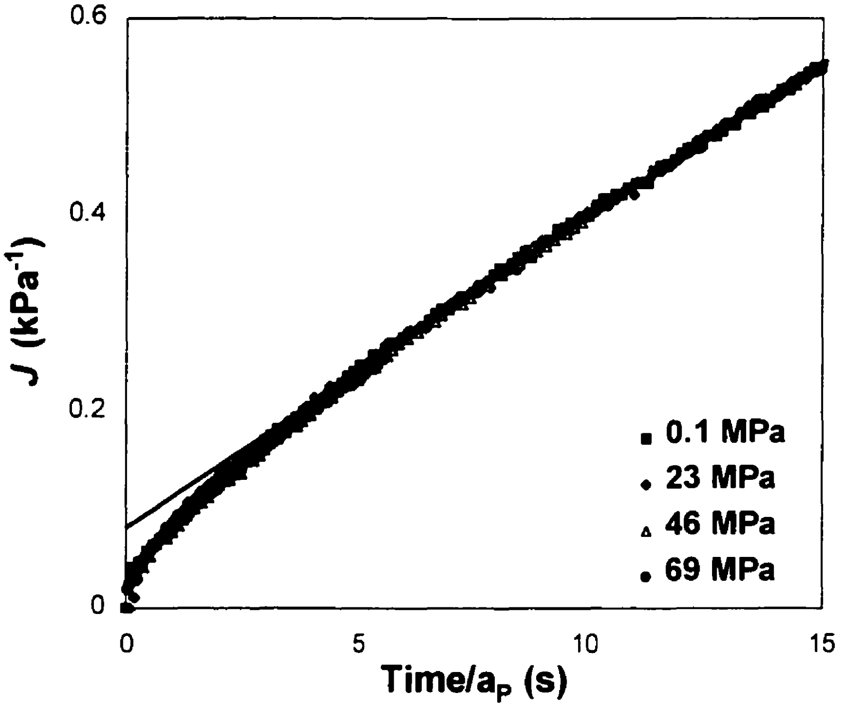

Figure 5.40. Master curve of creep compliance of BmPE.

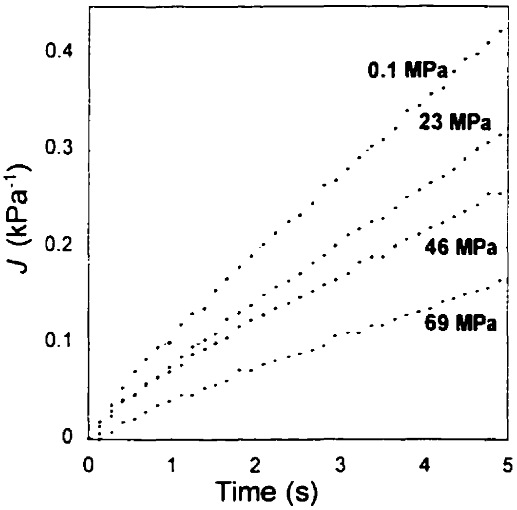

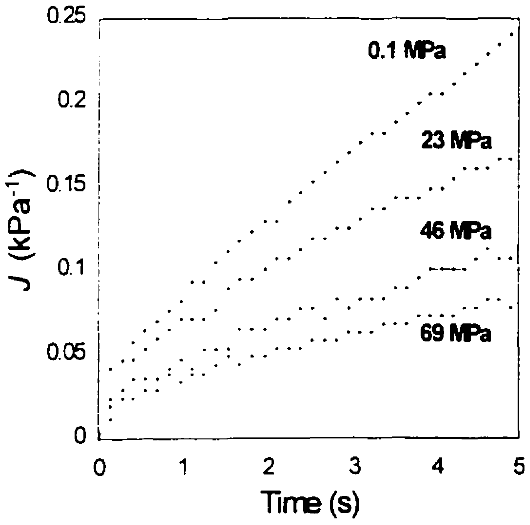

Figure 5.41. Early part of the creep curves of LLDPE.

Figure 5.42. Early part of the creep curves of BmPE.

References

1. S. Kim, Ph.D. Thesis, McGill University, Montreal, Canada, 2000.
2. Van Krevelen, *Properties of Polymers*, Third Edition, Elsvier, 1990.
3. A. Goubert, J. Vermant, P. Moldenaers, A. Göttfert and B. Ernst, in preparation (2001).

Chapter 6. Conclusions and Recommendations

6.1. Conclusions

1. The HPSPR can be used to determine the effect of pressure on the viscosity of molten plastics at pressures up to 70 MPa and temperatures up to at least 170 ℃.
2. The viscosities of the PEs studied increase exponentially with pressure.
3. Long chain branching increases the pressure sensitivity of viscosity in the polymers studied.
4. Polydispersity has no significant effect on the pressure sensitivity of viscosity
6. The HPSPR can be used to study the effect of pressure on creep and recoil at pressures up to 70 MPa and temperatures up to at least 170 ℃.
7. Increasing the pressure decreases the creep compliance.
8. LCB polymer shows a longer time for steady state and a larger recoil than linear polymer at a stress of 3 kPa.
9. Polydispersity has a similar effect to LCB for creep at a stress of 3 kPa.
10. Pressure shift factors from the creep experiments are similar to those obtained from constant shear-rate experiments.
11. Careful tuning of the controller in the stress control mode is required to study creep behavior.

6.2. Recommendations for Future Work

1. Develop a procedure for SST calibration at high pressure.
2. Develop an improved procedure for tuning the controller for controlled stress experiments.
3. Determine both the pressure and temperature dependency of the viscosity.
4. Carry out experiments using a series of long chain branched polymers to determine the effect of the level of LCB on the pressure sensitivity of viscosity.

Appendix. Experimental Procedures

1. Preliminary Checking

(1) The following items need to be inspected to verify that they are clean and oil-free:

- a) Fixed and moving plates
- b) SST active face head
- c) Mating surfaces
- d) Actuating rods
- e) Set screws

(2) The following items need to be checked to see that they are clean and well lubricated:

- a) O-ring groove on the cover plate of the pressure vessel:
- b) O-ring
- c) 7/8-inch bolts

(3) The following items need to be checked to see that they are connected correctly:

- a) Servo-valve and shear stress cables to the controller cards on the computer
- b) SST capacitance probe line to Capacitec^R amplifier
- c) Thermocouple to the temperature readout (Fig. A.1)
- d) Position of the rheometer selector of hydraulic pump oil (Fig. A.2)

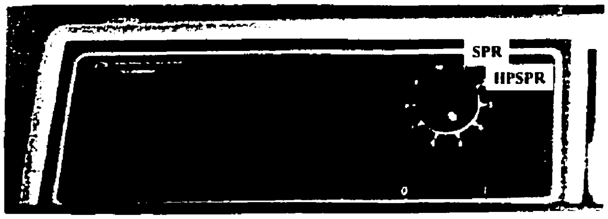

Figure A.1. Temperature readout.

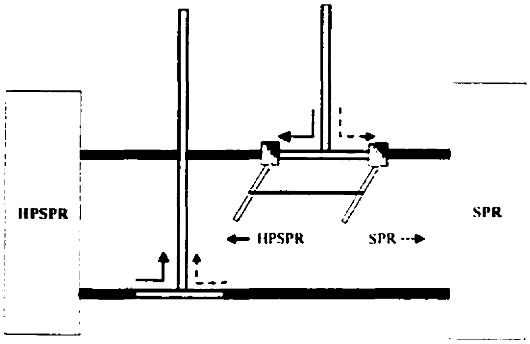

Figure A.2. Rheometer selector for hydraulic oil.

(4) Warming-up and tuning

a) Warm-up the actuator by sinusoidal linear movement.

b) Tune the control parameters (PIDO).

(5) Heating

a) Close the oven.

b) Turn on the heater (Figure A.3).

c) Set the temperature at the test temperature plus 20 ℃.

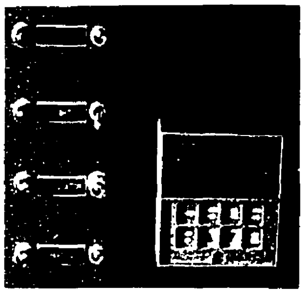

Figure A.3. Heating controller panel.

2. Adjusting the Control Parameters

The Proportional, Integral, Differential, and Offset (PIDO) parameters of the operating software, QUIKTEST, are adjusted to obtain a good match between command and feedback. A triangular mode of displacement can be used to adjust the controller parameters. The general procedure for adjusting the PIDO for controlled strain is as follows:

(1) After loading a dummy sample or without a sample, impose an appropriate frequency and amplitude for a triangular displacement.

(2) Set the I, D, and O parameters to zero.

(3) P governs the difference between the maximum and minimum values of the triangular displacement (Fig. A.5). Start the test. Adjust P until the desired response is achieved, and the difference between the maximum and minimum of the command and that of the feedback will the same.

(4) Adjust I to match the maximum and minimum of the command and those of the feedback (Fig. A.5).

(5) Adjust D to eliminate an overshoots when P is high. (usually zero).

(6) After stopping the test and turning off the I and D terms, adjust O to match the feedback and the command (Fig. A.6).

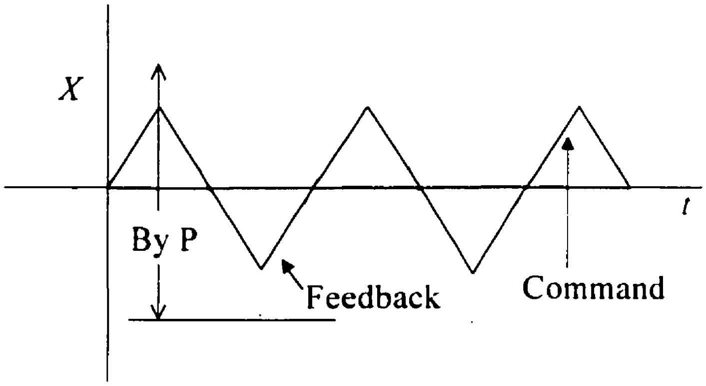

Figure A.4. Triangular displacement and effect of P parameter.

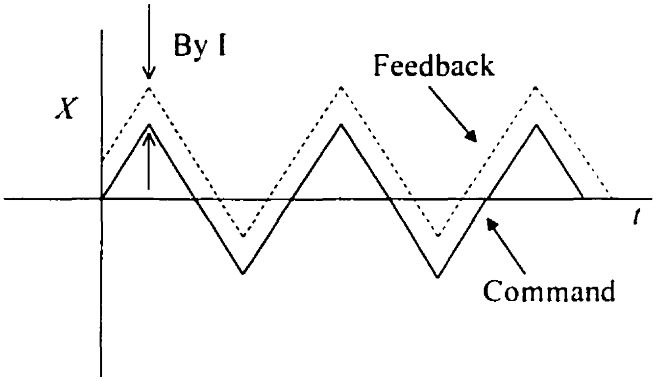

Figure A.5. Triangular displacement and effect of I parameter.

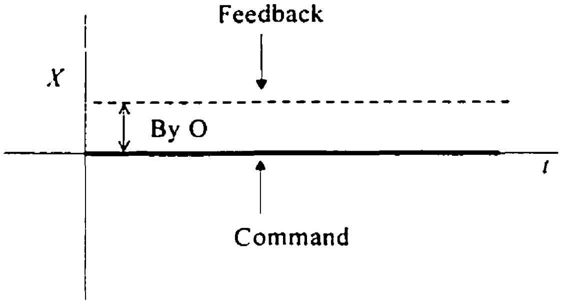

Figure A.6. Ambient command and effect of O parameter.

The procedure for adjusting the PIDO parameters for a controlled stress run is much more difficult and cannot be performed using a triangular displacement. The parameters can be adjusted using a ramp displacement, but this is a very laborious trial-and-error procedure, and control can easily be lost. If a large deformation occurs, for example 40 mm, the sample might fracture, and the controller will continue to try to achieve the set point stress.

3. Assembly and Sample Loading

a) Turn off the heater.

b) Install the moving plate.

c) Install the SST active face head.

d) Install the fixed plate.

e) Locate a sample of 1×8 cm at the center of the fixed plate.

f) Insert the O-ring in the groove.

4. Closing the HPSPR

a) Close the cover plate.

b) Insert the 7/8-inch bolts into the threaded holes.

c) Change the air inlet value to torque wrench mode.

d) Set the pressure value of the air regulator for the torque wrench.

d) Turn on air inlet.

f) Tighten the bolts with the torque wrench.

g) Close the oven.

h) Turn on the heater and set a test temperature.

5. Pressurizing

a) Change the air inlet value to oil-filling mode.

b) Turn on air inlet to fill HPSPR with Krytox oil.

c) Close every valve after the filling is finished.

d) Pressurize HPSPR with the hand pump until the desired pressure is reached.

6. Operating

Usually the set-point temperature can be reached one hour after loading the sample. Two hours after loading the sample, a run can be carried out.

6.1. Controlled Stress Mode

(1) Enter a value of the speed of stress change to reach a desired stress under

'rate' in the Quiktest operating software.

(2) Enter a value for the desired stress under 'level'.

(3) Press 'start'.

6.2. Controlled Strain Mode

Two ramp displacements, one upward and the other return, at constant speed are required to determine the viscosity.

(1) Enter a value of the desired speed of the moving plate under 'rate'.

(2) Enter a value of the desired total displacement under 'level'.

(3) Press 'start'.

7. Depressurizing

a)Turn off the heater

b) Open the release valve to 5° on the hand pump.

c) Close every valve connected to the hand pump.

d) Change air inlet value to oil-emptying mode.

e) Turn on air inlet to push oil out of the HPSPR.

8. Opening the HPSPR

a) Change air inlet value to torque wrench mode.

b) Open the oven.

c) Turn on air inlet.

d) Untighten the bolts with the torque wrench.

e) Remove 7/8-inch bolts.

f) Close the cover plate.

9. Disassembly and Sample Removal

a) Remove and clean the O-ring.

b) Remove the sample with an aluminium bar.

c) Remove the fixed plate

d) Remove the SST active face head

e) Remove the moving plate

10. Cleaning

a) Wipe out the inside of the HPSPR.

b) Cool down the plates and the SST active face head

c) Clean the plates and the SST active face head with Easy-off® oven cleaner.

d) Rinse off Easy-off® completely to prevent the corrosion of metal parts that are not made of stainless steel, such as the SST beam. Warm, around 60℃, xylene can be used to clean the plates and the SST head. It is a good solvent for polyethylene and does not corrode any metal. A ventilation system is required to use xylene since it is volatile and toxic.